Summer 2021

Development of Nanostructured Titania-Incorporated Photocatalysts for Environmental Applications

Sudheera B. Yaparatne
University of Maine, sudheera.yaparatne@maine.edu

DEVELOPMENT OF NANOSTRUCTURED TITANIA-INCORPORATED PHOTOCATALYSTS FOR ENVIRONMENTAL APPLICATIONS

By

Sudheera Bandara Yaparatne

B.Sc University of Kelaniya, Sri Lanka 2011

A DISSERTATION

Submitted in Partial Fulfillment of the

Requirements for the Degree of

Doctor of Philosophy

(in Chemistry)

The Graduate School

The University of Maine

August 2021

Advisory Committee:

Aria Amirbahman, Professor Emeritus, Civil and Environmental Engineering, Advisor

Carl P. Tripp, Professor of Chemistry

Scott Collins, Professor of Chemistry

Brian G. Frederick, Associate Professor of Chemistry

Douglas W. Bousfield, Professor of Chemical and Biological Engineering

DEVELOPMENT OF NANOSTRUCTURED TITANIA-INCORPORATED PHOTOCATALYSTS FOR ENVIRONMENTAL APPLICATIONS

By Sudheera Bandara Yaparatne

Dissertation Advisor: Dr. Aria Amirbahman

An Abstract of the Dissertation Presented
in Partial Fulfillment of the Requirements for the
Degree of Doctor of Philosophy
(in Chemistry)
August 2021

Ultraviolet (UV) radiation application in water and wastewater treatment has become a common approach for inactivation of protozoa and other pathogenic microorganisms. However, degradation of most organic compounds, such as taste and odor products prevalent in surface waters, has not been proven effective with direct UV photolysis. Advanced oxidation processes (AOPs) that involve efficient photocatalysts like TiO_2 show an advantage over direct UV photolysis providing fast reaction rates and non-selective oxidation of contaminants. However, the real-world application of TiO_2 in water and wastewater treatment is limited due to difficulties in separating the suspended nanosized particles following treatment, the relatively high charge carrier recombination effect, and the low absorption of visible light due to the wide bandgap of TiO_2. This study has developed two different TiO_2-based photocatalysts that address these limitations.

In the first study, an AEROXIDE® P25 TiO_2 powder-modified immobilized catalyst was developed using a glass substrate to degrade common algal taste and odor compounds 2-methylisoborneol (MIB) and geosmin (GSM) under UV-A (350 nm) irradiation. Attachment of the photocatalyst particles on the substrate was improved by

incorporating a TiO_2-SiO_2 sol-gel mixture as the binder and optimizing the Si concentration of the catalyst film to achieve superior robustness while maintaining a high photocatalytic activity. Catalyst films with a surface Ti:Si ratio ≈ 7 showed similar degradations rates but better robustness compared to immobilized P25 films. In the second study, a bismuth-titanate heterostructure composite containing a Bi_2O_3/$Bi_4Ti_3O_{12}$/TiO_2 mixture that showed visible light activity and a better charge carrier separation was developed. Heterostructure composition was optimized by incorporating the nonionic surfactant Tween-80 and varying the Bi concentration to achieve efficient photodegradation of phenol under visible light (420 nm) illumination. The catalyst with a Bi_2O_3:TiO_2:$Bi_4Ti_3O_{12}$ ratio = 1:7:15 showed the highest photocatalytic activity.

The UV active P25-modified TiO_2-SiO_2 film and visible light active bismuth-titanate heterostructure composite catalysts developed in this study showed promising efficacy with respect to photocatalytic degradation of organic pollutants. Future studies may consider a combination of the P25 modified TiO_2-SiO_2 catalyst film and bismuth-titanate heterostructure composite to extend the catalyst activity to a wide spectrum of electromagnetic energy. Further, pilot-scale application of these photocatalysts can assess their efficacy in drinking water treatment facilities.

DEDICATION

To my beloved parents, sister, and my dearest wife Thilini !

ACKNOWLEDGEMENTS

Foremost, I wish to thank my research advisor, Prof. Aria Amirbahman, for his patience, valuable guidance, endless support, and excellent mentoring throughout this study. I am indebted to Prof. Carl Tripp for the continuous support he kindly extended in all stages of my graduate degree at the University of Maine. The completion of this project would not have been possible without the support of Prof. Amirbahman and Prof. Tripp.

I am grateful to members of my advisory committee, Prof. Douglas W. Bousfield, Prof. Scott Collins, and Prof.Brian Frederick, for their constructive advice and feedback on my research. Special thanks to the Tripp and Amirbahman research groups for their support in my research projects. I would like to thank Dr. George Bernhadt, David Labrecque, Andrew Boucher for their instrumentation support. Also, many thanks to graduate students, faculty, technical and administrative staff of the Department of Chemistry and Department of Civil and Environmental Engineering at the University of Maine.

I am immensely grateful to my friends Phaneendra, Sirisha, Radowan, Sabrina, Shirly, Sampath, Shyamani, Panduka, Anushka, Pathum, Darshika, Seneviratne, Anusha, Srimal, Chandima, Asela, Madhira, Clarice, and Scott for their kind support.

Last but not least, I am grateful to my beloved parents, Thilak and Damayanthi, wife Thilini, and sister Ruvini. This work would not have been possible without the support, encouragement, and love of my family.

TABLE OF CONTENTS

DEDICATION iv

ACKNOWLEDGEMENTS v

TABLE OF CONTENTS vi

LIST OF TABLES x

LIST OF FIGURES xi

CHAPTER 1: INTRODUCTION 1

1.1. Safe drinking water 1

1.1.1. Emerging pollutants in drinking water 1

1.1.2. Advanced oxidation processes 5

1.1.3. Nanostructured materials for water treatment 7

1.2. Titanium dioxide (TiO_2) photocatalysis 8

1.2.1. TiO_2 as a Photocatalyst 9

1.2.2. P25 incorporation into TiO_2 sol-gel 15

1.2.3. Immobilization of photocatalysts 16

1.2.4. Titania-assisted photocatalytic degradation of taste and odor compounds 17

1.3. Visible light active photocatalysis 21

1.4. References 27

CHAPTER 2 : PHOTODEGRADATION OF TASTE AND ODOR COMPOUNDS IN WATER IN THE PRESENCE OF IMMOBILIZED TiO_2-SiO_2 PHOTOCATALYSTS.. 50

2.1. Abstract 50

2.2. Introduction 51

2.3. Experimental 54

2.3.1. Preparation of powder modified TiO_2-SiO_2 immobilized catalyst. 54

2.3.2. Photocatalytic degradation of MIB and GSM 56

2.3.3. Analytical determination of MIB and GSM 57

2.3.4. Reusability and radical hydroxyl production assessment and stability of the catalyst 58

2.3.5. Catalyst characterization 58

2.3.6. Photoleaching experiments 59

2.4. Results and discussion 60

2.4.1. Photocatalytic degradation of MIB and GSM 60

2.4.2. Reusability of the catalyst films 65

2.4.3. Hydroxyl radical generation and photodegradation mechanism 65

2.4.4. Robustness of catalyst films 69

2.4.5. Catalyst characterization 71

2.5. Conclusions 89

2.6. References 90

CHAPTER 3 : VISIBLE LIGHT-ACTIVATED CONTROLLABLE SYNTHESIS OF BISMUTH TITANATE PHOTOCATALYSTS FOR ORGANIC POLLUTANT DEGRADATION 100
3.1. Abstract 100
3.2. Introduction 101
3.3. Experimental 105
3.3.1. Preparation of Bi-incorporated titanate composites 105
3.3.2. Catalyst characterization 106
3.3.3. Photocatalytic degradation of phenol 107
3.4. Results and discussion 108
3.4.1. Photocatalyst characterization 108
3.4.1.1. Ti and Bi concentrations in catalysts 108
3.4.1.2. XRD analysis 109
3.4.1.3. X-ray photoelectron spectroscopy. 113
3.4.1.4. UV-Vis diffuse reflectance measurements 119
3.4.1.5. BET surface area. 122
3.4.1.6. Scanning electron microscopy 129
3.4.2. Effect of the surfactant on the catalyst formation 130
3.4.3. Photocatalytic degradation of phenol 131
3.4.4. Photocatalytic degradation mechanism 135
3.5. Conclusions 137
3.6. References 138

CHAPTER 4 : FUTURE DIRECTIONS 149

4.1. Preparation of visible light active TiO_2-SiO_2 coatings 149

4.2. Activity of bismuth incorporated photocatalyst composites 149

4.3. Implementation of catalyst films for photodegradation of pollutants in pilot scale 150

4.4. References 151

BIOGRAPHY OF THE AUTHOR 152

LIST OF TABLES

Table 1.1. MIB and GSM photodegradation under suspended TiO_2/ UV reactor systems 19

Table 1.2. MIB and GSM photodegradation under immobilized TiO_2/ UV reactor systems 20

Table 2.1. Photocatalyst films developed in this study 55

Table 2.2. Apparent rate constants (k_{app}) for photocatalytic degradation of MIB and GSM at 350 nm..... 64

Table 2.3. Photoleaching of Si and Ti from the photocatalyst..... 70

Table 3.1. Catalyst labeling scheme and corresponding Ti:Bi and Tween-80:Ti molar ratios 105

Table 3.2. Ti:Bi molar ratio of the catalysts after calcination obtained from ICP-AES….. 108

Table 3.3. Ti 2p3/2 binding energy values..... 118

Table 3.4. Structural characteristics of the catalysts 122

Table 3.5. Apparent rate constants for phenol photodegradation 132

LIST OF FIGURES

Figure 1.1. Taste and odor compounds (a) Geosmin (b) 2-methyl isoborneol 3

Figure 1.2. Environmental remediation approaches adapted from Guerra et al. 8

Figure 1.3. Octahedral unit cells of (A) rutile, (B) anatase, (C) brookite 9

Figure 1.4. Bandgap of some common photocatalysts with respect to NHE at pH 7; adapted from Prasad et al. (2019) 12

Figure 1.5. Potentials (vs. SHE) for various redox processes occur on TiO_2 surface at pH = 7; adapted from Fujishima et al. (2000) 13

Figure 1.6. Processes occur in TiO_2 photocatalysis 14

Figure 1.7. (A) Semiconductor bandgap narrowing due to non-metal doping (B) Co-doping non-metals in TiO_2 22

Figure 1.8. Photodegradation scheme for TiO_2/ Bi_2O_3 nanocomposite 24

Figure 2.1. Photocatalytic degradation experiment setup; Catalyst coated glass slides immersed in quartz beaker. 57

Figure 2.2. Time concentration plots for the photodegradation of MIB (500 ng L^{-1} initial concentration) for dark control, UV (350 nm) only, and ST photocatalyst……60

Figure 2.3. Time concentration plots for the photodegradation of MIB (500 ng L^{-1} initial concentration) for T, P, and PT photocatalysts 61

Figure 2.4. Time concentration plots for the photodegradation of MIB (500 ng L^{-1} initial concentration) for PS15T, PS20T, PS10T, PS5T, PS3T 62

Figure 2.5. Time concentration plots for the photodegradation of Geosmin (500 ng L^{-1} initial concentration for UV (350 nm) only, dark control, and PS3T catalyst 63

Figure 2.6. The concentration of hTPA at different repetitions 65

Figure 2.7. The plot of ln{[TPA]0/([TPA]0-[hTPA])} versus time used to determine the steady-state hydroxyl radical concentration in the dark, by UV only and in the presence of the PS3T catalyst and UV radiation. 66

Figure 2.8. Main products of GSM photodegradation in the presence of TiO_2 68

Figure 2.9. Main products of MIB photodegradation in the presence of TiO_2 68

Figure 2.10. The X-ray diffractogram of the photocatalyst films 71

Figure 2.11. The FT-IR spectra for the (A) PS20T; (B) PS15T; (C) PS10T; (D) PS5T; (E) PS3T; and (F) P-25 photocatalysts 73

Figure 2.12. The UV-Vis diffuse reflectance spectra of the photocatalysts 74

Figure 2.13. The XPS spectrum for the T photocatalyst 75

Figure 2.14. The XPS spectrum for the ST photocatalyst 75

Figure 2.15. The XPS spectrum for the PS3T photocatalyst 76

Figure 2.16. The XPS spectrum for the PS5T photocatalyst 76

Figure 2.17. The XPS spectrum for the PS10T photocatalyst 77

Figure 2.18. The XPS spectrum for the PS20T photocatalyst 77

Figure 2.19. The XPS spectrum for the PT photocatalyst 78

Figure 2.20. The XPS spectrum for the PS15T photocatalyst 78

Figure 2.21. The apparent rate constants (k_{app}) for the MIB (initial concentration 500 ng L^{-1}) photodegradation versus the surface atomic Ti:Si ratio 79

Figure 2.22. The apparent rate constants (k_{app}) for the MIB (initial concentration 500 ng L^{-1}) photodegradation versus the bulk Ti:Si mole ratio of catalyst films as determined by the ICP-AES 80

Figure 2.23. Photoluminescence spectra of the T, PT and PS20 photocatalyst films..... 81

Figure 2.24. The SEM micrograph of the photocatalyst films PS3T high magnification 82

Figure 2.25. The SEM micrograph of the photocatalyst films PS20T high magnification 82

Figure 2.26. The SEM micrograph of the photocatalyst films PS3T low magnification 83

Figure 2.27. The SEM micrograph of the photocatalyst films PS20T low magnification 83

Figure 2.28. SEM micrograph of the photocatalyst films T low magnification 84

Figure 2.29. SEM micrograph of the photocatalyst films T high magnification 84

Figure 2.30. SEM micrograph of the photocatalyst films ST low magnification..... 85

Figure 2.31. SEM micrograph of the photocatalyst films ST high magnification..... 85

Figure 2.32. SEM micrograph of the photocatalyst films PS5T low magnification..... 86

Figure 2.33. SEM micrograph of the photocatalyst films PS5T high magnification..... 86

Figure 2.34. SEM micrograph of the photocatalyst films PS10T low magnification..... 87

Figure 2.35. SEM micrograph of the photocatalyst films PS10T high magnification..... 87

Figure 2.36. SEM micrograph of the photocatalyst films PS15T low magnification..... 88

Figure 2.37. SEM micrograph of the photocatalyst films PS15T high magnification..... 88

Figure 3.1. Molecular structure of the Tween-80 103

Figure 3.2. X-Ray Diffractograms of the catalysts 110

Figure 3.3. Anatase (101) and $Bi_4Ti_3O_{12}$ (171) peak area obtained form XRD for (a) $B_{0.25}T$-2 and (b) $B_{0.5}T$-2 catalysts 111

Figure 3.4. Ternary phase diagram for the percentages of Bi_2O_3, TiO_2, and $Bi_4Ti_3O_{12}$ in the photocatalysts determined by XRD 112

Figure 3.5. XPS spectra of catalyst $B_{0.5}T$-0 113

Figure 3.6. XPS spectra of catalyst $B_{0.5}T$-0.5 114

Figure 3.7. XPS spectra of catalyst $B_{0.5}T$-1 114

Figure 3.8. XPS spectra of catalyst $B_{0.5}T$-2 115

Figure 3.9. XPS spectra of catalyst PBT-1 115

Figure 3.10. XPS spectra of catalyst PT-1 116

Figure 3.11. Gaussian peak fitting of XPS spectra of Ti 2p and Bi 4d3/2 region ($B_{0.5}T$-2 catalyst) 118

Figure 3.12. Modified Kubelka-Munk vs. energy plots; catalysts synthesized using Ti:Bi (molar) =1:0.5 and varying Tween-80:Ti (molar) (0, 0.5, 1 and 2) 120

Figure 3.13. Modified Kubelka-Munk vs. energy plots; catalysts synthesized varying Ti:Bi (molar) and using same amount of Tween 80 (Tween 80:Ti=2) 121

Figure 3.14. N_2 adsorption-desorption isotherms and corresponding pore size of $B_{0.5}T$-0 123

Figure 3.15. N_2 adsorption-desorption isotherms and corresponding pore size $B_{0.5}T$-0.5 123

Figure 3.16. N_2 adsorption-desorption isotherms and corresponding pore size $B_{0.5}T$-1 124

Figure 3.17. N_2 adsorption-desorption isotherms and corresponding pore size distribution of the catalysts $B_{0.5}T$-2 125

Figure 3.18. N_2 adsorption-desorption isotherms and corresponding pore size distribution of the catalysts $B_{0.25}T$-2 125

Figure 3.19. N_2 adsorption-desorption isotherms and corresponding pore size distribution of the catalysts B_1T-2 126

Figure 3.20. N_2 adsorption-desorption isotherms and corresponding pore size distribution of PT-1 127

Figure 3.21. N_2 adsorption-desorption isotherms and corresponding pore size distribution of T-2 127

Figure 3.22. N_2 adsorption-desorption isotherms and corresponding pore size distribution of the catalysts PBT-1 128

Figure 3.23. The SEM micrographs of the photocatalyst of the catalysts. (a: B0.5T-0,b: B0.5T-0.5, c: B0.5T-1, d: B0.5T-2, e: PBT-1, f: PT-1) 129

Figure 3.24. Time concentration plots for the photodegradation of phenol 1×10^{-4} M photocatalysts (0.04 g) synthesized using same amount bismuth (Ti:Bi =1:0.5) and changing amounts of Tween 80 133

Figure 3.25. Time concentration plots for the photodegradation of phenol 1×10^{-4} M photocatalysts(0.04 g) synthesized varying bismuth concentration (Ti:Bi =1:0, 1:0.25,1:0.5,1:1) and constant Tween-80 134

Figure 3.26. Schematic diagram for photocatalytic mechanism in TiO_2/ $Bi_4Ti_3O_{12}$/ Bi_2O_3 heterostructure 136

CHAPTER 1 : INTRODUCTION

1.1. Safe drinking water

Access to a safe, adequate, and clean water supply is an essential feature for sustainable development and wellbeing. Water safety and cleanliness are disrupted by climate change, population growth, excessive water pollution such as salt intrusion, soil erosion, poor hygiene, contamination of ground and surface water by algae blooms, detergents, industrial fertilizers, insecticides, chemicals, and heavy metals[1–4]. Purification of drinking water is one of the critical challenges the world is facing today. According to the world health organization (WHO) estimations, currently, 785 million people lack even a basic drinking water service, including 144 million people who are relying on surface water sources[5]. WHO predicts that half of the world's population will be living in water-stressed areas that have expanded due to climate change by 2025. When it comes to water safety in the United States, it has been estimated that 322-600 billion dollars in investments are needed over the next 20 years to overcome water purification issues[6]. Therefore, the development of efficient methods to decontaminate water has become a significant aspect of both humanitarian and economic concerns.

1.1.1. Emerging pollutants in drinking water

Drinking water treatment plants face significant challenges in remediating newly identified pollutants in aquatic media. Sixteen classes of substances (algal toxins, antifoaming and complexing agents, antioxidants, detergents, disinfection byproducts, plasticizers, flame retardants, fragrances, gasoline additives, nanoparticles, perfluoroalkylated substances, personal care products, pharmaceuticals, pesticides, and

anticorrosives) have been identified as emerging pollutants that pose adverse health and environmental implications[7].

Algal toxins are significant emerging pollutants in drinking water that are caused by cyanobacteria. These cyanotoxins result from diverse secondary metabolites produced by cyanobacteria, categorized as hepatotoxins, neurotoxins, cytotoxins, dermatotoxins, and irritant toxins[8]. Water treatment plants that use surface waters as their source are especially susceptible to the intake of cyanotoxins. Many lakes in temperate regions have experienced increased turbidity and algal blooms, including cyanobacteria[9]. This may be attributed to the changing climate, especially the increasing average temperatures, the increased eutrophication caused by agricultural, municipal, and industrial wastes' disposal into water bodies, and internal phosphorus release[10,11]. In addition, higher temperatures and extended periods of higher temperatures result in more widespread lake hypolimnetic anoxia[12], leading to internal sediment phosphorus release, causing undesired algal blooms[13].

Among the cyanotoxins, taste and odor compounds that are the secondary metabolites of cyanobacteria and actinomycetes have become a significant issue associated with drinking water quality and safety[14]. Although the health effects of taste and odor compounds are still not clear, the aesthetic issue of drinking water considered by consumers has become a challenge to managing drinking water treatment plants.

Common taste and odor compounds found naturally in the surface waters are geosmin (GSM), 2 methyl isoborneol (MIB), β-cyclocitral (CYC), and β-ionone (ION). These compounds have earthy, musty tobacco, and violet odors, respectively[15]. The main problem dealing with these taste and odor compounds is their extremely low odor threshold concentrations: GSM (4 ng/L), MIB (15 ng/L), CYC (19.3 ng/L), ION (7 ng/L)[15]. In this

thesis, GSM and MIB were used as taste and odor model compounds (Figure 1.1). MIB is a terpenoid produced by the cyanobacterial species, Oscillatoria and Phormidium, and actinomycetes[16–18]. GSM is bicyclic tertiary alcohol produced by certain species of Oscillatoria, Anabaena, Lyngbya, Symploca, and actinomycetes[17,18].

Only a few conventional water treatment methods have successfully removed taste and odor compounds at such low concentrations. Filtration, using granular activated carbon and sand, and alum coagulation are used for the removal of taste and odor compounds in some water treatment facilities[19,20].

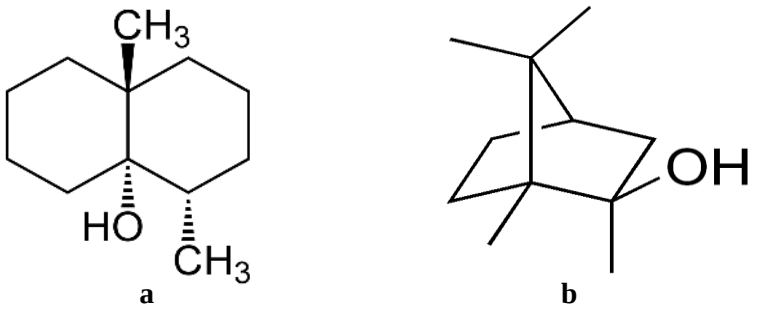

Figure 1.1. Taste and odor compounds (a) Geosmin (b) 2-methyl isoborneol

In the presence of dissolved organic matter (DOM), reduced adsorption of these compounds has been observed, and additional steps have to be taken to regenerate the saturated activated carbon for reuse[21,22]. Oxidants such as Cl_2, ClO_2, and $KMnO_4$ have proven ineffective in degrading these compounds due to tertiary alcohols' resistance toward mild oxidation[23]. Chlorination provides residual protection against the regrowth of pathogenic microorganisms[24,25] but can result in the formation of disinfection byproducts[26–29] and undesirable taste and odors[30] in potable water. Other conventional treatments such as biofiltration and thermal oxidation are also considered inefficient due to their high operating costs and generation of toxic secondary bi-products, respectively[31].

Ozonation and H_2O_2 associated processes are efficient in degrading taste and odor compounds MIB and GSM[32], but it has become less attractive due to its high equipment and operational cost and low solubility and stability in water[33]. Furthermore, ozone (O_3) reaction rates are slow and do not achieve complete mineralization of certain organic compounds such as aromatics, which have an inactivated π system or carboxylic acids[34,35]. Byproducts resulting from the ozonation are still being evaluated for their toxicity. Some potential carcinogens such as bromate (BrO_3^-) have been identified in ozone treatment of raw water for more extended periods (oxidation of bromide by O_3/UV)[36]. Other treatment techniques such as UV photolysis are not feasible alternatives for micropollutant removal[37]. UV photolysis alone does not provide sufficient energy to break down certain functional groups such as -NH_2 in organic compounds without help from an oxidant[38]. The use of Vacuum UV (VUV) irradiation (185 nm) appears to be promising in the degradation of MIB and GSM, but in the process, nitrate in water can be converted to nitrite[39] that is considered a potential carcinogen and can cause serious illnesses, especially in infants.

Among other persistent organic compounds, phenol is a widely used model compound to study the efficiency of degradation methods. Water can be contaminated by phenol mainly due to wastewaters from paint, pesticides, the petrochemical industry, pharmaceutical industry, and chemical industry[40]. Phenolic compounds are considered as a primary pollutant type due to their toxicity to organisms at low concentrations[41]. Phenol has been identified as a mutagenic and toxic substance that can cause mouth sores, nausea, urine darkening, and bloody diarrhea in humans[42]. Furthermore, due to the disinfection and oxidation processes, phenol can be converted to carcinogenic disinfection byproducts (DBP) such as cholorophenols[43]. Treatment methods such as adsorption and coagulation

for phenol removal are not considered as feasible because these methods cannot eliminate phenolic compounds from the system[44]. Moreover, sedimentation, filtration, membrane assisted phenol removal technologies are not favored due to high operational cost, generation of toxic DBP's, and not demonstrating sufficient efficiency[45,46].

1.1.2. Advanced oxidation processes

The processes involving the combination of UV photolysis and an oxidant are known as Advanced Oxidation Processes (AOPs); the added oxidizing agent such as H_2O_2 or a photocatalyst can be in the aqueous phase. AOPs provide a viable and effective approach to oxidation of a wide range of trace organic compounds in water[47–51]. AOPs are based on *in situ* generation of strong oxidants for degradation of persistent organic pollutants[52,53]. Ozonation and UV irradiation are well-established techniques that are implemented at full-scale in drinking water treatment facilities. AOPs enhance the efficacy of these techniques to degrade a wider spectrum of organic compounds at a faster rate by generating highly reactive and oxidizing species (Reactive oxygen species; ROS) such as hydroxyl radicals ($^{\bullet}OH$), superoxide radicals ($^{\bullet}O_2^-$), hydrogen peroxide (H_2O_2) and hydroperoxyl radicals ($HO_2\bullet$). AOPs be classified into two main categories of non-photochemical and photochemical.

Ozonation at elevated pH is one of the common oxidation techniques for drinking water, where the primary product is $^{\bullet}OH$. The AOPs involving O_3 include either homogenous or heterogeneous catalysts that catalyze the decomposition of O_3, generating $^{\bullet}O_2^-$, $^{\bullet}O_3^-$ and subsequently $^{\bullet}OH$. Another method is to use a combination of O_3 and H_2O_2 (peroxone) that results in generation of the conjugate base of H_2O_2 ($HO_2\bullet$) and its reaction with O_3 to generate $^{\bullet}OH$[54]. The application of O_3-related AOPs is limited due to the short

life of O_3 in water [55], its pH dependency, the high energy requirement for O_3 generation, the necessity of on-site O_3 production, and the risk for transportation and storage of H_2O_2[56].

Photochemical AOPs use radical promoters like O_3, H_2O_2, peroxydisulfate ($S_2O_8^{2}$), Cl_2, Fe (II), and semiconductor photocatalysts along with the UV light. Water treatment processes are typically based on UV sources, which are generally low (254 nm, monochromatic) or medium pressure (200-320 nm, polychromatic at various intensities) mercury vapor lamps[57,58]. Recently, UV light-emitting diode (LED) sources have also been investigated for water disinfection purposes[59]. UV energy plays a vital role in decomposing (via photolysis) organic compounds that are not transforming under non-photochemical oxidation reactions. When O_3 is used with UV (at 254 nm), O_3 is photolyzed to produce H_2O_2 and subsequently decomposes into $^{\bullet}OH$[60]. UV energy cleaves the peroxide linkage in H_2O_2 to form $^{\bullet}OH$, which forms H_2O and O_2[55]. The peroxone method under UV increases the decomposition rate of O_3, which in turn results in an increased $^{\bullet}OH$ generation rate[55]. UV-C (wavelength 200 - 280 nm) can cleave $S_2O_8^{2-}$ homolytically and produce primarily sulfate radicals ($SO_4^{\bullet-}$)[61]. Due to its lower quantum yield, selective reactivity, and high commercial pricing, $S_2O_8^{2-}$-based AOPs are not commonly used[57,62,63]. UV/Cl_2 is another promising AOP that produces $Cl^{\bullet}$ and $Cl^{\bullet}{}_2^{-}$ to oxidize target compounds[64]. Compared to $^{\bullet}OH$ radicals, $Cl^{\bullet}$ is proved to be a more selective oxidant because it reacts favorably with electron-rich compounds[65]. Fenton reaction with UV/visible radiation converts Fe(III) (one of the products) back to Fe(II) via photoreduction, where Fe(II) again can react with H_2O_2[66].

When comparing the AOPs, photo-driven AOPs have the advantage of providing simple, relatively inexpensive, clean, and efficient treatment alternatives to detoxify,

degrade, and mineralize contaminants in water[67]. Furthermore, among all of the oxidative treatments, photo-driven AOPs that use nanoparticulate photocatalysts, have been investigated extensively over the last decade due to their green and non-destructive character, sustainability and versatility when treating contaminated waters[57,68].

1.1.3. Nanostructured materials for water treatment

Capturing and degrading many organic pollutants have become challenging due to their potential high volatility, low reactivity, and complexity of the mixtures of different compounds[69]. Using nanostructured materials as photocatalysts has proven to be effective in meeting environmental standards and for adequate removal of a complex and broad spectrum of toxic chemicals and pathogenic microorganisms in raw water[70]. Photocatalytic water treatment is also categorized under the broad spectrum of AOPs, which generate ROSs, particularly $^{\bullet}OH$[71]. Recently, the incorporation of nanotechnology has emerged as an attractive approach to effectively remediate pollutants due to the unique properties of nanoparticles that are <100 nm in size. Compared to bulk materials, nanoscale materials exhibit exclusive properties, such as a high surface area to volume ratio, catalytic activity, high mechanical strength, thermal stability, electric conductivity, and strong magnetic properties[72]. Due to their large specific surface area, nanomaterials adsorb various types of pollutants, and in some cases, enable their effective catalytic degradation. In addition, they have low or no toxicity and low cost and show chemical stability, reusability, and tunable properties[73,74]. Nanomaterial-assisted environmental remediation approaches can be

categorized into five main categories, including absorption, adsorption, chemical reaction, photocatalysis, and filtration (Figure 1.2)[70].

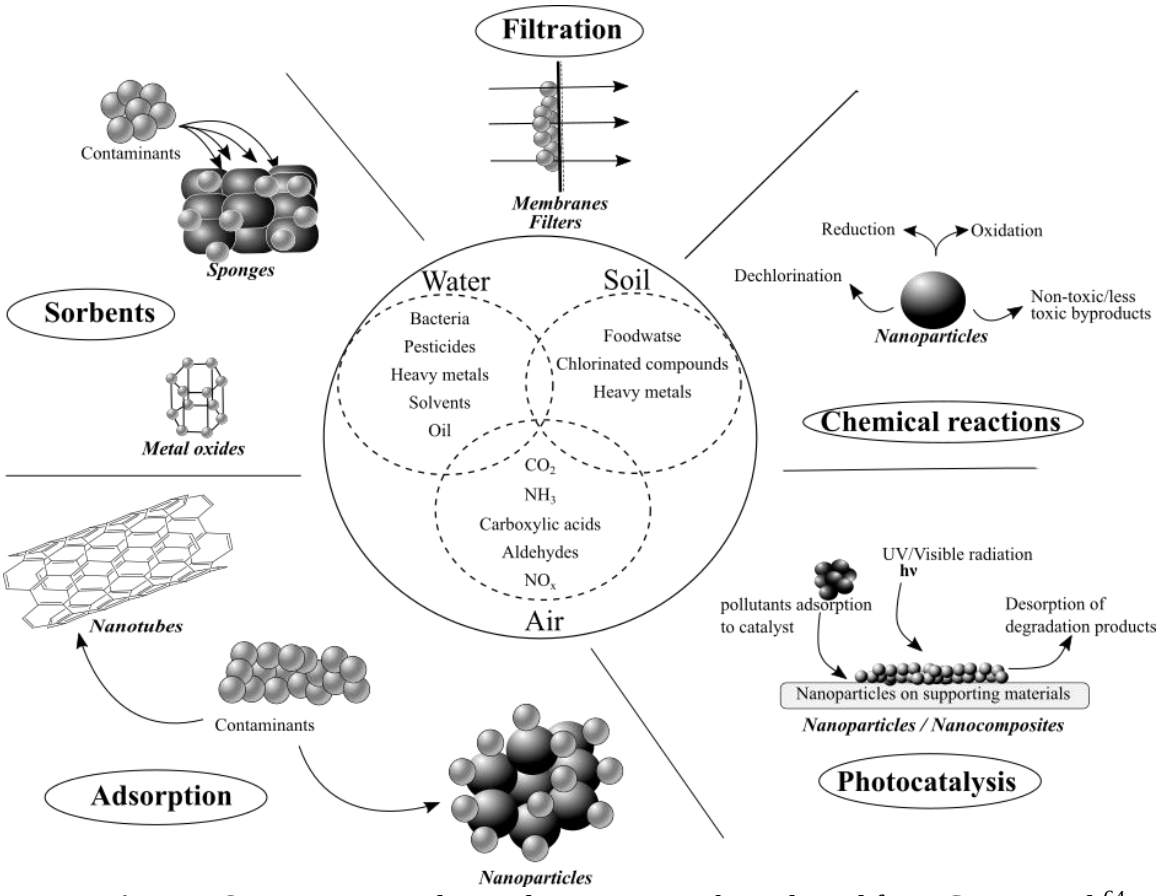

Figure 1.2. Environmental remediation approaches adapted from Guerra et al.[64]

1.2. Titanium dioxide (TiO_2) photocatalysis

Photocatalysis involves the activation of a catalytic material by radiation energy, which in turn increases the rate of a chemical reaction without itself being consumed.

The use of inexpensive, nontoxic, and reusable semiconductor photocatalysts has become an appealing approach due to features such as the ability to perform degradation under ambient conditions, requirement of only O_2 as the electron acceptor, energy higher than the band gap to initiate the reactions, and the possibility of supporting the catalysts on different types of substrates (e.g., glass, polymer, carbon nanotube, graphene oxide)[75]. The

effectiveness of semiconductors stems from their ability to generate charge carriers upon irradiation, followed by the production of ROSs (primarily •OH), which leads to further degradation reactions[76].

1.2.1. TiO_2 as a Photocatalyst

In 1972, Honda and Fujishima discovered the photosensitization effect of TiO_2 for the electrolysis of H_2O (water splitting) into H_2 and O_2. This occurred when they used Pt metal as the cathode under UV light irradiation of a TiO_2 photoanode[77]. TiO_2 remains as one of the most promising materials in environmental remediation applications due to its high oxidation efficiency, nontoxicity, high photostability, chemical inertness, self-cleaning features, and environmental friendly nature[78–80]. Also, TiO_2 cost is low owing to its natural abundance of Ti as 0.44% of the earth's crust[81]. Crystals of TiO_2 exist in one of three forms (i.e., polymorphs): rutile (tetragonal), anatase (tetragonal), and brookite (rhombohedral); Figure 1.3.

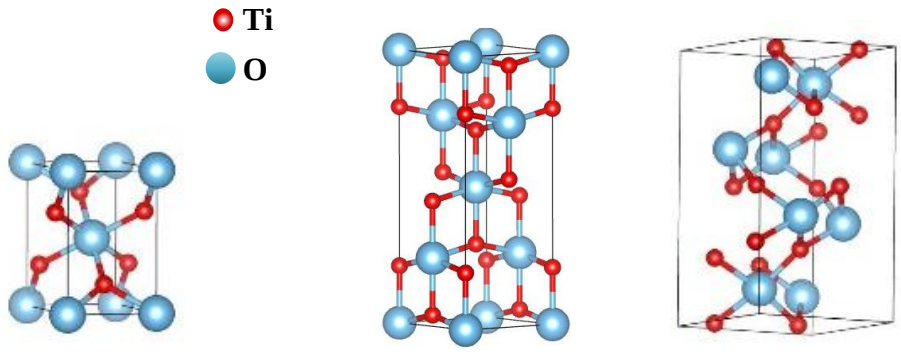

Figure 1.3. Octahedral unit cells of (A) rutile, (B) anatase, (C) brookite

Among these polymorphs, rutile is the stable phase, while anatase and brookite are metastable phases and readily transformed to rutile phase when heated[82]. Photocatalytic efficiency is mainly influenced by TiO_2 physicochemical properties, such as crystalline phases, exposed crystal facets, surface/bulk defects, specific surface area, and particle size[83]. Generally, anatase (in the presence of O_2 as the electron acceptor) shows a higher photocatalytic activity than rutile due to its higher Fermi level, a higher degree of hydroxylation, lower charge carrier recombination, and lower capacity to adsorb oxygen[84,85]. Also, anatase has a larger bandgap (3.20 eV) than rutile (3.00 eV), that raises the valence band (VB) maximum to higher energy levels relative to redox potentials of adsorbed molecules[86]. Lower photocatalytic activity of rutile is attributed to its larger grain size[87,88], lower specific surface area, and lower adsorption capacity[89,90]. The photogenerated holes and electrons for anatase have about one order of magnitude longer lifetime than for rutile, which enhances the surface photocatalytic reactions in the presence of anatase[91]. Photocatalytic activity studies of brookite (bandgap 3.30 eV) have been relatively fewer compared to those of anatase and rutile due to technical difficulties in synthesizing a pure brookite powder. However, several studies report that brookite nanocrystals show markedly high photocatalytic activity compared to rutile and anatase[82,92–94]. One of the main reasons for this observation may be the presence of trapped photogenerated electrons at a moderate depth between the conduction band (CB) and VB of the brookite (mid gap state), which increases the lifetime of both electrons and holes[95]. In contrast, the trap depth of anatase is too shallow to extend the lifetime of electrons and holes, and that of rutile is too deep for the electrons to contribute to the photocatalytic reactions. It has been observed that TiO_2 synthesized by mixing anatase with either rutile

or brookite or mix all three phases at an optimal level slows the recombination of photogenerated electrons and provides a higher photocatalytic activity than the pure phase species[82,94,96,97].

Anatase, rutile, and brookite are considered as wide bandgap semiconductors[98]. The VB of TiO_2 primarily consists of O *2p* states and a few Ti^{4+} *3d* states creating a strong p-d hybridization between Ti *3d* and O *2p* states, which form bonding states in the VB region[85]. Conduction bands are composed of Ti *3d* states hybridized with a few O *2p* and Ti *3p* states. Due to the presence of oxygen vacancies, which are compensated by the presence of Ti^{3+} centers, TiO_2 is considered an n-type semiconductor. The oxygen vacancies can be formed from the surface and bulk by heating to temperatures of 500-700 °C[84]. Oxygen defect sites change the electronic structure of TiO_2 by introducing an interband electronic donor state, which has Ti *3d* character 0.8-1.0 eV below the CB[99,100].

An efficient semiconductor photocatalyst is capable of adsorbing two reactants simultaneously that can be reduced and oxidized by photonic activation through absorbing radiation energy (hv) higher than the bandgap energy (E_g). Bandgap energies of several semiconductors and redox potentials relative to the normal hydrogen electrode (NHE) at pH seven are shown in Figure 1.4[101].

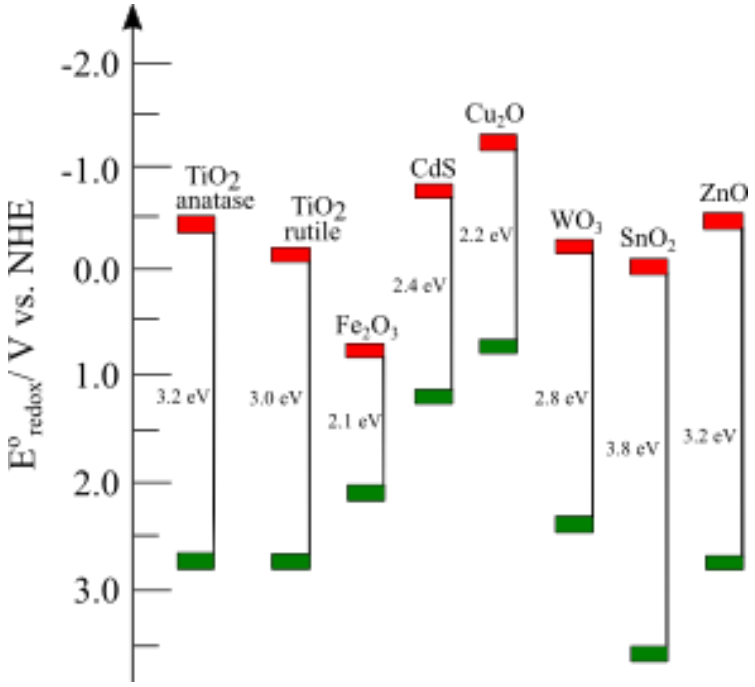

Figure 1.4. Bandgap of some common photocatalysts with respect to NHE at pH 7; adapted from Prasad et al. (2019)[101]

Among semiconductors, TiO_2 shows an additional advantage of efficient reduction of O_2 and oxidation of water simultaneously due to the redox potentials of its CB and VB. This is important because the photocatalytic decontamination of water relies mainly on the effective production of holes, $^{\bullet}OH$, and $^{\bullet}O_2^-$. More specifically, the redox potential for the photogenerated holes is more positive than the redox potential needed for producing $^{\bullet}OH$ from water at pH = 7, and the potential for CB electrons is negative enough to reduce O_2 to $^{\bullet}O_2^-$ as shown in Figure 1.5.

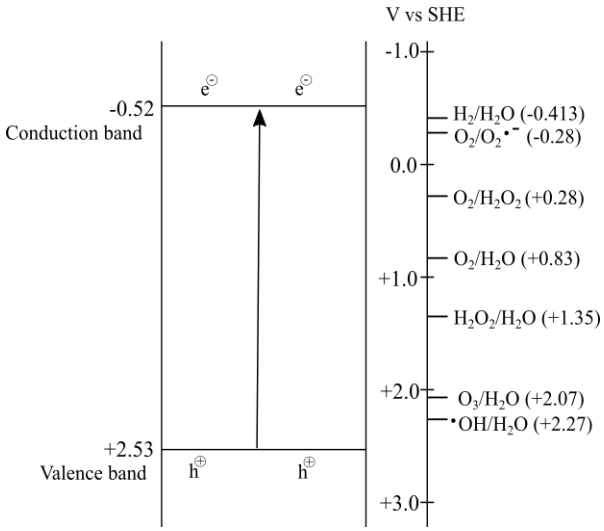

Figure 1.5. Potentials (vs. SHE) for various redox processes occur on TiO_2 surface at pH = 7; adapted from Fujishima et al. (2000)[102]

The formation of photogenerated holes and electrons (charge carriers), which occurs upon irradiation with UV light corresponding to the energy equal or greater than to the bandgap in TiO_2 is shown in Figure 1.6. When TiO_2 absorbs photons, electrons filled in the VB are excited to the vacant CB, creating holes in the VB. After this electron-hole pair separation, holes and electrons migrate to the surface to react with donor (D) and acceptor (A) molecules to drive the oxidation and reduction reactions, respectively (steps 1 and 3 in Figure 1.6). During the electron-hole migration process, electrons and holes recombine on the surface or in bulk, and the energy of the charge carriers is converted to the vibrational energy of lattice atoms (phonons) or photons (steps 2 and 4 in Figure 1.6) [103]. Generally, recombination occurs at the defect sites that lead to lower TiO_2 photocatalytic efficiency. Reactions on the photocatalytic surfaces can be classified into two types according to absorbed photon energy usage: downhill and uphill reactions[103]. Downhill reactions use photon energy to induce thermodynamically favored reactions, such as the decomposition of organic compounds. In uphill reactions, photon energy is converted to chemical energy by splitting H_2O into H_2 and O_2. Photocatalytic reactions

solely occur at the catalyst surface, where photogenerated holes and electrons (charge) migrate to the surface and induce the reactions. Prior to the photocatalytic reactions, charges undergo four major processes: separation, thermalization, trapping, recombination, and transport.

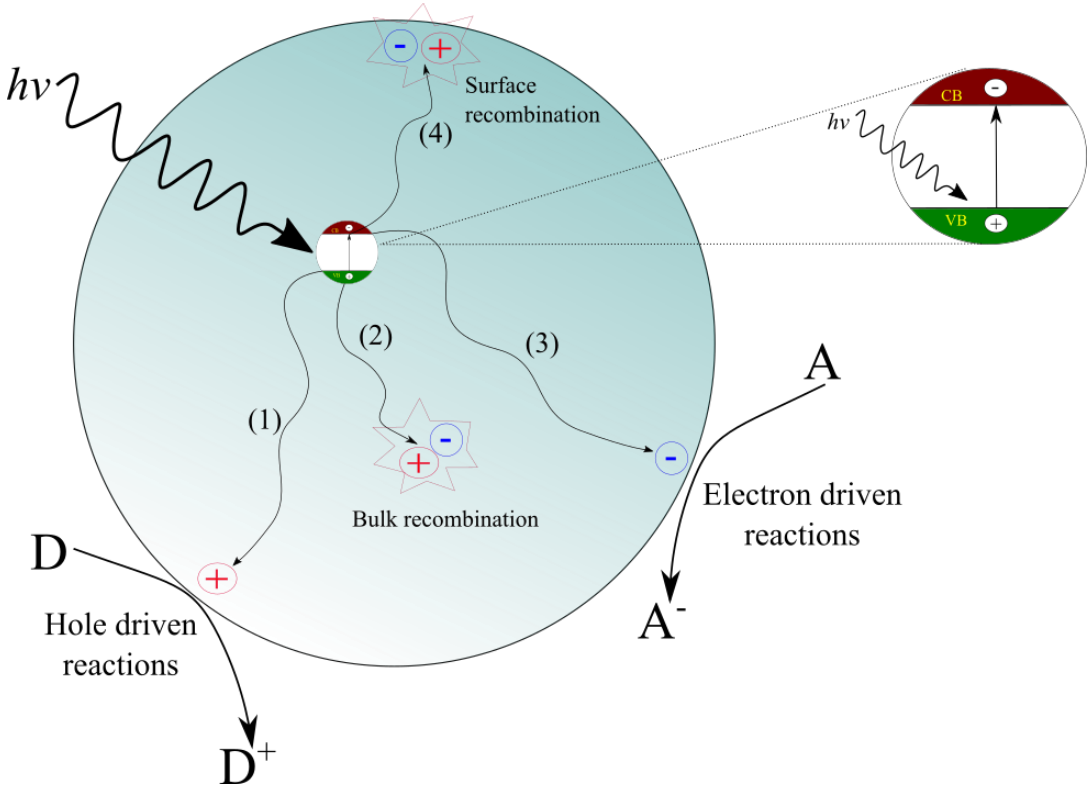

Figure 1.6. Processes occur in TiO_2 photocatalysis

Charge separation occurs after the generation of electron-hole pairs, and only less than 10% of separated charge carriers can be used in photocatalysis due to rapid recombination[104]. Studies done on TiO_2 reveal that electron thermalization in the CB occurs before the recombination or transfer processes[105–108]. The energy can be lost to the lattice via strong coupling with the phonon modes[109]. Hole thermalization in the VB is also accompanied by electron thermalization. It has been found that hole transfer from the TiO_2

VB to hole acceptor competes with hole trapping and charge recombination[110,111]. Upon excitation by UV energy, photogenerated electrons and holes are trapped rapidly within a 100 to 200 fs time range[112]. The trapped electrons reduce Ti^{4+} to Ti^{3+}, where the holes oxidize O^{2-} to O^{-}[103]. Electron traps are believed to be located at the TiO_2 lattices as Ti^{3+} sites lie below the CB edge[113]. Electron trapping is vital for driving the reductive reactions of TiO_2, but it can be detrimental to processes that need fast electron transport; e.g., photovoltaic applications. According to various Electron Spin Resonance studies, it has been proposed that hole trapping occurs at a surface Ti^{4+}-O^{-} site with the hole remaining at an uncoordinated oxygen atom[114].

Photogenerated charge recombination is another important phenomenon that takes place and limits the efficiency of photocatalytic reactions. Recombination occurs following thermalization and trapping that can either take nonradiative (phonon emission) or radiative (photons) pathways. Studies have shown that in rutile, lifetimes of electrons and holes are a few tens of nanoseconds before recombination takes place[115]. Conversely, anatase holes decay within a few seconds while electrons exist in the CB for few microseconds. Compared to rutile, anatase higher photoactivity may be attributed to these long-living electrons.

1.2.2. P25 incorporation into TiO_2 sol-gel

Evonik (formerly Degussa) P25, Aeroxide TiO_2 is a widely used titania photocatalyst with relatively high activity levels in many photocatalytic degradation reactions[116,117]. It has been found that the incorporation of commercially available P25 TiO_2 powder into self-synthesized TiO_2 sols has a positive effect on the photocatalytic degradation efficiency of TiO_2 photocatalysts[118]. TiO_2 surface serves as sites of nucleation

and growth of the self-synthesized TiO_2 particles, affecting the size, number, and physicochemical properties of the TiO_2 crystallites[119,120]. P25 consists of 70% anatase phase and 30% rutile phase and has a surface area of 49 $m^2 g^{-1}$ [121,122]. Due to its high surface area and the coexistence of rutile-anatase phases that allow the increase in charge separation efficiency due to interfacial electron transfer, P25 shows a high activity in degrading organic pollutants[122–125].

1.2.3. Immobilization of photocatalysts

In most of the photocatalytic applications, TiO_2 has been used as an aqueous suspension. Due to its large surface area compared to the immobilized system, TiO_2 suspension shows a higher activity. The use of aqueous suspensions/slurry has a major drawback in commercializing when used in water treatment plants because the separation and recycling of nanosized TiO_2 requires time-consuming and sophisticated ultracentrifugation or microfiltration techniques[126]. On the other hand, the effect of UV light on photocatalytic activity is limited because of strong absorptions and scattering by TiO_2 particles and dissolved organic species[127]. Immobilization of TiO_2 on solid supports is one of the main strategies to circumvent these problems. TiO_2 immobilized on soft, thin substrates is referred to as TiO_2 membranes or filters. Substrates used for TiO_2 membranes are alumina, polyvinylidene difluoride, glass filter, cellulose fibers, magnetic particles, and sponge[124,128–134]. TiO_2 immobilization on rigid substrates has gained more attraction over TiO_2 membranes due to its greater robustness. Different glass substrates (borosilicate, soda-lime glass, and quartz), zeolites, activated carbon, stainless steel, Teflon, fiberglass, cement, brick, and alumina-based ceramics have been used as rigid substrates[126,135–138]. However, TiO_2 immobilization on solid substrates reduces the photocatalytic efficiency

due to various reasons, such as reduction of the active surface, a more difficult exchange of the organic substrate with solution due to mass transfer limitations, and the diffusion of cationic impurities from substrates[139]. Solid supports used for TiO_2 immobilization should have specific characteristics in order to act as efficient photocatalysts: (a) transparency to irradiation, (b) strong surface bonding with the TiO_2 catalyst without negatively affecting the reactivity, (c) high specific surface area, (d) high adsorption affinity for organic compounds, (e) high mass transfer rate facilitating adsorption and separation following photodegradation, and (f) chemical inertness[140]. As such, as an immobilization substrate for photocatalysts, glass is considered as a promising candidate.

1.2.4. Titania-assisted photocatalytic degradation of taste and odor compounds

The use of TiO_2 photocatalysts in the presence of UV light is a more efficient approach than the existing methods for degrading MIB, GSM, and other cyanobacterial toxins due to its higher oxidation power in both distilled and natural waters[60,141–146]; furthermore, it is considered as a green method where there is a potential to reuse the photocatalyst. Several studies have investigated the MIB and GSM photodegradation in the presence of suspended TiO_2 under UV light. These studies are summarized in Table 1.1. In these studies, degradation was investigated in slurry forms for MIB and GSM. According to these studies, the degradation of MIB and GSM followed pseudo first-order kinetics[147,148]. $^{\bullet}OH$ was shown to be the major species that is responsible for the TiO_2-catalyzed photodegradation of MIB and GSM[148]. Increasing irradiation intensity and catalyst loading improved the degradation rates of MIB and GSM up to a certain level[149,150]. There are fewer studies on MIB and GSM photodegradation using immobilized catalyst systems, including the present study (Table 1.2). Degradation experiments that were done

by Pettit et al. (2014) focused on using immobilized catalysts in recirculation aquaculture systems (RAS)[151]. Even though UV-TiO_2 in a slurry reactor can oxidize up to 99% of MIB and GSM[147], it has been found that residual catalyst nanoparticles in such systems have potential adverse effects on fish health[152,153]. In the present study, the incorporation of SiO_2 and TiO_2 into P25 modified coatings increased the catalyst films' robustness without decreasing the photodegradation efficiency of MIB and GSM for multiple cycles[154].

Table 1.1. MIB and GSM photodegradation under suspended TiO_2/ UV reactor systems

Initial MIB/GSM Concentration	**Matrix**	**Experimental features**	**Degradation kinetics**	**Reference**
11.90 nM MIB 10.98 nM GSM	Milli-Q water	Degussa P25 TiO_2 1% 330-550 nm	~99% removal in 60 min $k_{app} = 1.98\times10^{-1}$ min^{-1} (MIB) $k_{app} = 6.33\times10^{-2}$ min^{-1} (GSM)	Lawton et al, 2003[147]
500 µg L^{-1} MIB & GSM	Nano pure water	P25& sol-gel TiO_2 coated Fe_3O_4 40 mg 254 nm	82% removal in 30 min $k_{app} = 8.3\times10^{-1}$ min^{-1} (MIB) $k_{app} = 9.4\times10^{-1}$ min^{-1} (GSM)	Sultana et al,2020[155]
220-1×10^4 ng L^{-1} GSM	Ultra-pure water	Suspended TiO_2 (anatase) 40 mg L^{-1} 365 nm	95.8-99.6 % removal in 60 min k_{app} = 0.021-0.055 min^{-1}	Bamuza et al, 2012[156]
0.1-5 mg L^{-1} GSM	Milli-Q water	Suspended Hombikat K01/C TiO_2 750 g L^{-1} 330-500 nm	70-90% degradation in 25 min	Robertson et al, 2008[157]
0.5-5 mg L^{-1} GSM	Milli-Q water	Pellet Hombikat K01/C TiO_2 750 g L^{-1} 330-500 nm	Complete removal in 25 mins k = 1.56 µM min^{-1}	Bellu et al, 2008[149]
135 mg L^{-1} GSM	Water	Suspended TiO_2 254 nm and 185 nm (4:1 lamps) 20 g L^{-1}	15-27% degradation in 180 min	Pookmanee et al, 2010[158]
0.19 mM MIB	Water	Suspended TiO_2 and Y zeolite 2×10^3 mg L^{-1} 200 W lamps(wavelength is not mentioned)	60% degradation in 220 min	Yoon et al 2007[159]

Table 1.2. MIB and GSM photodegradation under immobilized TiO_2/ UV reactor systems

Initial MIB/GSM Concentration	**Matrix**	**Experimental features**	**Degradation kinetics**	**Reference**
500 ng L^{-1} MIB & GSM	Milli-Q water	Immobilized P25 on glass petri dish 0.5 mg cm^{-2} (Ti ~0.3 mg cm^{-2}) 365 nm	~80% degradation in 60 min k_{app} = 2.4×10^{-2} min^{-1} (MIB) k_{app} = 2.6×10^{-2} min^{-1} (GSM)	Tran et al 2009[148]
50 ng L^{-1} MIB & GSM	Distilled water & recirculating aquaculture system water	Immobilized P25 on a borosilicate glass plate 0.25 mg cm^{-2} (Ti ~0.15 mg cm^{-2}) 350-400 nm	MIB 54% and GSM 60% degradation in 8h k_{app} = 1.4×10^{-3} min^{-1} (MIB_{DI}) k_{app} = 1.5×10^{-3} min^{-1} (MIB_{RAS}) k_{app} = 3.6×10^{-3} min^{-1} (GSM_{DI}) k_{app} = 1.7×10^{-3} min^{-1} (GSM_{RAS})	Pettit et al 2014[151]
500 ng L^{-1}	Nano pure water	Immobilized P25 modified TiO_2-SiO_2 sol gel on glass slide (area=10 cm^2) Ti=0.4 mg cm^{-2} 350 nm	~80% degradation in 60 min k_{app} = 2.86×10^{-2} min^{-1} (MIB) k_{app} = 2.72×10^{-2} min^{-1} (GSM)	Yaparatne at el[154]

1.3. Visible light active photocatalysis

The use of solar radiation in photodegradation of organic compounds is desirable. However, only 4-5% of the total solar spectrum constitutes UV light[160]. As such, many semiconductor photocatalysts do not possess the optical properties to initiate photocatalytic degradation reactions under visible/solar light, mainly due to their wide bandgap, which requires high energy UV irradiation. When developing semiconductor photocatalysts to tackle water contamination in an environmentally benign approach, it is imperative to use the 44% of visible light in the solar spectrum to drive the photocatalytic reactions. Moreover, single component semiconductor materials do not have the quantum and photocatalytic efficiencies due to their high recombination rates of photoinduced charge carriers[160]. In visible light-responsive photocatalysis, the semiconductor should have a narrow band gap (Eg < 3.0 eV) to allow the generation of photoexcited electrons and holes by absorbing light in the range of 400 nm < λ < 800 nm. Alterations such as doping, synthesizing heterostructures or composites, and coupling with π-conjugated architectures have been explored to extend conventional photocatalysts' activities in the visible range[161–163].

Doping a metal or a non-metal into TiO_2 extends its activity to visible light by modifying the TiO_2 band structure. Major substitutional non-metals that have been studied as dopants are C, N, F, P, and S for O in TiO_2[164]. These doped atoms can be introduced as an interstitial dopant, substitutional dopant, or a defect factor in the TiO_2 structure[165]. It was found that when doping N, 2p states of N mix with 2p states of O, which leads to the formation of a new VB with a shifted VB edge to narrow down the bandgap of TiO_2[164].

This was confirmed by detecting isolated N 2p localized states above the VB of TiO_2 experimentally and computationaly[166,167] (Figure 1.7 A). Other than this mechanism, schemes such as the generation of localized states below the TiO_2 CB, increasing the oxygen defect formation, and generation of diamagnetic clusters acting as an electron transfer source under visible light have been proposed to explain the origins of the visible light activity[164]. Additionally, co-doping of two non-metals, which reduces the electron-hole recombination due to intrinsic defects in TiO_2, has been investigated[168] (Figure 1.7 B).

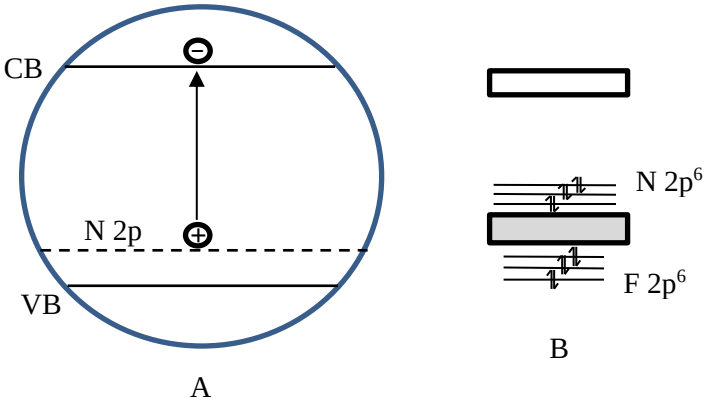

Figure 1.7. (A) Semiconductor bandgap narrowing due to non-metal doping (B) Co-doping non-metals in TiO_2

Doping with noble and transition metals such as Ag, Au, Pt, Pd, Fe, Cu, Co, Ni, Cr, V, Mn, Mo, Nb, W, and Ru has shown an extended response of TiO_2 into the visible region[169]. Metal incorporation forms new energy levels between VB and CB, producing red shifting of TiO_2 light absorption and acting as electron traps inhibiting the electron-hole recombination[170–174].

Dye sensitization is another strategy for achieving visible light-harvesting in wide band gap semiconductors. Electrons are excited from the highest occupied molecular orbital to the lowest unoccupied molecular orbital of a dye during the dye photosensitization. These electrons are subsequently transferred to the CB of TiO_2 surface, which can be scavenged by molecular oxygen to form $^{\bullet}O_2^-$ and $HO_2^{\bullet}$[169].

The construction of heterojunctions or nanocomposites is another approach that induces charge separation and increases visible light absorption. There are four typical categories of heterojunction photocatalyst systems according to its composition:(1) semiconductor-semiconductor heterojunction; (2) semiconductor-metal heterojunction; (3) semiconductor-carbon heterojunction; (4) multi-component heterojunction[161].

Recently, Bi-based semiconductors gained attention as promising candidates for visible light responsive photocatalysts. A variety of Bi-based compounds, such as Bi_2O_3, BiOX (X= Cl, Br, I), $BiVO_4$, Bi_2WO_6, $Bi_4Ti_3O_{12}$, $BiPO_4$, $Bi_2O_2CO_3$, and $BiOCO_2H$, have been used as visible light driven photocatalysts[175]. It has been reported that the VB of Bi-based semiconductors consist of hybrid orbitals of O 2p and Bi 6s[176]. As a result, the well dispersed Bi 6s orbital increases the mobility of the photogenerated charge carriers and decreases the band gap[177,178]. Owing to its cost-effective preparation, availability of precursors, and nontoxicity, Bi_2O_3-based photocatalyst have gained interest in visible light active photocatalyst applications[179,180]. Among Bi_2O_3 crystalline phases, α, β, γ, and δ have been used in photocatalytic applications[181]. Even though Bi_2O_3 is excited by visible light (Bandgap = 2.8 eV), its photocatalytic activity is low due to the photo-corrosion and fast recombination of photogenerated electrons and holes[182]. According to recent studies, using Bi-based multicomponent oxides has been proven to be effectively initiating the visible

light response; TiO_2/Bi_2O_3 heterojunction nanocomposites have shown superior photodegradation ability than TiO_2 alone[183–185]. Upon irradiating with visible light, Bi_2O_3 in TiO_2/Bi_2O_3 composite absorbs radiation and generates holes and electrons. Generated holes at the VB of Bi_2O_3 can be transferred to VB of TiO_2, because the TiO_2 VB is located at a higher level than the Bi_2O_3 VB. The proposed mechanism for TiO_2/Bi_2O_3 composite photodegradation is shown in Figure 1.8[186].

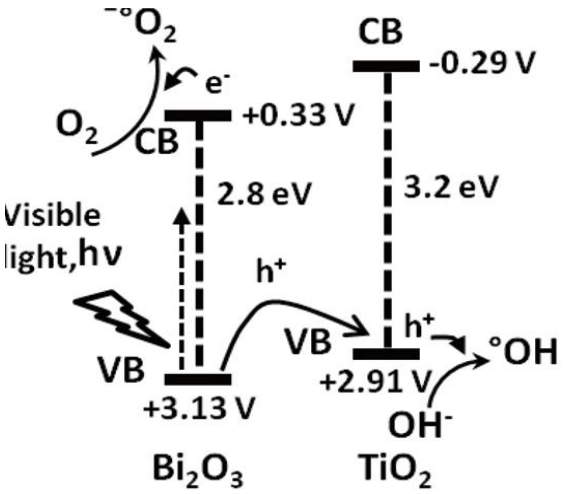

Figure 1.8. Photodegradation scheme for TiO_2/ Bi_2O_3 nanocomposite[186]

Several studies have reported that TiO_2/Bi_2O_3 composites can result in the formation of different bismuth-titanate crystalline phases; e.g., formation of $Bi_4Ti_3O_{12}$ and $Bi_{12}TiO_{20}$ depending on the Bi to Ti ratio[187,188]. In these different types of bismuth-titanate composites, Bi^{3+} species can also be doped into the TiO_2. These impurity levels introduced by Bi lead to an increase in the amount of visible light absorption and an increase in the lifetime of charge carriers[189].

There are limited studies conducted on visible light active catalytic degradation of taste and odor compounds. In particular, Bi-incorporated TiO_2 slurry or immobilized photocatalysts have not been studied for the degradation of these compounds under solar or visible light. Fotiou et al. (2013 & 2016) studied carbon-doped TiO_2 (C-TiO_2) and reduced graphene oxide TiO_2 (GO-TiO_2) for MIB and GSM degradation under the visible/solar light. In their first study, commercially available Kronos vlp-7000 TiO_2 (carbon doped anatase, 87.5%, 15 nm 250 m^2g^{-1})[190,191] was used as the C-TiO_2 and under visible light irradiation (400-700 nm; cutoff filters at 435 nm) degradation was not shown for MIB and GSM[192]. In the second study, simulated solar light irradiation of MIB and GSM in the presence of GO-TiO_2 achieved higher degradation rates than that achieved by the reference anatase TiO_2. However, GO-TiO_2 was slightly less active than P25. Apparent rate constants (k_{app}) for GSM degradation under simulated sunlight with P25 and GO-TiO_2 were 12.6 and 10.1 min^{-1}, respectively. In the same study, k_{app} for MIB degradation under simulated solar light in the presence of same mass of P25 (BET surface area 65 $m^2\,g^{-1}$) and GO-TiO_2 P25 (BET surface area 110 $m^2\,g^{-1}$) were 9.6 and 5.1 min^{-1}, respectively[193,194]. This improved performance in the presence of P25 was attributed to its mixed phase (anatase and rutile), which enables charge separation even under simulated sunlight and above 410 nm[123].

The goal of this work is to develop, characterize, and assess efficient titania-based photocatalysts that can be used for the degradation of persistent organic compounds. Even though UV treatment is currently being used in drinking water treatment plants for disinfection, newly emerging organic compounds are resistant to break down under UV treatment alone. Therefore, it is important to develop a photocatalytic system that will

augment the UV treatment efficiency by extending it into the visible range towards treating contaminated waters. It has been reported that the presence of nanosized photocatalytic particles/slurry usage in water treatment is not feasible due to the challenges in separation of the catalysts. Our work focuses on using a robust immobilized photocatalyst in degradation of two taste and odor compounds that are secreted by species of blue green algae (MIB and GSM). In particular, a titania-silica and P25 based immobilized catalyst was developed, characterized, and activity was assessed for degradation of MIB and GSM under UV irradiation. Further, extending the activity of photocatalyst system into the visible light range was studied by developing bismuth-titanate nano composites.

1.4. REFERENCES

(1) Ibrahim, R. K.; Hayyan, M.; AlSaadi, M. A.; Hayyan, A.; Ibrahim, S. Environmental Application of Nanotechnology: Air, Soil, and Water. *Environmental Science and Pollution Research* **2016**, *23* (14), 13754–13788. https://doi.org/10.1007/s11356-016-6457-z.

(2) Thines, R. K.; Mubarak, N. M.; Nizamuddin, S.; Sahu, J. N.; Abdullah, E. C.; Ganesan, P. Application Potential of Carbon Nanomaterials in Water and Wastewater Treatment: A Review. *Journal of the Taiwan Institute of Chemical Engineers* **2017**, *72*, 116–133. https://doi.org/10.1016/j.jtice.2017.01.018

(3) Amin, M. T.; Alazba, A. A.; Manzoor, U. A Review of Removal of Pollutants from Water/Wastewater Using Different Types of Nanomaterials. *Advances in Materials Science and Engineering* **2014**, *2014*, 1–24. https://doi.org/10.1155/2014/825910.

(4) Apul, O. G.; Karanfil, T. Adsorption of Synthetic Organic Contaminants by Carbon Nanotubes: A Critical Review. *Water Research* **2015**, *68*, 34–55. https://doi.org/10.1016/j.watres.2014.09.032.

(5) Drinking-water https://www.who.int/news-room/fact-sheets/detail/drinking-water (accessed 2020 -04 -22).

(6) Mihelcic, J. R.; Ren, Z. J.; Cornejo, P. K.; Fisher, A.; Simon, A. J.; Snyder, S. W.; Zhang, Q.; Rosso, D.; Huggins, T. M.; Cooper, W.; Moeller, J.; Rose, B.; Schottel, B. L.; Turgeon, J. Accelerating Innovation That Enhances Resource Recovery in the Wastewater Sector: Advancing a National Testbed Network. *Environmental Science & Technology* **2017**, *51* (14), 7749–7758. https://doi.org/10.1021/acs.est.6b05917.

(7) Teodosiu, C.; Gilca, A.-F.; Barjoveanu, G.; Fiore, S. Emerging Pollutants Removal through Advanced Drinking Water Treatment: A Review on Processes and Environmental Performances Assessment. *Journal of Cleaner Production* **2018**, *197*, 1210–1221. https://doi.org/10.1016/j.jclepro.2018.06.247.

(8) Wiegand, C.; Pflugmacher, S. Ecotoxicological Effects of Selected Cyanobacterial Secondary Metabolites a Short Review. *Toxicology and Applied Pharmacology* **2005**, *203* (3), 201–218. https://doi.org/10.1016/j.taap.2004.11.002.

(9) Jeppesen, E.; Kronvang, B.; Meerhoff, M.; Søndergaard, M.; Hansen, K. M.; Andersen, H. E.; Lauridsen, T. L.; Liboriussen, L.; Beklioglu, M.; Özen, A.; Olesen, J. E. Climate Change Effects on Runoff, Catchment Phosphorus Loading and Lake Ecological State, and Potential Adaptations. *Journal of Environment Quality* **2009**, *38* (5), 1930. https://doi.org/10.2134/jeq2008.0113.

(10) Ptacnik, R.; Lepistö, L.; Willén, E.; Brettum, P.; Andersen, T.; Rekolainen, S.; Solheim, A. L.; Carvalho, L. Quantitative Responses of Lake Phytoplankton to Eutrophication in Northern Europe. *Aquat Ecol* **2008**, *42* (2), 227–236. https://doi.org/10.1007/s10452-008-9181-z.

(11) Paerl, H. W.; Hall, N. S.; Calandrino, E. S. Controlling Harmful Cyanobacterial Blooms in a World Experiencing Anthropogenic and Climatic-Induced Change. *Science of The Total Environment* **2011**, *409* (10), 1739–1745. https://doi.org/10.1016/j.scitotenv.2011.02.001.

(12) Wetzel, R. G. 15 - Planktonic Communities: Algae And Cyanobacteria. In *Limnology (Third Edition)*; Academic Press: San Diego, 2001; pp 331–393. https://doi.org/10.1016/B978-0-08-057439-4.50019-8.

(13) Boström, B.; Andersen, J. M.; Fleischer, S.; Jansson, M. Exchange of Phosphorus across the Sediment-Water Interface. *Hydrobiologia* **1988**, *170* (1), 229–244. https://doi.org/10.1007/BF00024907.

(14) Shang, L.; Feng, M.; Xu, X.; Liu, F.; Ke, F.; Li, W. Co-Occurrence of Microcystins and Taste-and-Odor Compounds in Drinking Water Source and Their Removal in a Full-Scale Drinking Water Treatment Plant. *Toxins* **2018**, *10* (1), 26. https://doi.org/10.3390/toxins10010026.

(15) Watson, S. B. Aquatic Taste and Odor: A Primary Signal of Drinking-Water Integrity. *Journal of Toxicology and Environmental Health, Part A* **2004**, *67* (20–22), 1779–1795. https://doi.org/10.1080/15287390490492377.

(16) Klausen, C.; Nicolaisen, M. H.; Strobel, B. W.; Warnecke, F.; Nielsen, J. L.; Jørgensen, N. O. G. Abundance of Actinobacteria and Production of Geosmin and 2-Methylisoborneol in Danish Streams and Fish Ponds. *FEMS Microbiol Ecol* **2005**, *52* (2), 265–278. https://doi.org/10.1016/j.femsec.2004.11.015.

(17) Smith, J. L.; Boyer, G. L.; Zimba, P. V. A Review of Cyanobacterial Odorous and Bioactive Metabolites: Impacts and Management Alternatives in Aquaculture. *Aquaculture* **2008**, *280* (1–4), 5–20. https://doi.org/10.1016/j.aquaculture.2008.05.007.

(18) Lee, J.; Rai, P. K.; Jeon, Y. J.; Kim, K.-H.; Kwon, E. E. The Role of Algae and Cyanobacteria in the Production and Release of Odorants in Water. *Environmental Pollution* **2017**, *227*, 252–262. https://doi.org/10.1016/j.envpol.2017.04.058.

(19) Cook, D.; Newcombe, G.; Sztajnbok, P. The Application of Powdered Activated Carbon for MIB and Geosmin Removal: Predicting PAC Doses in Four Raw Waters. *Water Res.* **2001**, *35* (5), 1325–1333.

(20) Jung, S. W.; Baek, K. H.; Yu, M. J. Treatment of Taste and Odor Material by Oxidation and Adsorption. *Water Sci. Technol.* **2004**, *49* (9), 289–295.

(21) Jr, C. T.; Mt, B.; Dw, M. Improvement of Thermal Reactivation of Activated Carbon for the Removal of 2-Methylisoborneol. *Water Res* **2007**, *41* (1), 79–86. https://doi.org/10.1016/j.watres.2006.09.010.

(22) Yao, W.; Qu, Q.; von Gunten, U.; Chen, C.; Yu, G.; Wang, Y. Comparison of Methylisoborneol and Geosmin Abatement in Surface Water by Conventional Ozonation and an Electro-Peroxone Process. *Water Research* **2017**, *108*, 373–382. https://doi.org/10.1016/j.watres.2016.11.014.

(23) Rosenfeldt, E. J.; Melcher, B.; Linden, K. G. UV and UV/H_2O_2 Treatment of Methylisoborneol (MIB) and Geosmin in Water. *Journal of Water Supply: Research and Technology - Aqua* **2005**, *54* (7), 423–434.

(24) Szewzyk, U.; Szewzyk, R.; Manz, W.; Schleifer, K.-H. Microbiological Safety of Drinking Water. *Annual Review of Microbiology* **2000**, *54* (1), 81–127. https://doi.org/10.1146/annurev.micro.54.1.81.

(25) Zhang, W.; DiGiano, F. A. Comparison of Bacterial Regrowth in Distribution Systems Using Free Chlorine and Chloramine: A Statistical Study of Causative Factors. *Water Research* **2002**, *36* (6), 1469–1482. https://doi.org/10.1016/S0043-1354(01)00361-X.

(26) Hozalski, R. M.; Zhang, L.; Arnold, W. A. Reduction of Haloacetic Acids by Fe^0 : Implications for Treatment and Fate. *Environmental Science & Technology* **2001**, *35* (11), 2258–2263. https://doi.org/10.1021/es001785b.

(27) Becher, G. Drinking Water Chlorination and Health. *Acta hydrochimica et hydrobiologica* **1999**,*27* (2), 100–102. https://doi.org/10.1002/(SICI)1521-401X(199902)27:2<100::AID-AHEH100>3.0.CO;2-A.

(28) Sadiq, R.; Rodriguez, M. Disinfection By-Products (DBPs) in Drinking Water and Predictive Models for Their Occurrence: A Review. *Science of The Total Environment* **2004**, *321* (1–3), 21–46. https://doi.org/10.1016/j.scitotenv.2003.05.001.

(29) Gopal, K.; Tripathy, S. S.; Bersillon, J. L.; Dubey, S. P. Chlorination Byproducts, Their Toxicodynamics and Removal from Drinking Water. *Journal of Hazardous Materials* **2007**, *140* (1–2), 1–6. https://doi.org/10.1016/j.jhazmat.2006.10.063.

(30) Suffet, I. H.; Ho, J.; Chou, D.; Khiari, D.; Mallevialle, J. Taste-and-Odor Problems Observed during Drinking Water Treatment. *Advances in taste and odor treatment and control* **1995**, 1–21.

(31) Sun, A.; Xiong, Z.; Xu, Y. Removal of Malodorous Organic Sulfides with Molecular Oxygen and Visible Light over Metal Phthalocyanine. *Journal of Hazardous Materials* **2008**, *152* (1), 191–195. https://doi.org/10.1016/j.jhazmat.2007.06.105.

(32) Antonopoulou, M.; Evgenidou, E.; Lambropoulou, D.; Konstantinou, I. A Review on Advanced Oxidation Processes for the Removal of Taste and Odor Compounds from Aqueous Media. *Water Research* **2014**, *53*, 215–234. https://doi.org/10.1016/j.watres.2014.01.028.

(33) Mehrjouei, M.; Müller, S.; Möller, D. A Review on Photocatalytic Ozonation Used for the Treatment of Water and Wastewater. *Chemical Engineering Journal* **2015**, *263*, 209–219. https://doi.org/10.1016/j.cej.2014.10.112.

(34) Beltrán, F. J.; Rivas, F. J.; Gimeno, O.; Carbajo, M. Photocatalytic Enhanced Oxidation of Fluorene in Water with Ozone. Comparison with Other Chemical Oxidation Methods. *Industrial & Engineering Chemistry Research* **2005**, *44* (10), 3419–3425. https://doi.org/10.1021/ie048800w.

(35) Beltrán, F. J.; Aguinaco, A.; Rey, A.; García-Araya, J. F. Kinetic Studies on Black Light Photocatalytic Ozonation of Diclofenac and Sulfamethoxazole in Water. *Industrial & Engineering Chemistry Research* **2012**, *51* (12), 4533–4544. https://doi.org/10.1021/ie202525f.

(36) von Gunten, U. Ozonation of Drinking Water: Part I. Oxidation Kinetics and Product Formation. *Water Research* **2003**, *37* (7), 1443–1467. https://doi.org/10.1016/S0043-1354(02)00457-8.

(37) Adams, C.; Wang, Y.; Loftin, K.; Meyer, M. Removal of Antibiotics from Surface and Distilled Water in Conventional Water Treatment Processes. *Journal of Environmental Engineering* **2002**, *128* (3), 253–260. https://doi.org/10.1061/(ASCE)0733-9372(2002)128:3(253).

(38) Tan, C.; Gao, N.; Zhou, S.; Xiao, Y.; Zhuang, Z. Kinetic Study of Acetaminophen Degradation by UV-Based Advanced Oxidation Processes. *Chemical Engineering Journal* **2014**, *253*, 229–236. https://doi.org/10.1016/j.cej.2014.05.013.

(39) Han, M.; Mohseni, M. Impact of Organic and Inorganic Carbon on the Formation of Nitrite during the VUV Photolysis of Nitrate Containing Water. *Water Research* **2020**, *168*, 115169. https://doi.org/10.1016/j.watres.2019.115169.

(40) Prabha, I.; Lathasree, S. Photodegradation of Phenol by Zinc Oxide, Titania and Zinc Oxide–Titania Composites: Nanoparticle Synthesis, Characterization and Comparative Photocatalytic Efficiencies. *Materials Science in Semiconductor Processing* **2014**, *26*, 603–613. https://doi.org/10.1016/j.mssp.2014.05.031.

(41) Calace, N.; Nardi, E.; Petronio, B. M.; Pietroletti, M. Adsorption of Phenols by Papermill Sludges. *Environ Pollut* **2002**, *118* (3), 315–319. https://doi.org/10.1016/s0269-7491(01)00303-7.

(42) McCall, J.; Alexander, C.; Richter, M. M. Quenching of Electrogenerated Chemiluminescence by Phenols, Hydroquinones, Catechols, and Benzoquinones. *Anal. Chem.* **1999**, *71* (13), 2523–2527. https://doi.org/10.1021/ac981322c.

(43) Hasanoğlu, A. Removal of Phenol from Wastewaters Using Membrane Contactors: Comparative Experimental Analysis of Emulsion Pertraction. *Desalination* **2013**, *309*, 171–180. https://doi.org/10.1016/j.desal.2012.10.004.

(44) Padmanabhan, P. V. A.; Sreekumar, K. P.; Thiyagarajan, T. K.; Satpute, R. U.; Bhanumurthy, K.; Sengupta, P.; Dey, G. K.; Warrier, K. G. K. Nano-Crystalline Titanium Dioxide Formed by Reactive Plasma Synthesis. *Vacuum* **2006**, *80* (11), 1252–1255. https://doi.org/10.1016/j.vacuum.2006.01.054.

(45) Gaya, U. I.; Abdullah, A. H. Heterogeneous Photocatalytic Degradation of Organic Contaminants over Titanium Dioxide: A Review of Fundamentals, Progress and Problems. *Journal of Photochemistry and Photobiology C: Photochemistry Reviews* **2008**, *9* (1), 1–12. https://doi.org/10.1016/j.jphotochemrev.2007.12.003.

(46) Chong, M. N.; Jin, B.; Chow, C. W. K.; Saint, C. Recent Developments in Photocatalytic Water Treatment Technology: A Review. *Water Research* **2010**, *44* (10), 2997–3027. https://doi.org/10.1016/j.watres.2010.02.039.

(47) Comninellis, C.; Kapalka, A.; Malato, S.; Parsons, S. A.; Poulios, I.; Mantzavinos, D. Advanced Oxidation Processes for Water Treatment: Advances and Trends for R&D. *Journal of Chemical Technology & Biotechnology* **2008**, *83* (6), 769–776. https://doi.org/10.1002/jctb.1873.

(48) Klavarioti, M.; Mantzavinos, D.; Kassinos, D. Removal of Residual Pharmaceuticals from Aqueous Systems by Advanced Oxidation Processes. *Environment International* **2009**, *35* (2), 402–417. https://doi.org/10.1016/j.envint.2008.07.009.

(49) Yang, Y.; Pignatello, J. J.; Ma, J.; Mitch, W. A. Comparison of Halide Impacts on the Efficiency of Contaminant Degradation by Sulfate and Hydroxyl Radical-Based Advanced Oxidation Processes (AOPs). *Environmental Science & Technology* **2014**, *48* (4), 2344–2351. https://doi.org/10.1021/es404118q.

(50) Giannakis, S.; Gamarra Vives, F. A.; Grandjean, D.; Magnet, A.; De Alencastro, L. F.; Pulgarin, C. Effect of Advanced Oxidation Processes on the Micropollutants and the Effluent Organic Matter Contained in Municipal Wastewater Previously Treated by Three Different Secondary Methods. *Water Research* **2015**, *84*, 295–306. https://doi.org/10.1016/j.watres.2015.07.030.

(51) Stefan, M. I. *Advanced Oxidation Processes for Water Treatment: Fundamentals and Applications*; IWA publishing, 2017.

(52) Bolton, J. R.; Bircher, K. G.; Tumas, W.; Tolman, C. A. Figures-of-Merit for the Technical Development and Application of Advanced Oxidation Processes. *Journal of advanced oxidation technologies* **1996**, *1* (1), 13–17.

(53) Bolton, J. R.; Bircher, K. G.; Tumas, W.; Tolman, C. A. Figures-of-Merit for the Technical Development and Application of Advanced Oxidation Technologies for Both Electric- and Solar-Driven Systems (IUPAC Technical Report). *Pure and Applied Chemistry* **2001**, *73* (4), 627–637. https://doi.org/10.1351/pac200173040627.

(54) Staehelin, Johannes.; Hoigne, Juerg. Decomposition of Ozone in Water in the Presence of Organic Solutes Acting as Promoters and Inhibitors of Radical Chain Reactions. *Environmental Science & Technology* **1985**, *19* (12), 1206–1213. https://doi.org/10.1021/es00142a012.

(55) Sharma, A.; Ahmad, J.; Flora, S. J. S. Application of Advanced Oxidation Processes and Toxicity Assessment of Transformation Products. *Environmental Research* **2018**, *167*, 223–233. https://doi.org/10.1016/j.envres.2018.07.010.

(56) Tarr, M. A. *Chemical Degradation Methods for Wastes and Pollutants: Environmental and Industrial Applications*; CRC press, 2003.

(57) Miklos, D. B.; Remy, C.; Jekel, M.; Linden, K. G.; Drewes, J. E.; Hübner, U. Evaluation of Advanced Oxidation Processes for Water and Wastewater Treatment – A Critical Review. *Water Research* **2018**, *139*, 118–131. https://doi.org/10.1016/j.watres.2018.03.042.

(58) Sillanpää, M.; Ncibi, M. C.; Matilainen, A. Advanced Oxidation Processes for the Removal of Natural Organic Matter from Drinking Water Sources: A Comprehensive Review. *Journal of Environmental Management* **2018**, *208*, 56–76. https://doi.org/10.1016/j.jenvman.2017.12.009.

(59) Song, K.; Mohseni, M.; Taghipour, F. Application of Ultraviolet Light-Emitting Diodes (UV-LEDs) for Water Disinfection: A Review. *Water Research* **2016**, *94*, 341–349. https://doi.org/10.1016/j.watres.2016.03.003.

(60) Munter, R. Advanced Oxidation Processes–Current Status and Prospects. *Proc. Estonian Acad. Sci. Chem* **2001**, *50* (2), 59–80.

(61) Ike, I. A.; Linden, K. G.; Orbell, J. D.; Duke, M. Critical Review of the Science and Sustainability of Persulphate Advanced Oxidation Processes. *Chemical Engineering Journal* **2018**, *338*, 651–669. https://doi.org/10.1016/j.cej.2018.01.034.

(62) Wacławek, S.; Lutze, H. V.; Grübel, K.; Padil, V. V. T.; Černík, M.; Dionysiou, Dionysios. D. Chemistry of Persulfates in Water and Wastewater Treatment: A Review. *Chemical Engineering Journal* **2017**, *330*, 44–62. https://doi.org/10.1016/j.cej.2017.07.132.

(63) Ahn, Y.; Lee, D.; Kwon, M.; Choi, I.; Nam, S.-N.; Kang, J.-W. Characteristics and Fate of Natural Organic Matter during UV Oxidation Processes. *Chemosphere* **2017**, *184*, 960–968. https://doi.org/10.1016/j.chemosphere.2017.06.079.

(64) Watts, M. J.; Linden, K. G. Chlorine Photolysis and Subsequent OH Radical Production during UV Treatment of Chlorinated Water. *Water Research* **2007**, *41* (13), 2871–2878. https://doi.org/10.1016/j.watres.2007.03.032.

(65) Fang, J.; Fu, Y.; Shang, C. The Roles of Reactive Species in Micropollutant Degradation in the UV/Free Chlorine System. *Environmental Science & Technology* **2014**, *48* (3), 1859–1868. https://doi.org/10.1021/es4036094.

(66) Ruppert, G.; Bauer, R.; Heisler, G. The Photo-Fenton Reaction — an Effective Photochemical Wastewater Treatment Process. *Journal of Photochemistry and Photobiology A: Chemistry* **1993**, *73* (1), 75–78. https://doi.org/10.1016/1010-6030(93)80035-8.

(67) *Applications of Advanced Oxidation Processes (AOPs) in Drinking Water Treatment*; Gil, A., Galeano, L. A., Vicente, M. Á., Eds.; The Handbook of Environmental Chemistry; Springer International Publishing: Cham, 2019; Vol. 67. https://doi.org/10.1007/978-3-319-76882-3.

(68) Dong, S.; Feng, J.; Fan, M.; Pi, Y.; Hu, L.; Han, X.; Liu, M.; Sun, J.; Sun, J. Recent Developments in Heterogeneous Photocatalytic Water Treatment Using Visible Light-Responsive Photocatalysts: A Review. *RSC Advances* **2015**, *5* (19), 14610–14630. https://doi.org/10.1039/C4RA13734E.

(69) Tratnyek, P. G.; Johnson, R. L. Nanotechnologies for Environmental Cleanup. *Nano Today* **2006**, *1* (2), 44–48. https://doi.org/10.1016/S1748-0132(06)70048-2.

(70) Guerra, F.; Attia, M.; Whitehead, D.; Alexis, F. Nanotechnology for Environmental Remediation: Materials and Applications. *Molecules* **2018**, *23* (7), 1760. https://doi.org/10.3390/molecules23071760.

(71) Advanced-Oxidation-Processes-for-Water-Treatment-Chemical-Processes.Pdf.

(72) Stark, W. J.; Stoessel, P. R.; Wohlleben, W.; Hafner, A. Industrial Applications of Nanoparticles. *Chemical Society Reviews* **2015**, *44* (16), 5793–5805. https://doi.org/10.1039/C4CS00362D.

(73) Ciambelli, P.; La Guardia, G.; Vitale, L. Chapter 7 - Nanotechnology for Green Materials and Processes. In *Studies in Surface Science and Catalysis*; Basile, A., Centi, G., Falco, M. D., Iaquaniello, G., Eds.; Catalysis, Green Chemistry and

Sustainable Energy; Elsevier, 2019; Vol. 179, pp 97–116. https://doi.org/10.1016/B978-0-444-64337-7.00007-0.

(74) Saikia, J.; Gogoi, A.; Baruah, S. Nanotechnology for Water Remediation. In *Environmental Nanotechnology*; Dasgupta, N., Ranjan, S., Lichtfouse, E., Eds.; Environmental Chemistry for a Sustainable World; Springer International Publishing: Cham, 2019; Vol. 21, pp 195–211. https://doi.org/10.1007/978-3-319-98708-8_7.

(75) Malato, S.; Fernández-Ibáñez, P.; Maldonado, M. I.; Blanco, J.; Gernjak, W. Decontamination and Disinfection of Water by Solar Photocatalysis: Recent Overview and Trends. *Catalysis Today* **2009**, *147* (1), 1–59. https://doi.org/10.1016/j.cattod.2009.06.018.

(76) Ahmed, S. N.; Haider, W. Heterogeneous Photocatalysis and Its Potential Applications in Water and Wastewater Treatment: A Review. *Nanotechnology* **2018**, *29* (34), 342001. https://doi.org/10.1088/1361-6528/aac6ea.

(77) Fujishima, A.; Honda, K. Electrochemical Photolysis of Water at a Semiconductor Electrode. *nature* **1972**, *238* (5358), 37–38.

(78) Zhang, J.; Wu, Y.; Xing, M.; Leghari, S. A. K.; Sajjad, S. Development of Modified N Doped TiO2 Photocatalyst with Metals, Nonmetals and Metal Oxides. *Energy & Environmental Science* **2010**, *3* (6), 715. https://doi.org/10.1039/b927575d.

(79) Ouyang, J.; Chang, M.; Li, X. CdS-Sensitized ZnO Nanorod Arrays Coated with TiO2 Layer for Visible Light Photoelectrocatalysis. *Journal of Materials Science* **2012**, *47* (9), 4187–4193. https://doi.org/10.1007/s10853-012-6273-x.

(80) Di Valentin, C.; Finazzi, E.; Pacchioni, G.; Selloni, A.; Livraghi, S.; Paganini, M. C.; Giamello, E. N-Doped TiO_2: Theory and Experiment. *Chemical Physics* **2007**, *339* (1–3), 44–56. https://doi.org/10.1016/j.chemphys.2007.07.020.

(81) Robert, D. Photosensitization of TiO_2 by MxOy and MxSy Nanoparticles for Heterogeneous Photocatalysis Applications. *Catalysis Today* **2007**, *122* (1–2), 20–26. https://doi.org/10.1016/j.cattod.2007.01.060.

(82) Kandiel, T. A.; Robben, L.; Alkaim, A.; Bahnemann, D. Brookite versus Anatase TiO_2 Photocatalysts: Phase Transformations and Photocatalytic Activities.

Photochem. Photobiol. Sci. **2013**, *12* (4), 602–609. https://doi.org/10.1039/C2PP25217A.

(83) Yan, J.; Wu, G.; Guan, N.; Li, L.; Li, Z.; Cao, X. Understanding the Effect of Surface/Bulk Defects on the Photocatalytic Activity of TiO_2: Anatase versus Rutile. *Physical Chemistry Chemical Physics* **2013**, *15* (26), 10978. https://doi.org/10.1039/c3cp50927c.

(84) Carp, O. Photoinduced Reactivity of Titanium Dioxide. *Progress in Solid State Chemistry* **2004**, *32* (1–2), 33–177. https://doi.org/10.1016/j.progsolidstchem.2004.08.001.

(85) Zhang, J.; Zhou, P.; Liu, J.; Yu, J. New Understanding of the Difference of Photocatalytic Activity among Anatase, Rutile and Brookite TiO_2. *Phys. Chem. Chem. Phys.* **2014**, *16* (38), 20382–20386. https://doi.org/10.1039/C4CP02201G.

(86) Luttrell, T.; Halpegamage, S.; Tao, J.; Kramer, A.; Sutter, E.; Batzill, M. Why Is Anatase a Better Photocatalyst than Rutile? - Model Studies on Epitaxial TiO_2 Films. *Scientific Reports* **2015**, *4* (1). https://doi.org/10.1038/srep04043.

(87) Zhang, Z.; Wang, C.-C.; Zakaria, R.; Ying, J. Y. Role of Particle Size in Nanocrystalline TiO_2-Based Photocatalysts. 8.

(88) Zhang, Q.; Gao, L.; Guo, J. Effects of Calcination on the Photocatalytic Properties of Nanosized TiO_2 Powders Prepared by TiCl4 Hydrolysis. **2000**, 9.

(89) Fox, M. A.; Dulay, M. T. Heterogeneous Photocatalysis. 17.

(90) Kesselman, J. M.; Shreve, G. A.; Hoffmann, M. R.; Lewis, N. S. Flux-Matching Conditions at TiO_2 Photoelectrodes: Is Interfacial Electron Transfer to O2 Rate-Limiting in the TiO_2-Catalyzed Photochemical Degradation of Organics? 11.

(91) Xu, M.; Gao, Y.; Moreno, E. M.; Kunst, M.; Muhler, M.; Wang, Y.; Idriss, H.; Wöll, C. Photocatalytic Activity of Bulk TiO 2 Anatase and Rutile Single Crystals Using Infrared Absorption Spectroscopy. *Physical Review Letters* **2011**, *106* (13). https://doi.org/10.1103/PhysRevLett.106.138302.

(92) Zhang, L.; Menendez-Flores, V. M.; Murakami, N.; Ohno, T. Improvement of Photocatalytic Activity of Brookite Titanium Dioxide Nanorods by Surface Modification Using Chemical Etching. *Applied Surface Science* **2012**, *258* (15), 5803–5809. https://doi.org/10.1016/j.apsusc.2012.02.103.

(93) Ismail, A. A.; Kandiel, T. A.; Bahnemann, D. W. Novel (and Better?) Titania-Based Photocatalysts: Brookite Nanorods and Mesoporous Structures. *Journal of Photochemistry and Photobiology A: Chemistry* **2010**, *216* (2–3), 183–193. https://doi.org/10.1016/j.jphotochem.2010.05.016.

(94) Allen, N. S.; Mahdjoub, N.; Vishnyakov, V.; Kelly, P. J.; Kriek, R. J. The Effect of Crystalline Phase (Anatase, Brookite and Rutile) and Size on the Photocatalytic Activity of Calcined Polymorphic Titanium Dioxide (TiO 2). *Polymer Degradation and Stability* **2018**, *150*, 31–36. https://doi.org/10.1016/j.polymdegradstab.2018.02.008.

(95) Vequizo, J. J. M.; Matsunaga, H.; Ishiku, T.; Kamimura, S.; Ohno, T.; Yamakata, A. Trapping-Induced Enhancement of Photocatalytic Activity on Brookite TiO_2 Powders: Comparison with Anatase and Rutile TiO_2 Powders. *ACS Catalysis* **2017**, *7* (4), 2644–2651. https://doi.org/10.1021/acscatal.7b00131.

(96) Wang, H.; Gao, X.; Duan, G.; Yang, X.; Liu, X. Facile Preparation of Anatase–Brookite–Rutile Mixed-Phase N-Doped TiO_2 with High Visible-Light Photocatalytic Activity. *Journal of Environmental Chemical Engineering* **2015**, *3* (2), 603–608. https://doi.org/10.1016/j.jece.2015.02.006.

(97) Jiang, X.; Manawan, M.; Feng, T.; Qian, R.; Zhao, T.; Zhou, G.; Kong, F.; Wang, Q.; Dai, S.; Pan, J. H. Anatase and Rutile in Evonik Aeroxide P25: Heterojunctioned or Individual Nanoparticles? *Catalysis Today* **2018**, *300*, 12–17. https://doi.org/10.1016/j.cattod.2017.06.010.

(98) Shimura, K.; Yoshida, H. Heterogeneous Photocatalytic Hydrogen Production from Water and Biomass Derivatives. *Energy & Environmental Science* **2011**, *4* (7), 2467. https://doi.org/10.1039/c1ee01120k.

(99) Fischer, S.; Munz, A. W.; Schierbaum, K.-D.; Göpel, W. The Geometric Structure of Intrinsic Defects at TiO_2(110) Surfaces: An STM Study. *Surface Science* **1995**, *337* (1–2), 17–30. https://doi.org/10.1016/0039-6028(95)00572-2.

(100) Woicik, J. C.; Nelson, E. J.; Kronik, L.; Jain, M.; Chelikowsky, J. R.; Heskett, D.; Berman, L. E.; Herman, G. S. Hybridization and Bond-Orbital Components in Site-Specific X-Ray Photoelectron Spectra of Rutile TiO_2. *Physical Review Letters* **2002**, *89* (7). https://doi.org/10.1103/PhysRevLett.89.077401.

(101) Prasad, C.; Tang, H.; Liu, Q. Q.; Zulfiqar, S.; Shah, S.; Bahadur, I. An Overview of Semiconductors/Layered Double Hydroxides Composites: Properties, Synthesis, Photocatalytic and Photoelectrochemical Applications. *Journal of Molecular Liquids* **2019**, *289*, 111114. https://doi.org/10.1016/j.molliq.2019.111114.

(102) Fujishima, A.; Rao, T. N.; Tryk, D. A. Titanium Dioxide Photocatalysis. *Journal of Photochemistry and Photobiology C: Photochemistry Reviews* **2000**, *1* (1), 1–21.

(103) Guo, Q.; Zhou, C.; Ma, Z.; Yang, X. Fundamentals of TiO_2 Photocatalysis: Concepts, Mechanisms, and Challenges. *Advanced Materials* **2019**, *31* (50), 1901997. https://doi.org/10.1002/adma.201901997.

(104) Hoffmann, M. R.; Martin, S. T.; Choi, W.; Bahnemann, D. W. Environmental Applications of Semiconductor Photocatalysis. *Chemical reviews* **1995**, *95* (1), 69–96.

(105) Yamada, Y.; Kanemitsu, Y. Blue Photoluminescence of Highly Photoexcited Rutile TiO 2 : Nearly Degenerate Conduction-Band Effects. *Physical Review B* **2010**, *82* (11). https://doi.org/10.1103/PhysRevB.82.113103.

(106) Yamada, Y.; Kanemitsu, Y. Photoluminescence Spectrum and Dynamics in Highly Photoexcited Rutile TiO_2. *physica status solidi (c)* **2011**, *8* (1), 104–107. https://doi.org/10.1002/pssc.201000642.

(107) Sporleder, D.; Wilson, D. P.; White, M. G. Final State Distributions of O_2 Photodesorbed from TiO 2 (110). *The Journal of Physical Chemistry C* **2009**, *113* (30), 13180–13191. https://doi.org/10.1021/jp901065j.

(108) Diwald, O.; Thompson, T. L.; Goralski, E. G.; Walck, S. D.; Yates, J. T. The Effect of Nitrogen Ion Implantation on the Photoactivity of TiO 2 Rutile Single Crystals. *The Journal of Physical Chemistry B* **2004**, *108* (1), 52–57. https://doi.org/10.1021/jp030529t.

(109) J. C., Xu, Y.-J., Eds.; Green Chemistry and Sustainable Technology; Springer Berlin Heidelberg: Berlin, *Heterogeneous Photocatalysis*; Colmenares, **2016**. https://doi.org/10.1007/978-3-662-48719-8.

(110) Colombo, D. P.; Bowman, R. M. Does Interfacial Charge Transfer Compete with Charge Carrier Recombination? A Femtosecond Diffuse Reflectance Investigation of TiO $_2$ Nanoparticles. *The Journal of Physical Chemistry* **1996**, *100* (47), 18445–18449. https://doi.org/10.1021/jp9610628.

(111) Yang, X.; Tamai, N. How Fast Is Interfacial Hole Transfer? In Situ Monitoring of Carrier Dynamics in Anatase TiO_2 Nanoparticles by Femtosecond Laser Spectroscopy. *Physical Chemistry Chemical Physics* **2001**, *3* (16), 3393–3398. https://doi.org/10.1039/b101721g.

(112) Tamaki, Y.; Hara, K.; Katoh, R.; Tachiya, M.; Furube, A. Femtosecond Visible-to-IR Spectroscopy of TiO_2 Nanocrystalline Films: Elucidation of the Electron Mobility before Deep Trapping. *The Journal of Physical Chemistry C* **2009**, *113* (27), 11741–11746. https://doi.org/10.1021/jp901833j.

(113) Uetsuka, H.; Onishi, H.; Henderson, M. A.; White, J. M. Photoinduced Redox Reaction Coupled with Limited Electron Mobility at Metal Oxide Surface. *The Journal of Physical Chemistry B* **2004**, *108* (30), 10621–10624. https://doi.org/10.1021/jp0484027.

(114) Diebold, U. The Surface Science of Titanium Dioxide. *Surface Science Reports* **2003**, *48* (5–8), 53–229. https://doi.org/10.1016/S0167-5729(02)00100-0.

(115) Yamada, Y.; Kanemitsu, Y. Determination of Electron and Hole Lifetimes of Rutile and Anatase TiO_2 Single Crystals. *Applied Physics Letters* **2012**, *101* (13), 133907. https://doi.org/10.1063/1.4754831.

(116) Baccaro, A. L. B.; Gutz, I. G. R. Quick Cold Preparation of TiO_2 Nanolayers on Gold from P25 Suspensions – Film Structure, Voltammetric Behavior and Photocatalytic Performance for the Oxidation of EDTA under UVA-LED Irradiation. *Electrochimica Acta* **2016**, *214*, 295–306. https://doi.org/10.1016/j.electacta.2016.08.048.

(117) Kelesidis, G. A.; Goudeli, E.; Pratsinis, S. E. Flame Synthesis of Functional Nanostructured Materials and Devices: Surface Growth and Aggregation. *Proceedings of the Combustion Institute* **2017**, *36* (1), 29–50. https://doi.org/10.1016/j.proci.2016.08.078.

(118) Sreethawong, T.; Ngamsinlapasathian, S.; Yoshikawa, S. Positive Role of Incorporating P-25 TiO_2 to Mesoporous-Assembled TiO_2 Thin Films for Improving Photocatalytic Dye Degradation Efficiency. *Journal of Colloid and Interface Science* **2014**, *430*, 184–192. https://doi.org/10.1016/j.jcis.2014.05.032.

(119) Balasubramanian, G.; Dionysiou, D. D.; Suidan, M. T.; Subramanian, V.; Baudin, I.; Laîné, J.-M. Titania Powder Modified Sol-Gel Process for Photocatalytic Applications. *Journal of materials science* **2003**, *38* (4), 823–831.

(120) Chen, Y.; Dionysiou, D. D. TiO_2 Photocatalytic Films on Stainless Steel: The Role of Degussa P-25 in Modified Sol–Gel Methods. *Applied Catalysis B: Environmental* **2006**, *62* (3–4), 255–264. https://doi.org/10.1016/j.apcatb.2005.07.017.

(121) Ohno, T.; Sarukawa, K.; Tokieda, K.; Matsumura, M. Morphology of a TiO_2 Photocatalyst (Degussa, P-25) Consisting of Anatase and Rutile Crystalline Phases. *Journal of Catalysis* **2001**, *203* (1), 82–86. https://doi.org/10.1006/jcat.2001.3316.

(122) Jafry, H. R.; Liga, M. V.; Li, Q.; Barron, A. R. Simple Route to Enhanced Photocatalytic Activity of P25 Titanium Dioxide Nanoparticles by Silica Addition. *Environmental Science & Technology* **2011**, *45* (4), 1563–1568. https://doi.org/10.1021/es102749e.

(123) Hurum, D. C.; Agrios, A. G.; Gray, K. A.; Rajh, T.; Thurnauer, M. C. Explaining the Enhanced Photocatalytic Activity of Degussa P25 Mixed-Phase TiO_2 Using EPR. *J. Phys. Chem. B* **2003**, *107* (19), 4545–4549. https://doi.org/10.1021/jp0273934.

(124) Li, F.; Zhao, Y.; Hao, Y.; Wang, X.; Liu, R.; Zhao, D.; Chen, D. N-Doped P25 TiO_2–Amorphous Al_2O_3 Composites: One-Step Solution Combustion Preparation and Enhanced Visible-Light Photocatalytic Activity. *Journal of Hazardous Materials* **2012**, *239–240*, 118–127. https://doi.org/10.1016/j.jhazmat.2012.08.016.

(125) Scanlon, D. O.; Dunnill, C. W.; Buckeridge, J.; Shevlin, S. A.; Logsdail, A. J.; Woodley, S. M.; Catlow, C. R. A.; Powell, Michael. J.; Palgrave, R. G.; Parkin, I. P.; Watson, G. W.; Keal, T. W.; Sherwood, P.; Walsh, A.; Sokol, A. A. Band Alignment of Rutile and Anatase TiO_2. *Nature Materials* **2013**, *12* (9), 798–801. https://doi.org/10.1038/nmat3697.

(126) Legrini, O.; Oliveros, E.; Braun, A. M. Photochemical Processes for Water Treatment. *Chemical Reviews* **1993**, *93* (2), 671–698.

(127) Hofstadler, K.; Bauer, R.; Novalic, S.; Heisler, G. New Reactor Design for Photocatalytic Wastewater Treatment with TiO_2 Immobilized on Fused-Silica Glass Fibers: Photomineralization of 4-Chlorophenol https://pubs.acs.org/doi/pdf/10.1021/es00053a021 (accessed 2020 -12 -26). https://doi.org/10.1021/es00053a021.

(128) Athanasekou, C. P.; Romanos, G. E.; Katsaros, F. K.; Kordatos, K.; Likodimos, V.; Falaras, P. Very Efficient Composite Titania Membranes in Hybrid Ultrafiltration/Photocatalysis Water Treatment Processes. *Journal of Membrane Science* **2012**, *392–393*, 192–203. https://doi.org/10.1016/j.memsci.2011.12.028.

(129) Djafer, L.; Ayral, A.; Ouagued, A. Robust Synthesis and Performance of a Titania-Based Ultrafiltration Membrane with Photocatalytic Properties. *Separation and Purification Technology* **2010**, *75* (2), 198–203. https://doi.org/10.1016/j.seppur.2010.08.001.

(130) Romanos, G. Em.; Athanasekou, C. P.; Katsaros, F. K.; Kanellopoulos, N. K.; Dionysiou, D. D.; Likodimos, V.; Falaras, P. Double-Side Active TiO_2-Modified Nanofiltration Membranes in Continuous Flow Photocatalytic Reactors for Effective Water Purification. *Journal of Hazardous Materials* **2012**, *211–212*, 304–316. https://doi.org/10.1016/j.jhazmat.2011.09.081.

(131) Damodar, R. A.; You, S.-J.; Chou, H.-H. Study the Self Cleaning, Antibacterial and Photocatalytic Properties of TiO_2 Entrapped PVDF Membranes. *Journal of Hazardous Materials* **2009**, *172* (2), 1321–1328. https://doi.org/10.1016/j.jhazmat.2009.07.139.

(132) Bedford, N. M.; Pelaez, M.; Han, C.; Dionysiou, D. D.; Steckl, A. J. Photocatalytic Cellulosic Electrospun Fibers for the Degradation of Potent Cyanobacteria Toxin Microcystin-LR. *J. Mater. Chem.* **2012**, *22* (25), 12666–12674. https://doi.org/10.1039/C2JM31597A.

(133) Li, G.; Park, S.; Kang, D.-W.; Krajmalnik-Brown, R.; Rittmann, B. E. 2,4,5-Trichlorophenol Degradation Using a Novel TiO_2-Coated Biofilm Carrier: Roles of Adsorption, Photocatalysis, and Biodegradation. *Environ. Sci. Technol.* **2011**, *45* (19), 8359–8367. https://doi.org/10.1021/es2016523.

(134) Kalan, R. E.; Yaparatne, S.; Amirbahman, A.; Tripp, C. P. P25 Titanium Dioxide Coated Magnetic Particles: Preparation, Characterization and Photocatalytic Activity. *Applied Catalysis B: Environmental* **2016**, *187*, 249–258. https://doi.org/10.1016/j.apcatb.2016.01.008.

(135) Rachel, A.; Subrahmanyam, M.; Boule, P. Comparison of Photocatalytic Efficiencies of TiO_2 in Suspended and Immobilised Form for the Photocatalytic Degradation of Nitrobenzenesulfonic Acids. *Applied Catalysis B: Environmental* **2002**, *37* (4), 301–308. https://doi.org/10.1016/S0926-3373(02)00007-3.

(136) Byrne, J. A.; Eggins, B. R.; Brown, N. M. D.; McKinney, B.; Rouse, M. Immobilisation of TiO_2 Powder for the Treatment of Polluted Water. *Applied Catalysis B: Environmental* **1998**, *17* (1–2), 25–36. https://doi.org/10.1016/S0926-3373(97)00101-X.

(137) Verma, A.; Prakash, N. T.; Toor, A. P. An Efficient TiO_2 Coated Immobilized System for the Degradation Studies of Herbicide Isoproturon: Durability Studies. *Chemosphere* **2014**, *109*, 7–13. https://doi.org/10.1016/j.chemosphere.2014.02.051.

(138) El-Roz, M.; Haidar, Z.; Lakiss, L.; Toufaily, J.; Thibault-Starzyk, F. Immobilization of TiO_2 Nanoparticles on Natural Luffa Cylindrica Fibers for Photocatalytic Applications. *RSC Advances* **2013**, *3* (10), 3438. https://doi.org/10.1039/c2ra22438k.

(139) Fernandez, A.; Lassaletta, G.; Jimenez, V. M.; Justo, A.; Gonzalez-Elipe, A. R.; Herrmann, J.-M.; Tahiri, H.; Ait-Ichou, Y. Preparation and Characterization of TiO_2 Photocatalysts Supported on Various Rigid Supports (Glass, Quartz and Stainless Steel). Comparative Studies of Photocatalytic Activity in Water Purification. *Applied Catalysis B: Environmental* **1995**, *7* (1–2), 49–63.

(140) Pozzo, R. L.; Baltanás, M. A.; Cassano, A. E. Supported Titanium Oxide as Photocatalyst in Water Decontamination: State of the Art. *Catalysis Today* **1997**, *39* (3), 219–231. https://doi.org/10.1016/S0920-5861(97)00103-X.

(141) Peter, A.; Von Gunten, U. Oxidation Kinetics of Selected Taste and Odor Compounds During Ozonation of Drinking Water. *Environ. Sci. Technol.* **2007**, *41* (2), 626–631. https://doi.org/10.1021/es061687b.

(142) Liang, C.; Wang, D.; Chen, J.; Zhu, L.; Yang, M. Kinetics Analysis on the Ozonation of MIB and Geosmin. *Ozone: Science & Engineering* **2007**, *29* (3), 185–189. https://doi.org/10.1080/01919510701294197.

(143) Westerhoff, P.; Yoon, Y.; Snyder, S.; Wert, E. Fate of Endocrine-Disruptor, Pharmaceutical, and Personal Care Product Chemicals during Simulated Drinking Water Treatment Processes. *Environmental Science & Technology* **2005**, *39* (17), 6649–6663. https://doi.org/10.1021/es0484799.

(144) Huang, W.-J.; Cheng, Y.-L.; Cheng, B.-L. Effect of Water Quality on Destruction of Odor Causing Substances during Ozonation Processes. *J. Environ. Eng. Manage* **2007**, *17*, 257–265.

(145) Qi, F.; Xu, B.; Chen, Z.; Ma, J.; Sun, D.; Zhang, L. Efficiency and Products Investigations on the Ozonation of 2-Methylisoborneol in Drinking Water. *Water Environ Res* **2009**, *81* (12), 2411–2419. https://doi.org/10.2175/106143009x425933.

(146) Ho, L.; Newcombe, G.; Croué, J.-P. Influence of the Character of NOM on the Ozonation of MIB and Geosmin. *Water Research* **2002**, *36* (3), 511–518. https://doi.org/10.1016/S0043-1354(01)00253-6.

(147) Lawton, L. The Destruction of 2-Methylisoborneol and Geosmin Using Titanium Dioxide Photocatalysis. *Applied Catalysis B: Environmental* **2003**, *44* (1), 9–13. https://doi.org/10.1016/S0926-3373(03)00005-5.

(148) Tran, H.; Evans, G. M.; Yan, Y.; Nguyen, A. V. Photocatalytic Removal of Taste and Odour Compounds for Drinking Water Treatment. *Water Science and Technology: Water Supply* **2009**, *9* (5), 477–483.

(149) Bellu, E.; Lawton, L. A.; Robertson, P. K. J. Photocatalytic Destruction of Geosmin Using Novel Pelleted Titanium Dioxide. *Journal of Advanced Oxidation Technologies* **2008**, *11* (2). https://doi.org/10.1515/jaots-2008-0225.

(150) Bamuza-Pemu, E. E.; Chirwa, E. M. N. Photocatalytic Degradation of Taste and Odour Causing Compounds in Natural Water Sources. *1* **2011**, *23*, 387–392. https://doi.org/10.3303/CET1123065.

(151) Pettit, S. L.; Rodriguez-Gonzalez, L.; Michaels, J. T.; Alcantar, N. A.; Ergas, S. J.; Kuhn, J. N. Parameters Influencing the Photocatalytic Degradation of Geosmin and 2-Methylisoborneol Utilizing Immobilized TiO_2. *Catalysis Letters* **2014**, *144* (8), 1460–1465. https://doi.org/10.1007/s10562-014-1281-x.

(152) Federici, G.; Shaw, B. J.; Handy, R. D. Toxicity of Titanium Dioxide Nanoparticles to Rainbow Trout (Oncorhynchus Mykiss): Gill Injury, Oxidative Stress, and Other Physiological Effects. *Aquatic Toxicology* **2007**, *84* (4), 415–430. https://doi.org/10.1016/j.aquatox.2007.07.009.

(153) Pestana, C. J.; Robertson, P. K. J.; Edwards, C.; Wilhelm, W.; McKenzie, C.; Lawton, L. A. A Continuous Flow Packed Bed Photocatalytic Reactor for the Destruction of 2-Methylisoborneol and Geosmin Utilising Pelletised TiO_2. *Chemical Engineering Journal* **2014**, *235*, 293–298. https://doi.org/10.1016/j.cej.2013.09.041.

(154) Yaparatne, S.; Tripp, C. P.; Amirbahman, A. Photodegradation of Taste and Odor Compounds in Water in the Presence of Immobilized TiO_2 -SiO_2 Photocatalysts. *Journal of Hazardous Materials* **2018**, *346*, 208–217. https://doi.org/10.1016/j.jhazmat.2017.12.029.

(155) Sultana, S.; Amirbahman, A.; Tripp, C. P. A Method to Produce Robust Magnetic Particles Coated with TiO_2 Nano Particulates. *Applied Catalysis B: Environmental* **2020**, *273*, 118935. https://doi.org/10.1016/j.apcatb.2020.118935.

(156) Bamuza-Pemu, E.; Chirwa, E. Photocatalytic Degradation of Geosmin: Reaction Pathway Analysis. *Water SA* **2012**, *38* (5). https://doi.org/10.4314/wsa.v38i5.6.

(157) Robertson, P. K. J.; Bahnemann, D. W.; Lawton, L. A.; Bellu, E. A Study of the Kinetic Solvent Isotope Effect on the Destruction of Microcystin-LR and Geosmin

Using TiO_2 Photocatalysis. *Applied Catalysis B: Environmental* **2011**, *108–109*, 1–5. https://doi.org/10.1016/j.apcatb.2011.07.019.

(158) Pookmanee, P.; Ninsonti, H.; Sangsrichan, S.; Kangwansupamomkon, W.; Phanichphant, S. Photocatalytic Degradation of Geosmin by Titanium Dioxide Powder Synthesized by the Hydrothermal Route. *Advanced Materials Research* **2010**, *93–94*, 161–164. https://doi.org/10.4028/www.scientific.net/AMR.93-94.161.

(159) Yoon, S.-J.; Lee, Y. H.; Cho, W.-J.; Koh, I.-O.; Yoon, M. Synthesis of TiO_2-Entrapped EFAL-Removed Y-Zeolites: Novel Photocatalyst for Decomposition of 2-Methylisoborneol. *Catalysis Communications* **2007**, *8* (11), 1851–1856. https://doi.org/10.1016/j.catcom.2007.02.027.

(160) You, J.; Guo, Y.; Guo, R.; Liu, X. A Review of Visible Light-Active Photocatalysts for Water Disinfection: Features and Prospects. *Chemical Engineering Journal* **2019**, *373*, 624–641. https://doi.org/10.1016/j.cej.2019.05.071.

(161) Wang, H.; Zhang, L.; Chen, Z.; Hu, J.; Li, S.; Wang, Z.; Liu, J.; Wang, X. Semiconductor Heterojunction Photocatalysts: Design, Construction, and Photocatalytic Performances. *Chemical Society Reviews* **2014**, *43* (15), 5234–5244. https://doi.org/10.1039/C4CS00126E.

(162) Liqiang, J.; Yichun, Q.; Baiqi, W.; Shudan, L.; Baojiang, J.; Libin, Y.; Wei, F.; Honggang, F.; Jiazhong, S. Review of Photoluminescence Performance of Nano-Sized Semiconductor Materials and Its Relationships with Photocatalytic Activity. *Solar Energy Materials and Solar Cells* **2006**, *90* (12), 1773–1787. https://doi.org/10.1016/j.solmat.2005.11.007.

(163) Leyland, N. S.; Podporska-Carroll, J.; Browne, J.; Hinder, S. J.; Quilty, B.; Pillai, S. C. Highly Efficient F, Cu Doped TiO_2 Anti-Bacterial Visible Light Active Photocatalytic Coatings to Combat Hospital-Acquired Infections. *Scientific Reports* **2016**, *6* (1), 24770. https://doi.org/10.1038/srep24770.

(164) Marschall, R.; Wang, L. Non-Metal Doping of Transition Metal Oxides for Visible-Light Photocatalysis. *Catalysis Today* **2014**, *225*, 111–135. https://doi.org/10.1016/j.cattod.2013.10.088.

(165) Imtiaz, F.; Rashid, J.; Xu, M. Semiconductor Nanocomposites for Visible Light Photocatalysis of Water Pollutants. In *Concepts of Semiconductor Photocatalysis*; Rahman, M., Khan, A., Asiri, A., Inamuddin, I., Eds.; IntechOpen, **2019**. https://doi.org/10.5772/intechopen.86542.

(166) Irie, H.; Watanabe, Y.; Hashimoto, K. Nitrogen-Concentration Dependence on Photocatalytic Activity of $TiO_{2-x}N_x$ Powders. *The Journal of Physical Chemistry B* **2003**, *107* (23), 5483–5486. https://doi.org/10.1021/jp030133h.

(167) Di Valentin, C.; Pacchioni, G.; Selloni, A. Origin of the Different Photoactivity of N -Doped Anatase and Rutile TiO_2. *Physical Review B* **2004**, *70* (8). https://doi.org/10.1103/PhysRevB.70.085116.

(168) Di Valentin, C.; Pacchioni, G. Trends in Non-Metal Doping of Anatase TiO_2: B, C, N and F. *Catalysis Today* **2013**, *206*, 12–18. https://doi.org/10.1016/j.cattod.2011.11.030.

(169) Pelaez, M.; Nolan, N. T.; Pillai, S. C.; Seery, M. K.; Falaras, P.; Kontos, A. G.; Dunlop, P. S. M.; Hamilton, J. W. J.; Byrne, J. A.; O'Shea, K.; Entezari, M. H.; Dionysiou, D. D. A Review on the Visible Light Active Titanium Dioxide Photocatalysts for Environmental Applications. *Applied Catalysis B: Environmental* **2012**, *125*, 331–349. https://doi.org/10.1016/j.apcatb.2012.05.036.

(170) and, X. Z. L.; Li, F. B. Study of Au/Au_3+-TiO_2 Photocatalysts toward Visible Photooxidation for Water and Wastewater Treatment http://pubs.acs.org/doi/abs/10.1021/es001752w (accessed 2021 -01 -06). https://doi.org/10.1021/es001752w.

(171) Behar, D.; Rabani, J. Kinetics of Hydrogen Production upon Reduction of Aqueous TiO_2 Nanoparticles Catalyzed by Pd^0, Pt^0, or Au^0 Coatings and an Unusual Hydrogen Abstraction; Steady State and Pulse Radiolysis Study. *The Journal of Physical Chemistry B* **2006**, *110* (17), 8750–8755. https://doi.org/10.1021/jp060971m.

(172) Wang, W.; Zhang, J.; Chen, F.; He, D.; Anpo, M. Preparation and Photocatalytic Properties of Fe3+-Doped Ag@TiO_2 Core–Shell Nanoparticles. *Journal of Colloid and Interface Science* **2008**, *323* (1), 182–186. https://doi.org/10.1016/j.jcis.2008.03.043.

(173) Zeng, Y.; Wu, W.; Lee, S.; Gao, J. Photocatalytic Performance of Plasma Sprayed Pt-Modified TiO_2 Coatings under Visible Light Irradiation. *Catalysis Communications* **2007**, *8* (6), 906–912. https://doi.org/10.1016/j.catcom.2006.09.023.

(174) You, X.; Chen, F.; Zhang, J.; Anpo, M. A Novel Deposition Precipitation Method for Preparation of Ag-Loaded Titanium Dioxide. *Catal Lett* **2005**, *102* (3), 247–250. https://doi.org/10.1007/s10562-005-5863-5.

(175) Han, Q. Advances in Preparation Methods of Bismuth-Based Photocatalysts. *Chemical Engineering Journal* **2020**, 127877. https://doi.org/10.1016/j.cej.2020.127877.

(176) Meng, X.; Zhang, Z. Bismuth-Based Photocatalytic Semiconductors: Introduction, Challenges and Possible Approaches. *Journal of Molecular Catalysis A: Chemical* **2016**, *423*, 533–549. https://doi.org/10.1016/j.molcata.2016.07.030.

(177) An, H.; Du, Y.; Wang, T.; Wang, C.; Hao, W.; Zhang, J. Photocatalytic Properties of BiOX (X = Cl, Br, and I). *Rare Metals* **2008**, *27* (3), 243–250. https://doi.org/10.1016/S1001-0521(08)60123-0.

(178) Meng, X.; Zhang, Z. Facile Synthesis of BiOBr/Bi2WO6 Heterojunction Semiconductors with High Visible-Light-Driven Photocatalytic Activity. *Journal of Photochemistry and Photobiology A: Chemistry* **2015**, *310*, 33–44. https://doi.org/10.1016/j.jphotochem.2015.04.024.

(179) Drache, M.; Roussel, P.; Wignacourt, J.-P. Structures and Oxide Mobility in Bi−Ln−O Materials: Heritage of Bi_2O_3. *Chemical Reviews* **2007**, *107* (1), 80–96. https://doi.org/10.1021/cr050977s.

(180) Sood, S.; Umar, A.; Kumar Mehta, S.; Kumar Kansal, S. α-Bi_2O_3 Nanorods: An Efficient Sunlight Active Photocatalyst for Degradation of Rhodamine B and 2,4,6-Trichlorophenol. *Ceramics International* **2015**, *41* (3, Part A), 3355–3364. https://doi.org/10.1016/j.ceramint.2014.10.038.

(181) Reverberi, A. P.; Varbanov, P. S.; Vocciante, M.; Fabiano, B. Bismuth Oxide-Related Photocatalysts in Green Nanotechnology: A Critical Analysis. *Frontiers of Chemical Science and Engineering* **2018**, *12* (4), 878–892. https://doi.org/10.1007/s11705-018-1744-5.

(182) Hameed, A.; Gombac, V.; Montini, T.; Felisari, L.; Fornasiero, P. Photocatalytic Activity of Zinc Modified Bi_2O_3. *Chemical Physics Letters* **2009**, *483* (4), 254–261. https://doi.org/10.1016/j.cplett.2009.10.087.

(183) Fang, D.; Qin, Z.; Qufu, W.; Dongjian, S.; Mingqing, C. Control of Photocatalytic Property of Bismuth-Based Semiconductor Photocatalysts. *Progress in Chemistry* **2014**, *26* (01), 30. https://doi.org/10.7536/PC130770.

(184) Correia, F. C.; Calheiros, M.; Marques, J.; Ribeiro, J. M.; Tavares, C. J. Synthesis of Bi_2O_3/TiO_2 Nanostructured Films for Photocatalytic Applications. *Ceramics International* **2018**, *44* (18), 22638–22644. https://doi.org/10.1016/j.ceramint.2018.09.040.

(185) Wang, C.; Tan, C.; Lv, W.; Zhu, G.; Wei, Z.; Zhang, K. H. L.; He, W. Coherent Bi_2O_3-TiO_2 Hetero-Junction Material through Oriented Growth as an Efficient Photo-Catalyst for Methyl Orange Degradation. *Materials Today Chemistry* **2018**, *8*, 36–41. https://doi.org/10.1016/j.mtchem.2018.02.005.

(186) Chakraborty, A. K.; Hossain, M. E.; Rhaman, M. M.; Sobahan, K. Fabrication of Bi_2O_3/TiO_2 Nanocomposites and Their Applications to the Degradation of Pollutants in Air and Water under Visible-Light. *Journal of Environmental Sciences* **2014**, *26* (2), 458–465. https://doi.org/10.1016/S1001-0742(13)60428-3.

(187) Zhang, H.; Lü, M.; Liu, S.; Xiu, Z.; Zhou, G.; Zhou, Y.; Qiu, Z.; Zhang, A.; Ma, Q. Preparation and Photocatalytic Properties of Sillenite $Bi_{12}TiO_{20}$ Films. *Surface and Coatings Technology* **2008**, *202* (20), 4930–4934. https://doi.org/10.1016/j.surfcoat.2008.04.081.

(188) Lin, X.; Lv, P.; Guan, Q.; Li, H.; Zhai, H.; Liu, C. Bismuth Titanate Microspheres: Directed Synthesis and Their Visible Light Photocatalytic Activity. *Applied Surface Science* **2012**, *258* (18), 7146–7153. https://doi.org/10.1016/j.apsusc.2012.04.019.

(189) Kumar, M. K.; Bhavani, K.; Srinivas, B.; Kumar, S. N.; Sudhakar, M.; Naresh, G.; Venugopal, A. Nano Structured Bismuth and Nitrogen Co-Doped TiO_2 as an Efficient Light Harvesting Photocatalyst under Natural Sunlight for the Production of H_2 by H_2O Splitting. *Applied Catalysis A: General* **2016**, *515*, 91–100. https://doi.org/10.1016/j.apcata.2016.01.009.

(190) Vela, N.; Calín, M.; Yáñez-Gascón, M. J.; Garrido, I.; Pérez-Lucas, G.; Fenoll, J.; Navarro, S. Photocatalytic Oxidation of Six Pesticides Listed as Endocrine Disruptor Chemicals from Wastewater Using Two Different TiO_2 Samples at Pilot Plant Scale under Sunlight Irradiation. *Journal of Photochemistry and Photobiology A: Chemistry* **2018**, *353*, 271–278. https://doi.org/10.1016/j.jphotochem.2017.11.040.

(191) Azami, M. S.; Ain, S. K.; Zaharudin, R.; Bakar, F.; Nawawi, W. I. Immobilized/P25/DSAT and Immobilized/Kronos/DSAT on Photocatalytic Degradation of Reactive Red 4 Under Fluorescent Light. *MATEC Web of Conferences* **2016**, *47*, 05015. https://doi.org/10.1051/matecconf/20164705015.

(192) Fotiou, T.; Triantis, T. M.; Kaloudis, T.; O'Shea, K. E.; Dionysiou, D. D.; Hiskia, A. Assessment of the Roles of Reactive Oxygen Species in the UV and Visible Light Photocatalytic Degradation of Cyanotoxins and Water Taste and Odor Compounds Using C–TiO_2. *Water Research* **2016**, *90*, 52–61. https://doi.org/10.1016/j.watres.2015.12.006.

(193) Fotiou, T.; Triantis, T. M.; Kaloudis, T.; Pastrana-Martínez, L. M.; Likodimos, V.; Falaras, P.; Silva, A. M. T.; Hiskia, A. Photocatalytic Degradation of Microcystin-LR and Off-Odor Compounds in Water under UV-A and Solar Light with a Nanostructured Photocatalyst Based on Reduced Graphene Oxide–TiO_2 Composite. Identification of Intermediate Products. *Industrial & Engineering Chemistry Research* **2013**, *52* (39), 13991–14000. https://doi.org/10.1021/ie400382r.

(194) Pastrana-Martínez, L. M.; Morales-Torres, S.; Likodimos, V.; Figueiredo, J. L.; Faria, J. L.; Falaras, P.; Silva, A. M. T. Advanced Nanostructured Photocatalysts Based on Reduced Graphene Oxide–TiO_2 Composites for Degradation of Diphenhydramine Pharmaceutical and Methyl Orange Dye. *Applied Catalysis B: Environmental* **2012**, *123–124*, 241–256. https://doi.org/10.1016/j.apcatb.2012.04.045.

CHAPTER 2 : PHOTODEGRADATION OF TASTE AND ODOR COMPOUNDS IN WATER IN THE PRESENCE OF IMMOBILIZED TiO_2-SiO_2 PHOTOCATALYSTS

2.1. Abstract

Disinfection by ultraviolet (UV) radiation is a growing trend in public water treatment systems because of its effectiveness with respect to the inactivation of protozoa and other pathogenic microorganisms. However, removal of different classes of organic compounds, including taste and odor compounds, in water is not effective with UV irradiation. In this chapter, we report a novel TiO_2-based immobilized photocatalyst that was developed to enhance the UV photodegradation of two of the major taste and odor compounds, 2-methylisoborneol (MIB) and Geosmin (GSM) in water. Evonik (formerly Degussa) P-25 powder-modified TiO_2 was immobilized on glass slides using TiO_2-SiO_2 sol-gel mixture as the binder and calcined at 500°C. Several catalyst films with different Si amounts were synthesized and characterized by X-ray diffraction (XRD), X-ray photoelectron spectroscopy (XPS), infrared spectroscopy (IR), diffuse reflectance spectroscopy (DRS), photoluminescence spectroscopy (PL), and scanning electron microscopy (SEM). Photocatalytic degradation of MIB and GSM was investigated by irradiating aqueous solutions under UV-A light (350 nm). The generation of hydroxyl radicals (•OH) was also assessed to evaluate the activity of the photocatalyst films. Catalyst films with surface ratios of Ti:Si ≈ 7 showed similar degradation rates but better robustness compared to immobilized P25 films.

2.2. Introduction

Access to safe drinking water is a basic necessity for maintaining human health. According to the US EPA, there are five major types of contaminants in drinking water: microorganisms, disinfection byproducts, inorganic chemicals, organic chemicals, and radionuclides[1]. In 2006, EPA introduced the long-term 2 enhanced surface water treatment rule (LT2) to further reduce contamination by pathogens in drinking water, specifically viruses and the protozoa, *Cryptosporidium and Giardia*[2]. In compliance with LT2, UV disinfection, as an effective means for inactivating these pathogenic microorganisms, has gained more interest in public water treatment systems. However, direct UV photolysis is not very effective with respect to the degradation of many organic compounds, such as taste and odor compounds in water[3,4].

The changing climate, especially the increasing average temperatures, has led to surface water quality deterioration in many temperate regions. Many lakes in these areas have experienced increased turbidity and algal blooms, including harmful algae[5]. The growth of cyanobacteria and actinomycetes is promoted due to eutrophication caused by the disposal of agricultural, municipal, and industrial wastes into water bodies, as well as internal phosphorus release[6,7]. Higher temperatures and longer periods of higher temperatures result in more widespread lake hypolimnetic anoxia[8] that can lead to the release of sediment phosphorus, causing undesired algal blooms[9]. Taste and odor compounds are mainly produced by cyanobacterial blooms as secondary metabolites[10]. The odor threshold of these compounds is in the ng L^{-1} range, making their effective removal from drinking water a challenging task. Previous studies have shown that most of the taste and odor compounds

are resistant to conventional water treatment techniques, such as coagulation, sedimentation, and filtration, especially at very low concentration[11].

Only a few conventional water treatment methods have been successful in removing taste and odor compounds at such low concentrations. Oxidants such as Cl_2, ClO_2, and $KMnO_4$ have proven to be ineffective in degrading these compounds due to the resistance of tertiary alcohols toward mild oxidation[11]. Filtration using granular activated carbon and sand and alum coagulation are used for the removal of taste and odor compounds in some water treatment facilities[12,13]. In the presence of dissolved organic matter (DOM), reduced adsorption of these compounds has been observed, where additional steps are taken to clean the saturated activated carbon for reuse[14]. Two common taste and odor compounds found in surface waters are 2-methylisoborneol (MIB; odor threshold 15 ng L^{-1}) and geosmin (GSM; odor threshold 4 ng L^{-1})[15]. MIB is a terpenoid produced by the cyanobacterial species, *Oscillatoria and Phormidium*, and actinomycetes[16–18]. GSM is a bicyclic tertiary alcohol produced by certain species of *Oscillatoria*, *Anabaena*, *Lyngbya*, *Symploca,* and actinomycetes[17,18].

Advanced oxidation processes (AOPs) have the advantage of providing fast reaction rates and strong non-selective oxidation over multiple contaminants. As such, they have become desirable techniques for degrading taste and odor compounds[19,20]. UV irradiation in the presence of colloidal TiO_2-based photocatalysts is one of the AOPs that can efficiently degrade MIB and GSM via the production of hydroxyl radicals ($^{\bullet}OH$)[21]. However, the use of a photocatalyst suspension in a UV water treatment reactor is limited due to difficulties in the separation of the suspended photocatalyst particles following treatment. Therefore,

it is important to have an immobilized photocatalytic system to enhance the UV degradation of organic compounds in water[22–26].

Among different TiO_2 photocatalysts, P25 is considered as the "gold standard" due to its efficiency compared to other forms of TiO_2[27,28]. P25 consists of 70% anatase phase and 30% rutile phase and has a surface area of 49 m^2 g^{-1} [29,30]. Owing to its high surface area and the coexistence of rutile -anatase phases which allows the increase in charge-separation efficiency due to interfacial electron transfer, P25 shows a high activity in degrading organic pollutants[30–33].

Immobilizing P25 alone onto substrates does not result in a robust and durable film with sufficient mechanical stability. To improve the robustness of the coatings and improve the adherence of P25, Ti alkoxide and SiO_2 gel-supported matrices can be used[34–38]. The presence of SiO_2 in the catalyst films improves their thermal stability and mechanical strength[39,40]. Even though SiO_2 is added as a binder, in these studies, its effect on photocatalytic activity has not been assessed. Further, the effect of these binary oxides on the degradation rate of taste and odor compounds has not been studied. To date, most of the MIB and GSM photodegradation studies have been performed in TiO_2 slurry systems[25,26]. To the best of our knowledge, very few studies were carried out on the degradation of MIB and GSM using immobilized TiO_2 catalysts[25,26]. In these studies, TiO_2 nanoparticles dispersed in methanol have been directly coated on glass substrates. The robustness of such coatings is poor, where the coating exfoliates even under gentle rubbing, according to our observations.

The objective of this study is to develop an effective TiO_2-based photocatalyst, using P25 modified TiO_2-SiO_2 sol-gel, immobilized on a glass substrate to augment the existing UV

systems for degradation of taste and odor compounds. Photocatalytic degradation rates of MIB and GSM were measured in the presence of catalyst films with varying concentrations of SiO_2 under monochromatic UV-A light (350 nm). Development of TiO_2 photocatalysts following the sol-gel method with a controlled hydrolysis and condensation reactions resulted in photocatalysts with enhanced structural and catalytic properties.

2.3. Experimental

2.3.1. Preparation of powder modified TiO_2-SiO_2 immobilized catalyst

Titanium tetraisoprpoxide and (TTIP, 99.99%; Sigma Aldrich) and tetraethylorthosilicate (TEOS, 99.99%; Sigma Aldrich) were used as precursors for TiO_2 and SiO_2, respectively. P25 TiO_2 powder (Evonik, formerly Degussa) was used to prepare sol-gel derived powder-immobilized coatings. The TiO_2 sol-gel mixture was prepared according to a previously reported method[23]. First, polyoxyethylene (20) sorbitan monooleate (Tween 80, 99.99%; Sigma Aldrich) was homogeneously dissolved in 2-propanol (iPrOH, 99.99%; Sigma Aldrich). Then acetic acid (AcOH, 99.7%; EM Science) was dissolved into the solution, and TTIP was added under stirring. The molar ratios of the reactants were Tween 80: iPrOH:AcOH: TTIP = 1:45:6:1. The final transparent TiO_2 sol was stirred for 30 min before mixing it with the SiO_2 sol, which was prepared by adding TEOS to a solution of pure ethanol (EtOH) and concentrated HCl and stirring for 30 min. Molar ratios of the SiO_2 sol mixture were TEOS:EtOH: HCl = 1:8:0.05. Different volumes (1.3–8.5 mL) of SiO_2 sol (1.43 M) were added to 66.6 mL of TiO_2 sol (0.18 M) to obtain different Si molar concentrations and stirred for 60 min. P25 TiO_2 powder (50 g L^{-1}) was added to the TiO_2-SiO_2 solution and stirred for 6 h. The final Si: Ti molar ratios were 3, 5, 10, 15, and 20%.

As controls, catalyst films with TiO_2 sol, TiO_2-SiO_2 sol, powder-modified (with added P25) and TiO_2-SiO_2 sol, and P25 (dispersed in iPrOH) were synthesized.

Plain microscope glass slides were cleaned with piranha solution (H_2SO_4:H_2O_2 = 7:3 v/v) for 1 h at 70 ˚C, washed with deionized water, and dried at 125 ˚C in an oven. Cleaned glass slides were dip-coated with control films and P25 powder modified TiO_2-SiO_2 sol-gel mixtures (10 cm^2 area on each side & four coatings). Dip coating was performed at a withdrawal rate of 120 mm min^{-1}. Catalyst coatings were dried and annealed at 125 ˚C for 24 h followed by calcination at a ramp rate of 3 ˚C min^{-1} up to 500 ˚C, dwelling at this temperature for 1h and cooling down naturally. The labeling scheme for the photocatalysts is shown in Table 2.1.

Table 2.1. Photocatalyst films developed in this study

Catalyst	**P25 (g L^{-1})**	**Si: Ti molar ratio in the initial sol-gel**
T (Ti sol gel only)	0	0:100
ST (Si-Ti sol gel))	0	15:85
P (P25 only)	50	0:100
PT (P25 & Ti sol gel)	50	0:100
PS3T (P25 & Si **(**3%)-Ti sol gel)	50	3:97
PS5T	50	5:95
PS10T	50	10:90
PS15T	50	15:85
PS20T	50	20:80

2.3.2. Photocatalytic degradation of MIB and GSM

Photodegradation experiments were conducted in 200 mL quartz beakers in the presence of MIB (≥98.0%; Sigma Aldrich) or GSM (≥97.0%; Sigma Aldrich) at a concentration of 500 ng L^{-1} in deionized water (DI, 18 MΩ cm). Coated glass slides (4 slides) were immersed vertically (Figure 2.1) in the beakers covered with aluminum foil, and the system was allowed to equilibrate for 20 min in the dark. The solutions were then placed in a photochemical chamber (Rayonet Model RPR-100) and illuminated with 16 lamps (Rayonet RPR- 3500 Å), each emitting monochromatic light in the UV-A range (~350 nm) for 60 min under stirring. During the irradiation, 10 mL aliquots of solution were taken out at six different time intervals (0, 5, 10, 15, 30, and 60 min) for analysis of MIB and GSM concentrations. The degradation experiments were repeated three times using the same set of films of each catalyst. The intensity of the UV lamps was measured by the ferrioxalate actinometry method[41]. Potassium ferrioxalate was used as the chemical actinometer, and the dissolved Fe(II) concentration was measured using the ferrozine method[42].

2.3.3. Analytical determination of MIB and GSM

The concentrations of MIB and GSM were determined by headspace solid-phase microextraction (HS-SPME) gas chromatography-mass spectrometry (GC–MS; Agilent 6890 Series gas chromatograph interfaced to an Agilent 5973 mass selective detector). Samples (10 mL) were placed in screw-capped, straight-sided headspace vials with PTFE-lined silicone septa. NaCl (3.0 g) and a magnetic stirrer were added to the sealed vials and placed in a 70 ˚C water bath for 20 min[43]. A GC temperature gradient from 50 ˚C (held for 1 min) to 250 ˚C (held for 6 min), using a temperature ramp of 12˚C min^{-1} under constant flow of He gas at 1 mL $min^{-1,}$ was used. Extraction of analytes by HS-SPME was achieved using a Supelco fiber coated with Divinyl-benzene/Carboxen/Polydimethylsiloxane (DVB/CAR/PDMS), Stableflex, 50/30 µm. Detection was performed in selected ion monitoring (SIM) mode at m/z = 95 for MIB, and m/z = 112 for GSM. Data processing and instrument control were performed using the Agilent MSD Chemstation software.

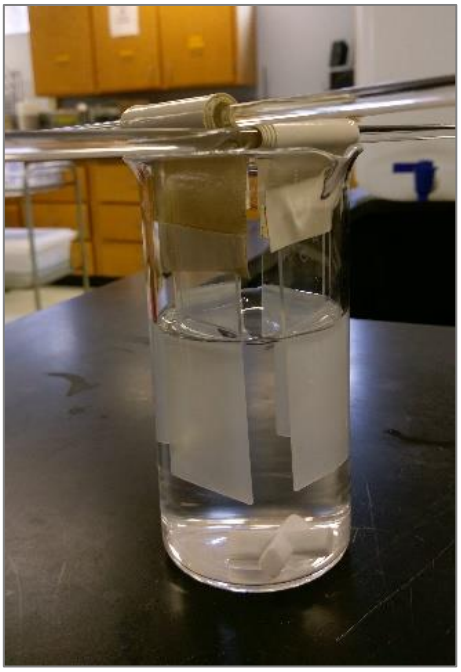

Figure 2.1. Photocatalytic degradation experiment setup; Catalyst coated glass slides immersed in quartz beaker

2.3.4. Reusability and radical hydroxyl production assessment and stability of the catalyst

Reusability of the most efficient and robust catalyst film (PS3T) was evaluated by •OH production using terephthalic acid (TPA, 98%; Sigma Aldrich) for 10 repetitions. The reaction product of TPA with •OH is 2-hydroxyterephthalic acid (hTPA), whose fluorescence intensity is proportional to the •OH concentration[44–46]. Coated glass slides were immersed in 200 mL of 0.5 mM TPA solution at pH 8 and equilibrated in the dark for 15 min. The TPA solution with the catalyst films were placed in the photochemical chamber and irradiated for 60 min while stirring (UV-A at 350 nm with 16 lamps). At specified time intervals during illumination, 3 mL aliquots were withdrawn and diluted with DI water for fluorescence measurements of hTPA at excitation and emission wavelengths of 315 and 425 nm, respectively. Generated hTPA concentrations were calculated using a hTPA calibration curve (hTPA, 97%; Sigma Aldrich). Indirect photodegradation by the PS3T catalyst was assessed by calculating the steady-state •OH concentration[39,44,47]. The fluorescence spectra were recorded on a Jobin Yvon Fluorolog-3 spectrofluorometer equipped with emission and excitation monochromators, a 400 W Xenon lamp source, and a photomultiplier tube. Control experiments were carried out to evaluate the generation of •OH under dark conditions and UV only illumination.

2.3.5. Catalyst characterization

X-ray diffraction (XRD) patterns of catalyst films were obtained on a PANanalytical X'pert MRD X-ray diffraction system using Cu-Ka radiation at a scan rate of $0.3^{\circ}\ s^{-1}$. X-ray photoelectron spectroscopy (XPS) was performed on a dual anode VG Microtech X-ray source and a SPECS HSA2000 analyzer (Source: Al, Source energy: 1486.61 eV). FTIR

spectra of the catalyst films were recorded on the powder obtained from scraping off the catalyst from the glass slide. Transmission FTIR spectra were recorded on an ABB FTLA2000 spectrometer. Diffuse reflectance spectra were collected on solid samples at 25 °C. The light source was a Mikropack DH-2000 deuterium and halogen light source coupled with an Ocean Optics USB4000 detector. The scattered light was collected with a fiber optic cable. Spectra were referenced with PTFE. Data were processed using Spectra Suite 1.4.2 09. The elemental composition of each type of photocatalyst film was obtained by digesting the coated glass slides in a solution containing 20 mL of 3:1 mixture (volume ratio) of concentrated H_2SO_4 (ACS reagent, 95-98%) and H_2O_2 (Certified ACS, 30% w/v), and analyzing using an Inductively Coupled Plasma-Atomic Emission Spectrometer (ICP-AES; TJA Model iCAP 6000). Steady-state photoluminescence (PL) spectra were recorded with a Model QuantaMaster-1046 photoluminescence spectrophotometer (Photon Technology International). The instrument is equipped with two excitation monochromators and a single emission monochromator with a 75 W Xenon arc lamp. The excitation wavelength was at 325 nm. Scanning electron microscopy (SEM) was performed on a Zeiss N vision 40 system. The adherence ability of the catalyst films was evaluated by the cross-cut tape adhesion test (ASTM D3359)[48].

2.3.6. Photoleaching experiments

To quantify the concentrations of Ti and Si leaching from the catalyst films during the experiments, 10 mL aliquots of the sample were withdrawn at the end of TPA experiments (60 min) and were analyzed using an Inductively Coupled Plasma Atomic Emission Spectrometer (ICP-AES; TJA Model iCAP 6000). A TPA solution irradiated for 60 min was used as a blank sample without the catalyst film.

2.4. Results and discussion

2.4.1. Photocatalytic degradation of MIB and GSM

Figures 2.2-2.5 show the photodegradation of MIB and GSM in the presence and absence of the catalyst films. Three trials of degradation experiments were performed using the same set of glass slides for each catalyst type, and an average degradation was taken. MIB adsorption to TiO_2 surface is negligible relative to the total amount in solution[25]. During a period of 1h, MIB concentration decreased by ~20% under the dark condition in the absence of a catalyst (Figure 2.2) that can be attributed to its volatilization.

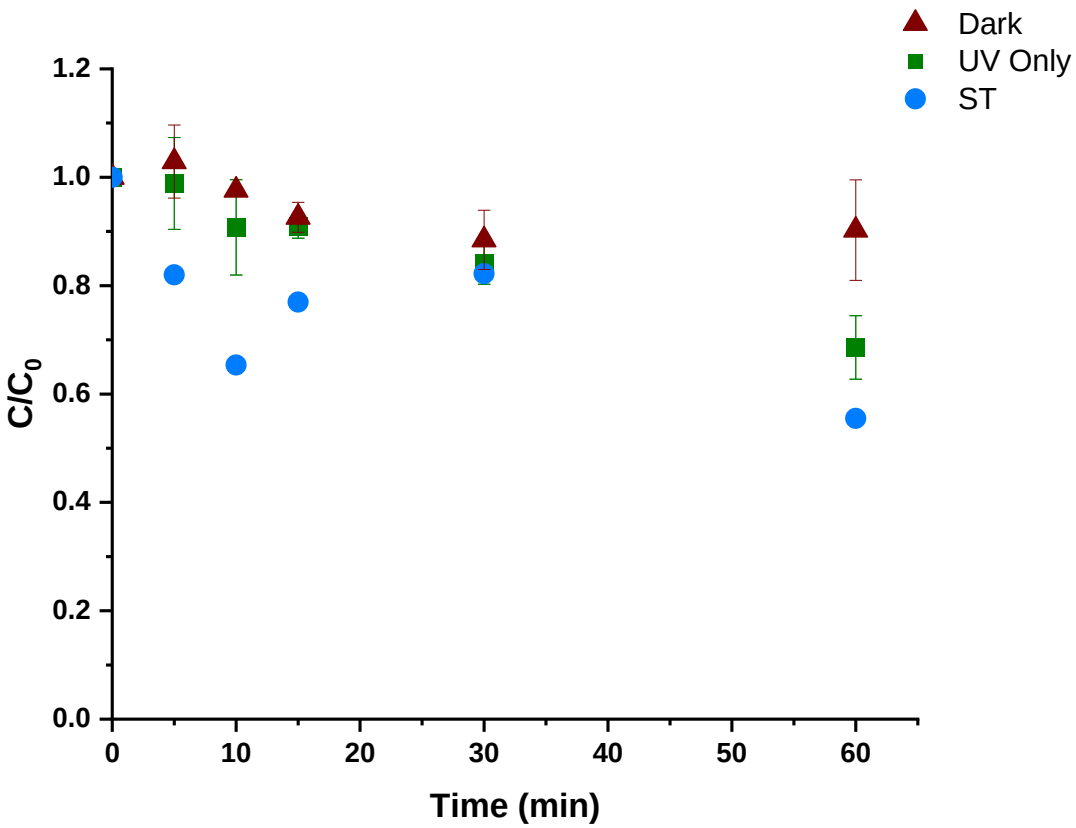

Figure 2.2. Time concentration plots for the photodegradation of MIB (500 ng L^{-1} initial concentration) for (▲) dark control, (■) UV (350 nm) only, (●) ST photocatalyst

For the same duration, a ~30% decrease in MIB concentration was observed in the presence of UV light only that can be attributed to a combination of about 10% photolytic degradation and 20% volatilization. A previous photolytic degradation study of MIB and GSM showed that ~10% of MIB and ~7% of GSM were degraded by UV alone at 365 nm, emitting 71.7 mW cm^{-2} at a distance of 25 cm in 60 min[49]. In our experiment, the ferrioxlate actinometry measurement showed a UV intensity of 18.3 mW cm^{-2} (corresponding to $5.1x10^{-4}$ Einstein min^{-1}) at a distance of 12.5 cm to the center of the quartz beaker. UV intensity drops off as a square of the distance between the source and the sample[50]. Considering these distances, the samples in Fotiou et al.'s study[49] and our study are exposed to a similar UV intensity of 0.1 mW cm^{-2}. The presence of the catalyst film in our study resulted in an increase in the MIB degradation rate (Figure 2.3).

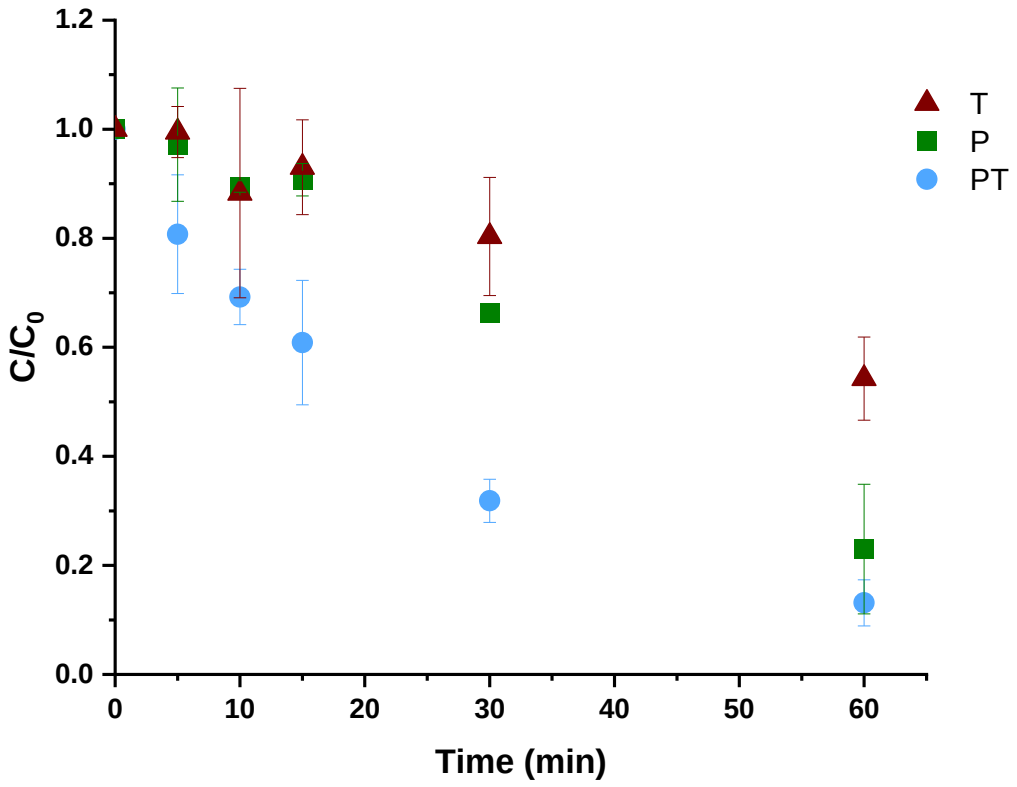

Figure 2.3. Time concentration plots for the photodegradation of MIB (500 ng L^{-1} initial concentration) for (▲)T, (■) P, and (●) PT photocatalysts

Catalyst films T (coated with only the TiO_2 sol gel) and ST (coated with TiO_2-SiO_2 sol gel) resulted in ~50% MIB loss after 1h. Catalyst coatings P (immobilized P25) and PT (immobilized P25 and TiO_2 sol gel) showed ~80% concentration loss of MIB during the same period. MIB photodegradation in the presence of SiO_2-containing catalyst films is shown in Figure 2.4.

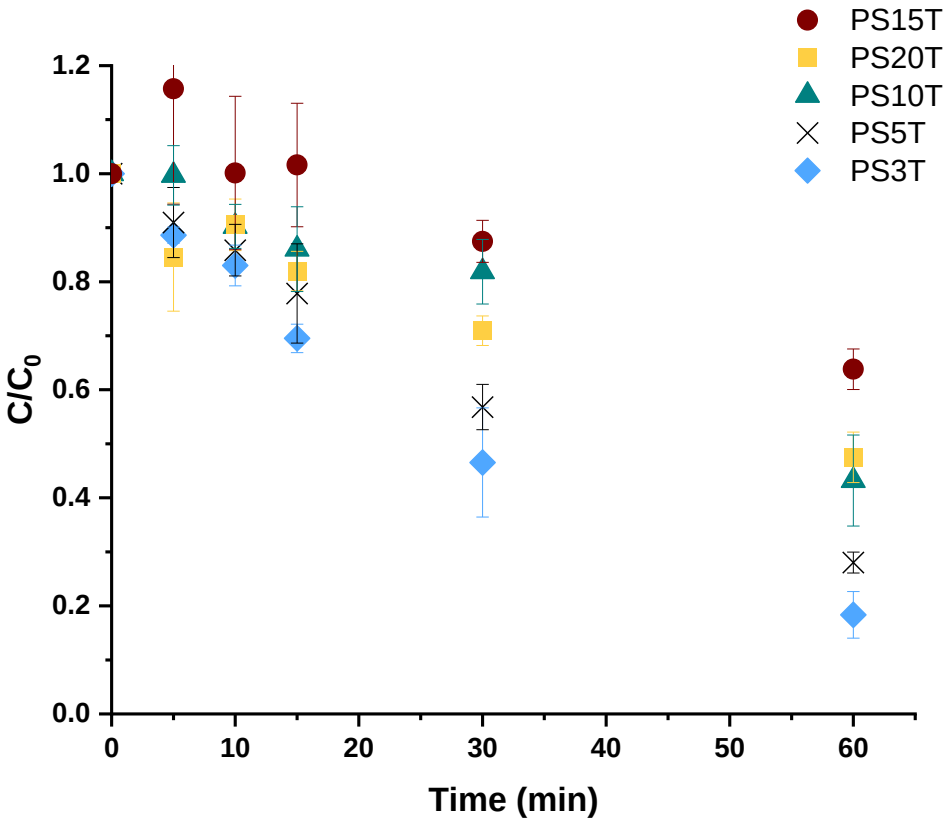

Figure 2.4. Time concentration plots for the photodegradation of MIB (500 ng L^{-1} initial concentration) for (●) PS15T, (■)PS20T, (▲) PS10T, (×) PS5T, (◆) PS3T

When the SiO_2 content was increased from 3% to 20% in the sol-gel, the photodegradation rate decreased from ~80% to ~50%. Catalyst films synthesized from sol-gel mixtures containing 3% Si (PS3T) showed ~80% loss of MIB within 1h, which is comparable to that performance of the P and PT catalysts. The presence of the PS3T catalyst also resulted in ~80% GSM photodegradation in 1h (Figure 2.5).

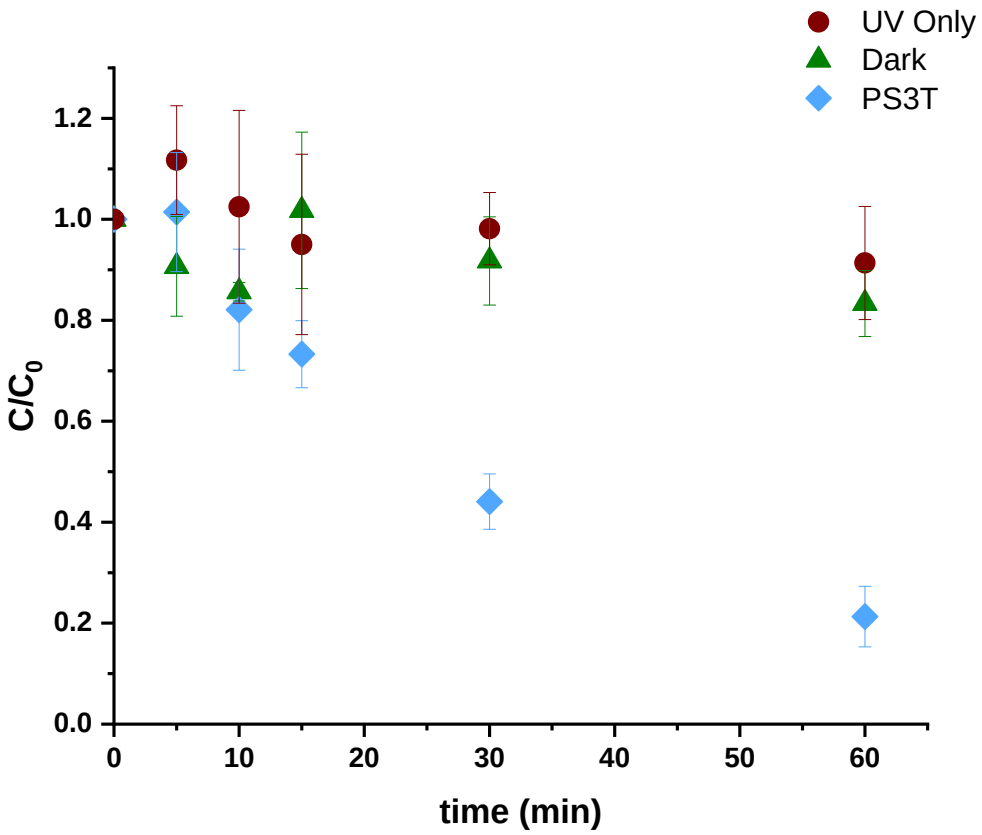

Figure 2.5. Time concentration plots for the photodegradation of Geosmin (500 ng L^{-1} initial concentration for(●) UV (350 nm) only, (▲) dark control, (◆) PS3T catalyst

The higher effectiveness of the P and PT photocatalysts compared to the T and ST catalysts can be attributed to the presence of P25[31]. The decrease in photocatalytic activity of the films when increasing the SiO_2 content is due to the smaller concentration of TiO_2 (dilution of TiO_2 phase in SiO_2)[51–53] on the substrate surface as observed in XPS,

which is discussed below. The degradation kinetics of both compounds followed pseudo-first-order kinetics, which agrees with previously reported TiO_2 photodegradation studies of organic compounds[54–57]. Apparent rate constants (k_{app}) under dark conditions, at UV-only treatment and in the presence of T, P, PT, and PS3T catalysts are shown in the Table 2.2. k_{app} values for MIB and GSM degradation in the presence of PS3T (The total Ti content 0.4 mg cm^{-2}) catalyst were 2.9 x 10^{-2} and 2.7 x 10^{-2} min^{-1}, respectively. A previous study of photocatalytic removal of MIB and GSM by immobilized P25 (0.25 mg cm^{-2}) onto borosilicate glass plates showed 54% and 60% removal, respectively, over an 8h period under UV A light[26]. Another study of immobilized P25 (0.5 mg cm^{-2}; ~0.3 mg- Ti cm^{-2}) on petri dish showed ~80% degradation in 1h of both MIB (k_{app} = 2.7 x 10^{-2} min^{-1}) and GSM (k_{app} = 2.4 x 10^{-2} min^{-1}) at 365 nm with 1.48x10^{-4} Einstein min^{-1} intensity[25]. These k_{app} values are comparable to ours according to the amount of catalyst and UV intensity (Table 2.2).

Table 2.2. Apparent rate constants (k_{app}) for photocatalytic degradation of MIB and GSM at 350 nm

Catalyst	**k_{app} (min^{-1}) MIB**	**k_{app} (min^{-1}) GSM**
Dark	5.1×10^{-3}	2.1×10^{-3}
UV only	6.2×10^{-3}	2.2×10^{-3}
T	1.0×10^{-2}	N/A
P	2.5×10^{-2}	N/A
PT	3.2×10^{-2}	N/A
PS3T	2.9×10^{-2}	2.72×10^{-2}
PS5T	2.1×10^{-2}	N/A
PS10T	1.4×10^{-2}	N/A
PS15T	8.8×10^{-3}	N/A
PS20T	1.2×10^{-2}	N/A

2.4.2. Reusability of the catalyst films

Figure 2.6 shows the production of hTPA in the presence of PS3T catalyst for 10 repetitions. Produced hTPA concentrations after 60 min were in the range of $6.1x10^{-6}$ M–$9.3x10^{-6}$ M with no significant trend in hTPA concentrations, suggesting that the photocatalyst activity with respect to the production of $^{\bullet}OH$ does not change with repeated use.

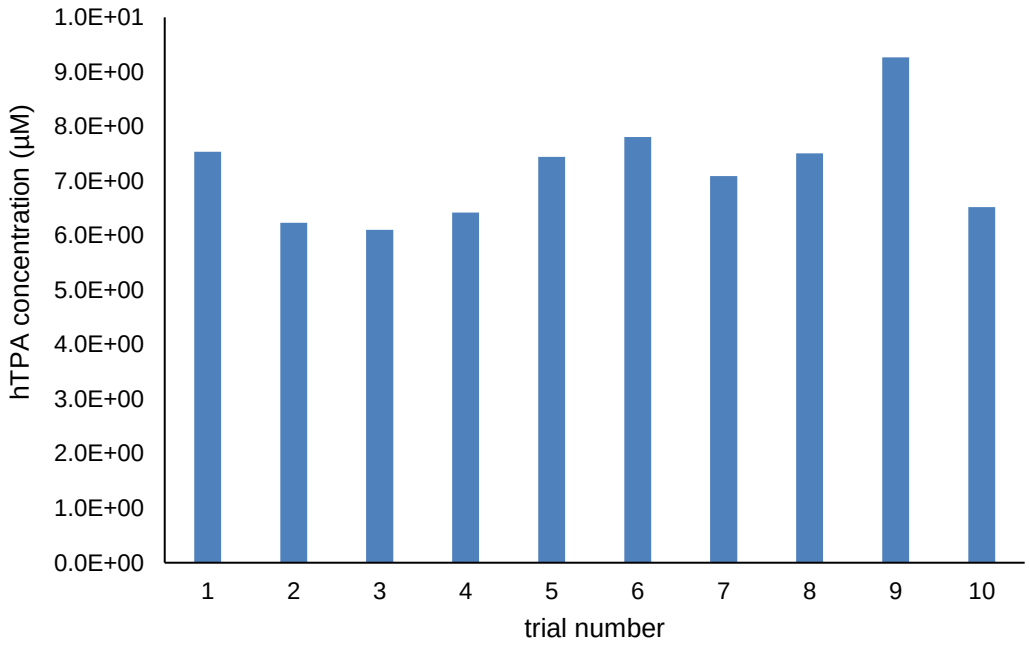

Figure 2.6. The concentration of hTPA at different repetitions

2.4.3. Hydroxyl radical generation and photodegradation mechanism

Hydroxyl radicals have been considered as the major species responsible for the TiO_2-catalyzed photodegradation of organic compounds[45]. Other reactive oxygen species, such as superoxide ($^{\bullet}O_2^-$), hydrogen peroxide (H_2O_2) and hydroperoxyl radical ($HO_2^{\bullet}$) do not participate in the TiO_2-catalyzed photodegradation of TPA[44]. Photodegradation studies of

GSM and MIB with the P25 catalyst in the presence of •OH scavengers Br^- and tertiary butyl alcohol showed a significant reduction in their degradation rates[49].

The TPA experiments show that the steady-state •OH concentrations ([•OH]ss) were 6.13 × 10^{-18} µM, 2.86 × 10^{-16} µM and 3.71 × 10^{-14} µM for dark condition, UV-A only and UV-A illumination in the presence of PS3T catalyst, respectively. ([•OH]ss) is determined from the slope of ln{$[TPA]_0$/($[TPA]_0$-[hTPA])} versus time (Figure 2.7), where $[TPA]_0$ is the initial TPA concentration[58], as described below. The higher activity in the presence of PS3T photocatalyst can be related to the efficient generation of •OH under UV illumination.

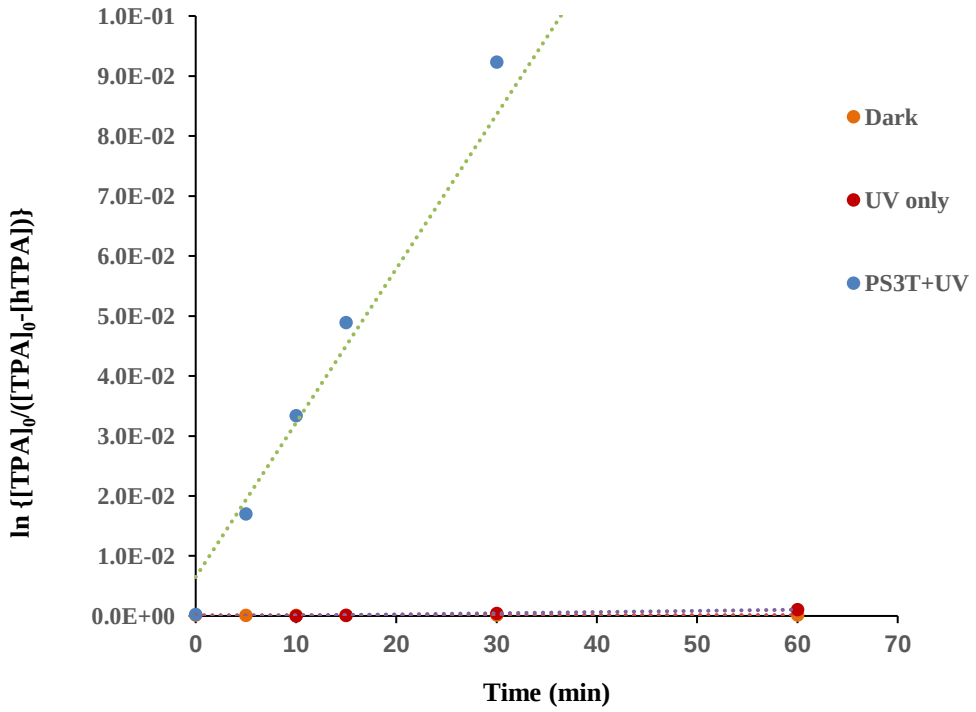

Figure 2.7. The plot of ln{[TPA]0/([TPA]0-[hTPA])} versus time used to determine the steady-state hydroxyl radical concentration in the dark, by UV only and in the presence of the PS3T catalyst and UV radiation

The reaction of •OH with the terephthalic acid (TPA) probe is overall second-order (Eq. 1), [44]

$$\mathrm{TPA} + \cdot\mathrm{OH} \xrightarrow{k_{\mathrm{TPA}}^{\cdot\mathrm{OH}}} \mathrm{hTPA} \qquad (1)$$

In the presence of a photocatalyst, •OH concentration reaches to a steady-state value ($[\bullet OH]_{ss}$). The hTPA (2-hydroxyterephthalic acid) production rate can be expressed with respect to $[\bullet OH]_{ss}$

$$\frac{d[\mathrm{hTPA}]}{dt} = Yk_{\mathrm{TPA}}^{\cdot\mathrm{OH}}[\cdot\mathrm{OH}]_{ss}[\mathrm{TPA}] = Yk_{\mathrm{TPA}}^{\cdot\mathrm{OH}}[\cdot\mathrm{OH}]_{ss}([\mathrm{TPA}]_0 - [\mathrm{hTPA}]) \qquad (2)$$

where Y is the percent yield of the reaction of TPA with •OH = 35%[58] and $k_{\mathrm{TPA}}^{\cdot\mathrm{OH}}$ is the Second-order rate constant = 3.3×10^9 M^{-1} s^{-1}[58].

$$\int_0^{[\mathrm{hTPA}]} -\frac{1}{[\mathrm{TPA}]_0 - [\mathrm{hTPA}]} d([\mathrm{TPA}]_0 - [\mathrm{hTPA}]) = \int_0^t Yk_{\mathrm{TPA}}^{\cdot\mathrm{OH}}[\cdot\mathrm{OH}]_{ss}\,dt \qquad (3)$$

$$\ln\frac{[\mathrm{TPA}]_0}{[\mathrm{TPA}]_0 - [\mathrm{hTPA}]} = Yk_{\mathrm{TPA}}^{\cdot\mathrm{OH}}[\cdot\mathrm{OH}]_{ss}\,t \qquad (4)$$

$[\bullet OH]_{ss}$ can be determined from the slope of the linear regression plot of $\ln\{[TPA]_0/([TPA]_0-[hTPA])\}$ versus time.

A mechanistic study to identify mechanisms and reaction intermediates for the photocatalytic degradation of MIB and GSM in the presence of colloidal TiO_2 has been conducted by Fotiou et al.[49]. They proposed that GSM photodegradation in the presence of TiO_2 produces two main products 8a-Hydroxy-4a-methyl-octahydro-naphthalen-2-one (α-hydrogen abstraction from the tertiary carbon of GSM, β-scission abstraction, followed by hydroxylation from •OH attack) and 8,8a-dimethyl-decahydro-naphthalen-1-ol (dehydration of GSM and •OH addition followed by π bond rearrangement. The dehydration product of MIB 1,2,7,7-tetramethyl-bicyclo[2.2.1]hept-2-ene is converted to

1,6,7,7-tetramethyl-bicyclo[2.2.1]hept-5-en-2-ol due to the •OH attack. Due to β scission, subsequent H elimination, and •OH addition of MIB, several diketones are produced as other intermediate degradation products. The reaction products are shown in Figures 2.8 and 2.9.

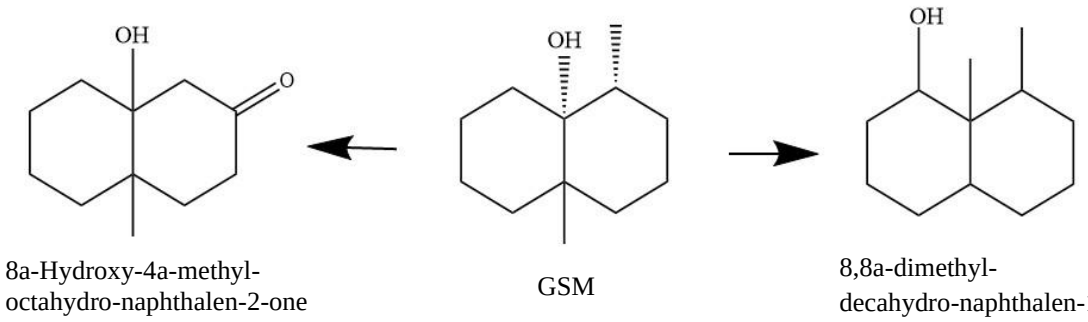

8a-Hydroxy-4a-methyl-octahydro-naphthalen-2-one

GSM

8,8a-dimethyl-decahydro-naphthalen-1-

Figure 2.8. Main products of GSM photodegradation in the presence of TiO_2

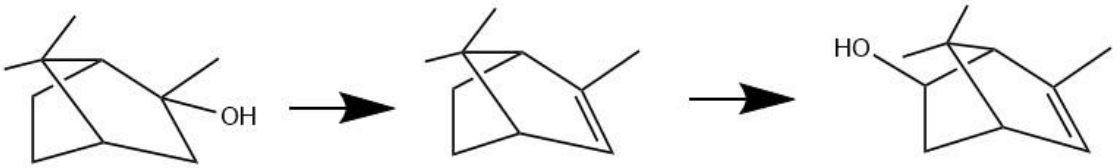

MIB

1,2,7,7-tetramethyl-bicyclo[2.2.1]hept-2-ene

1,6,7,7-tetramethyl-bicyclo[2.2.1]hept-5-en-2-ol

Figure 2.9. Main products of MIB photodegradation in the presence of TiO_2

2.4.4. Robustness of catalyst films

Despite photocatalytic effectiveness with respect to degradation of MIB and GSM, direct immobilization of P25 on glass substrates does not produce a robust coating. This was observed for the P and PT catalysts that contained P25 and would readily exfoliate with gentle rubbing. To increase the robustness of the catalyst films, SiO_2 was added to the TiO_2 sol-gel mixture while maintaining a constant Ti concentration. The catalysts with SiO_2 consistently exhibited higher robustness according to the cross-tape adhesion test that is designed to test the adherence strength of coatings[21,48].

The PS3T catalyst film that was synthesized with the addition of 3% Si sol-gel mixture to the powder-modified TiO_2 mixture showed the highest photodegradation rate (Table 2.2) with better adhesion to the glass substrate. Catalyst P that was synthesized without TiO_2-SiO_2 sol-gel mixture showed poor adhesion. This catalyst was classified under ASTM class 0 B, indicating that >65% of the coating in the cross-cut area was removed. The PS3T film was classified under 5B, where none of the coatings in the cross-cut area was removed. The robustness of the catalyst coatings increased with the Si content in the sol-gel mixture. At the same time, increased Si content in the catalyst resulted in a decrease in photocatalytic activity (Figure 2.4, Table 2.2). The decrease in the activity can be attributed to lower P25 surface coverage due to a higher amorphous SiO_2 content and lower surface TiO_2 content, as observed from catalyst characterization data below.

The leached Ti and Si concentrations were measured after 60 min of TPA photodegradation in the presence of the PS3T catalyst. The leached concentrations for both elements were at or below the detection limit of the instrument (Table 2.3). Presently, the U.S. Environmental Protection Agency does not have maximum contaminant limits for Ti and

Si in drinking water. The detection limit of the ICP-AES was 0.04 and 0.01 mg L^{-1} for Si and Ti, respectively. A toxicological study on rats suggested a maximum contaminant level of 0.1 mg L^{-1} for Ti in drinking water[59]. This concentration is an order of magnitude higher than the Ti concentrations leached after 60 min from the PS3T catalyst (Table 2.3).

Table 2.3. Photoleaching of Si and Ti from the photocatalyst

Sample	**Si (mg L^{-1})**	**Ti (mg L^{-1})**
Blank	<0.04	0.0112
Trial 1	<0.04	0.0107
Trial 2	<0.04	0.0159
Trial 3	<0.04	0.0107

2.4.5. Catalyst characterization

The XRD patterns obtained for different substrates are shown in Figure 2.10. All peaks were assigned according to the International Centre for Diffraction Data, Powder Diffraction File (ICCD, PDF 01-080- 6402). The catalyst film that was coated with the TiO_2-SiO_2 sol-gel mixture (ST) did not show a TiO_2 peak, suggesting that film was amorphous to be identified by XRD. The catalyst film T showed only anatase (101) crystal peak at $2\theta = 25.3^{\circ}$ as the prominent peak. Catalyst films containing P25 showed both anatase and rutile peaks. Diffraction peaks at $2\theta = 25.3^{\circ}$, 37.8°, 48.0°, and 55.1° can be indexed to (101), (004), (200), and (211) crystal planes of anatase, respectively. Crystal planes of rutile (110), (101), and (211) showed peaks at $20 = 27.4^{\circ}$, 36.1° , and 54.1°, respectively (Figure 2.10).

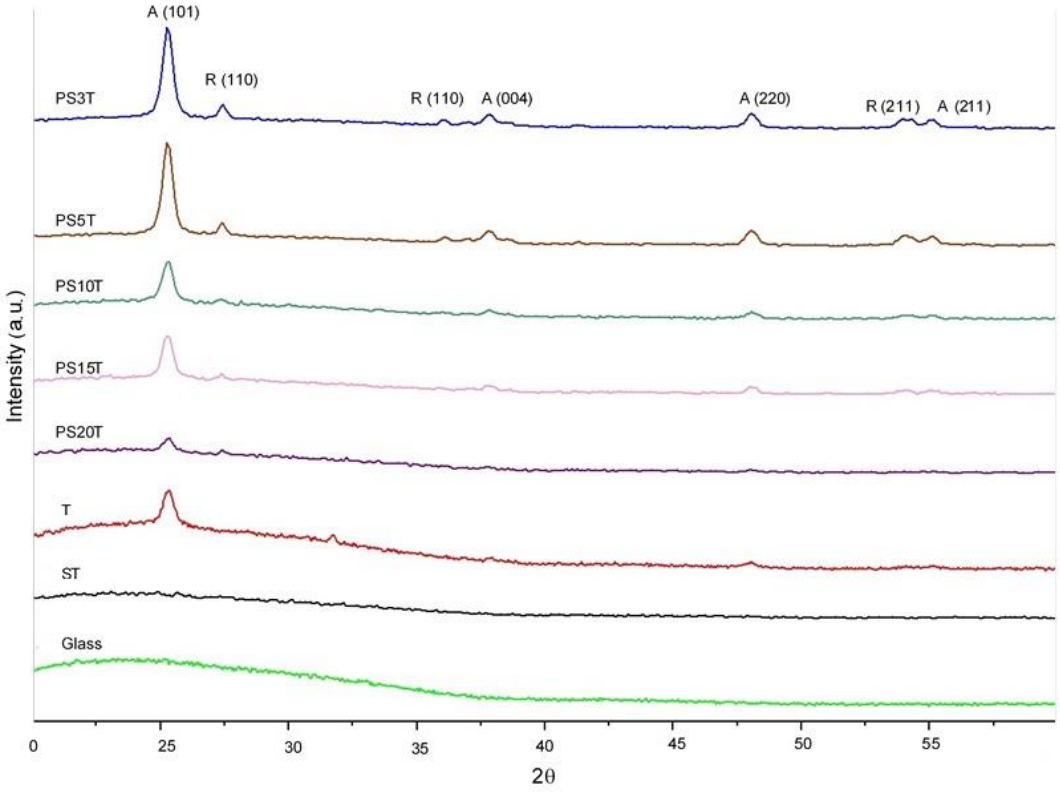

Figure 2.10. The X-ray diffractogram of the photocatalyst films

The P25 anatase:rutile ratio is reported at 70:30 (wt%)[60,61]. TiO_2-based photocatalysts having anatase and rutile crystalline phases show better photocatalytic activity towards organic compounds than catalysts with anatase alone[62]. This higher activity is attributed to the prevention of recombination of electrons and holes because the mixed rutile and anatase crystalline phases facilitate efficient electron-hole separation[33,62–64]. Recent combined theoretical and experimental studies have shown that anatase has a higher affinity towards electrons[33]. Therefore, photogenerated electrons in the conduction band flow from rutile to anatase, stabilizing the holes generated in rutile by preventing recombination. Alternatively, other studies have proposed the transfer of photogenerated conduction band electrons from anatase to rutile[65–67]. When Si content increases in the catalyst, reduction of diffraction line intensity is observed for both anatase and rutile, and this is accompanied by the appearance of a broad feature at low 2θ (<35˚) characteristic of amorphous SiO_2 (Figure 2.10). This reduction in peak intensities is a result of the additional SiO_2, which reduces the TiO_2 concentration in the mixture[38,68]. It has also been shown that the coexistence of SiO_2 prevents the rearrangement of TiO_2 and limits the growth of TiO_2 crystallites following calcination of the sol-gel mixture[69,70], even though in this study, the photocatalytic activity occurs largely due to the presence of P25.

The IR spectra of the catalyst films are shown in Figure 2.11. The absorption band at 1620 cm^{-1} is attributed to the bending vibrations of surface adsorbed water. The broad absorption band around 600 cm^{-1} is due to the stretching vibrations of Ti-O-Ti and Ti-O bonds that is characteristic of the formation of a Ti-O-Ti network. Compared to the IR spectrum of pure P25, IR spectra of catalysts with SiO_2 showed additional absorption bands at ~1050 cm^{-1} and ~950 cm^{-1} that are ascribed to the asymmetric stretching vibrations of Si-O-Si and Ti-

O-Si bonds, respectively[68,71]. At higher SiO_2 concentrations (e.g., PS20T), these bands become more prominent, suggesting the formation of a Ti-O-Si network that is the result of the fusion of TiO_2 and SiO_2 sol-gel, as well as an increase in the Si-O-Si bonds.

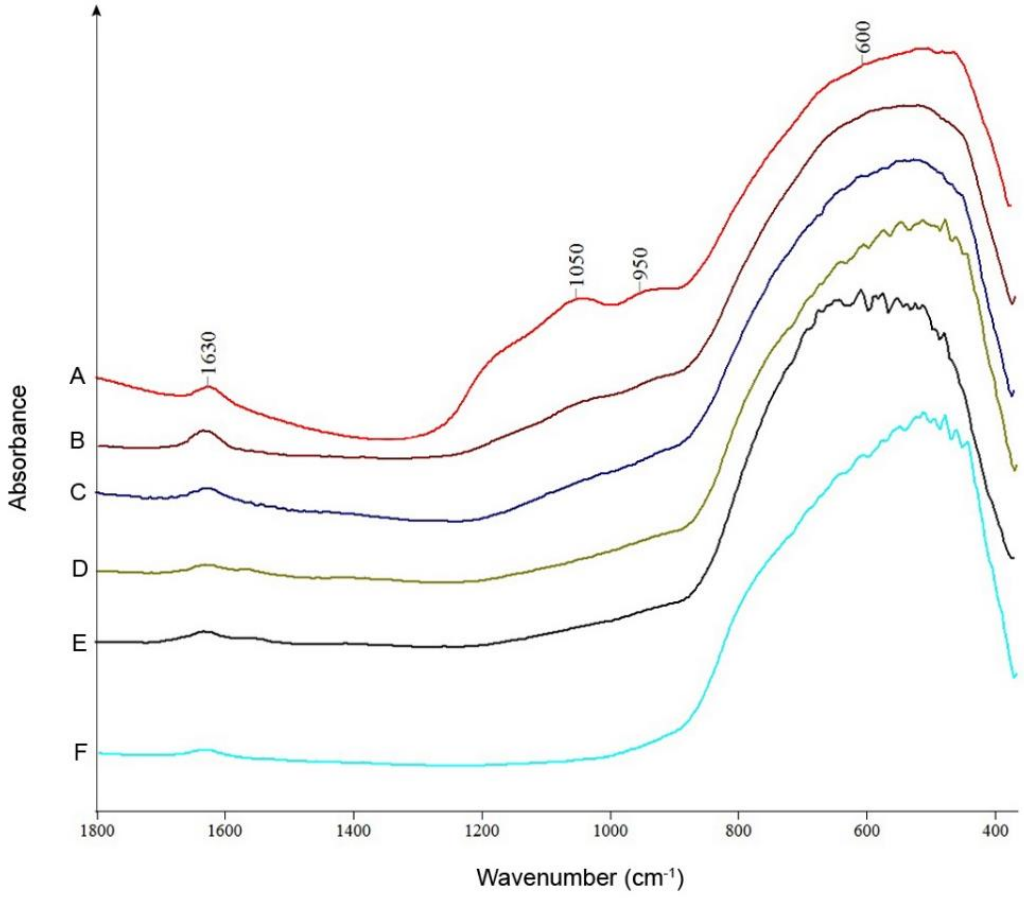

Figure 2.11. The FT-IR spectra for the (A) PS20T; (B) PS15T; (C) PS10T; (D) PS5T; (E) PS3T; and (F) P-25 photocatalysts

Bandgap energies of the powder-enriched catalyst films were assessed by the UV–vis diffuse reflectance spectra (Figure 2.12). Catalyst coating without any SiO_2 (PT catalyst) showed bandgap energy of 3.23 eV, which is in good agreement with the reported value of 3.2 eV for commercial P25 TiO_2[72]. However, the reflectance band shifted to a lower wavelength with increasing Si concentration in the catalyst films, indicating a

widening of bandgap, where the highest Si-containing catalyst PS20T showed the widest bandgap among the catalyst films. This blue shift of the band edge has been associates with an increase in the dispersion of titania crystallites in the catalyst film that can be attributed to the quantum size effect[46,73].

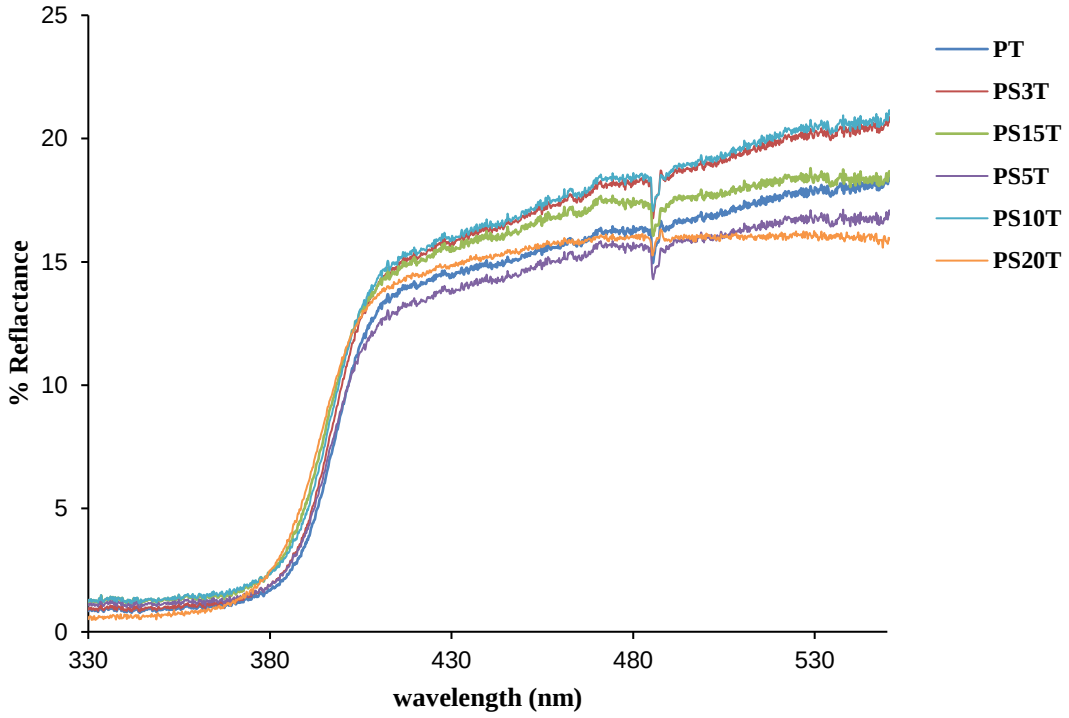

Figure 2.12. The UV-Vis diffuse reflectance spectra of the photocatalysts

The XPS analysis was employed to identify elemental composition from the top 10 nm of the surface. XPS analyses of different catalysts show that surface coverage of Ti changes with the amount of Si added in the initial sol-gel mixture (Figure 2.13-2.20).

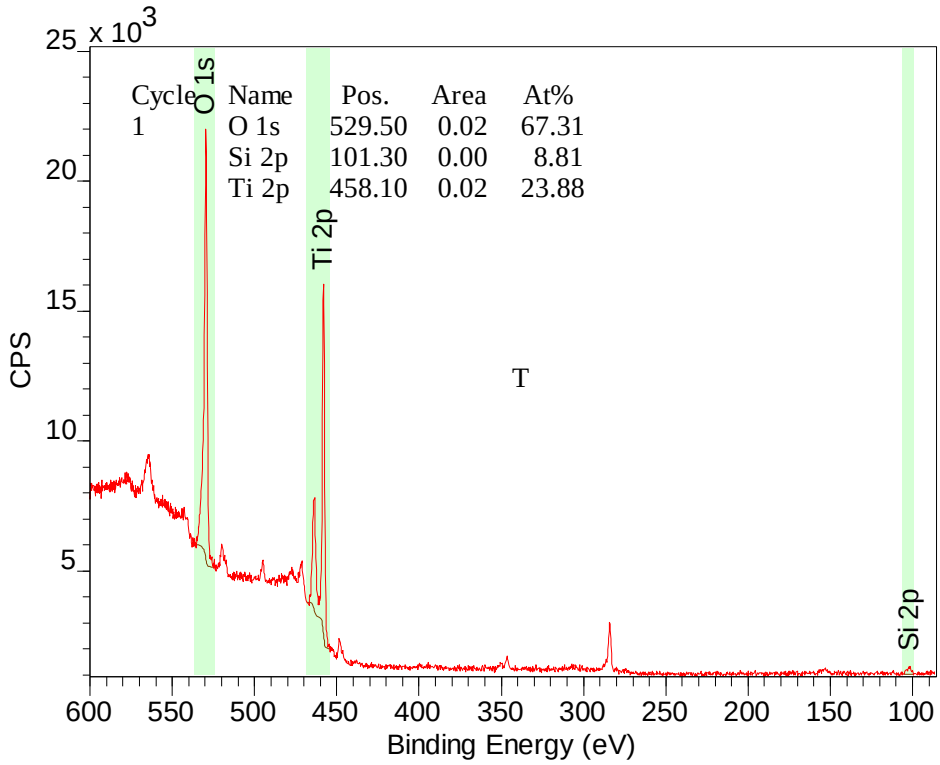

Figure 2.13. The XPS spectrum for the T photocatalyst

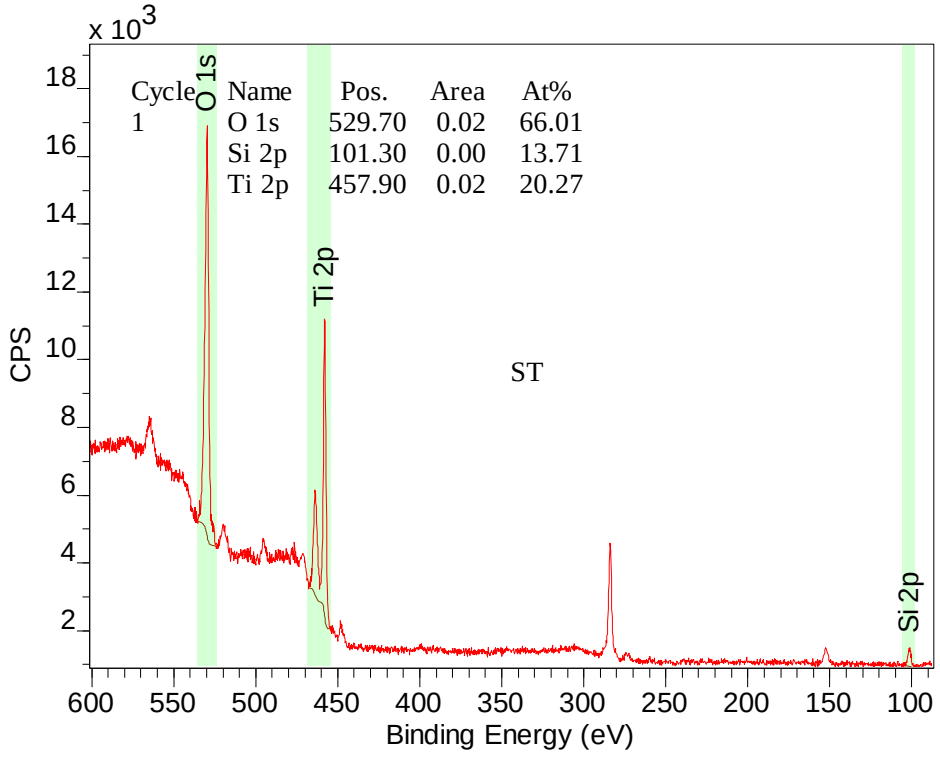

Figure 2.14. The XPS spectrum for the ST photocatalyst

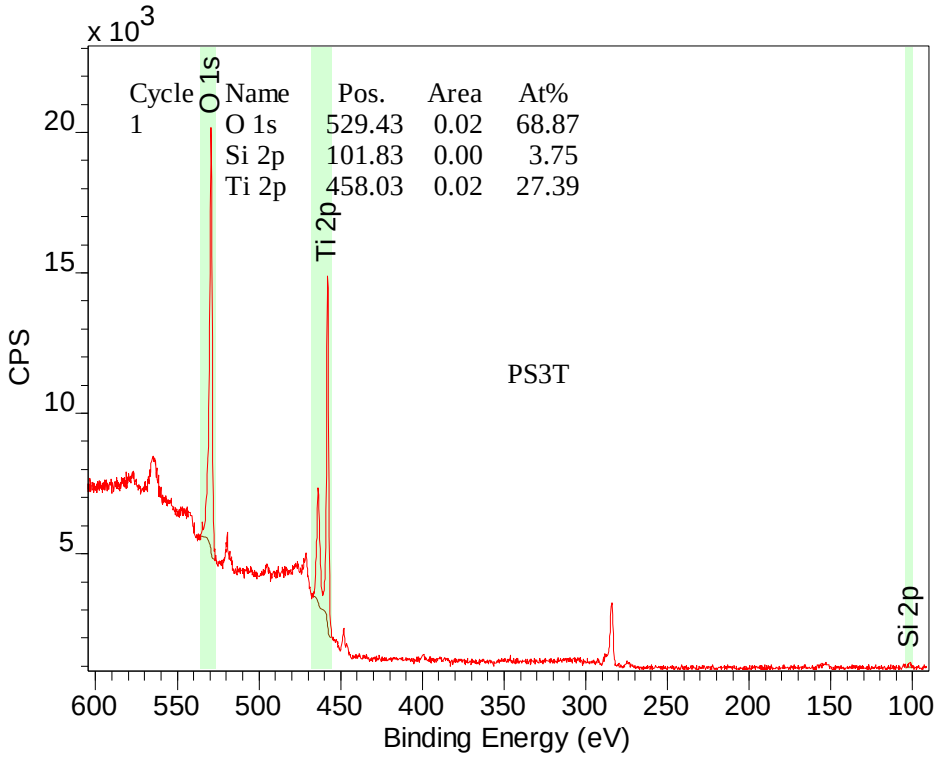

Figure 2.15. The XPS spectrum for the PS3T photocatalyst

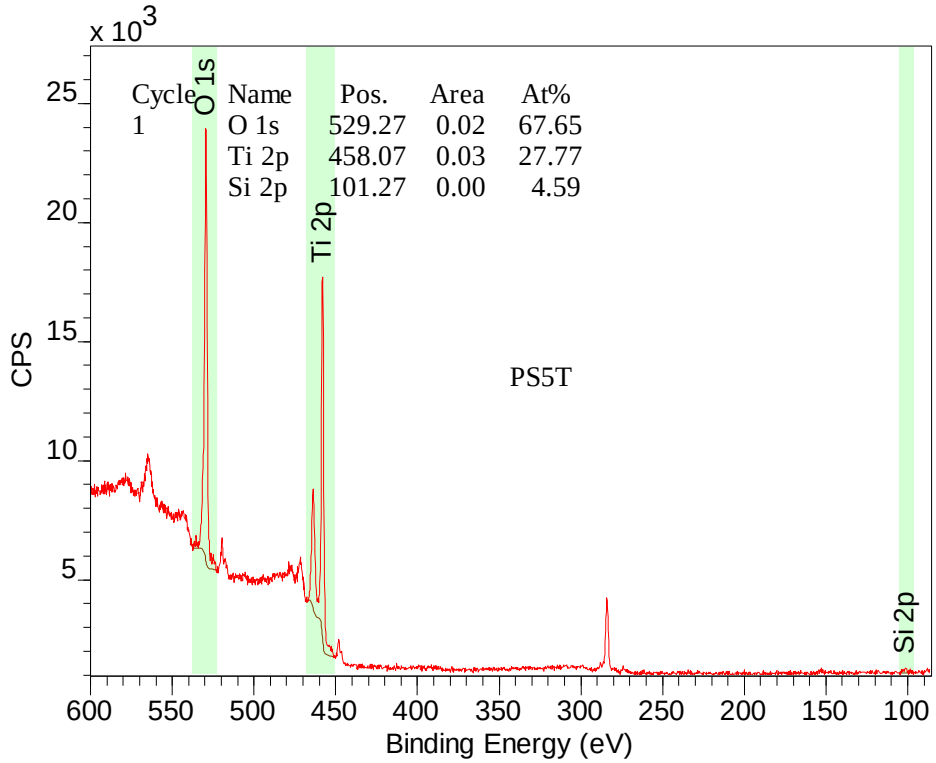

Figure 2.16. The XPS spectrum for the PS5T photocatalyst

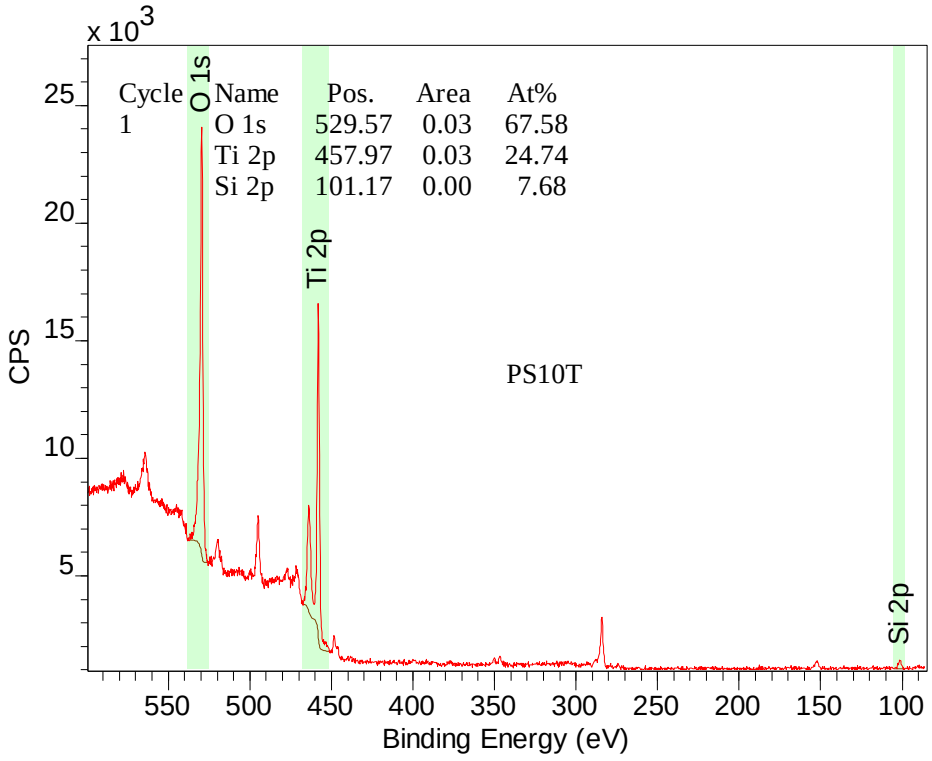

Figure 2.17. The XPS spectrum for the PS10T photocatalyst

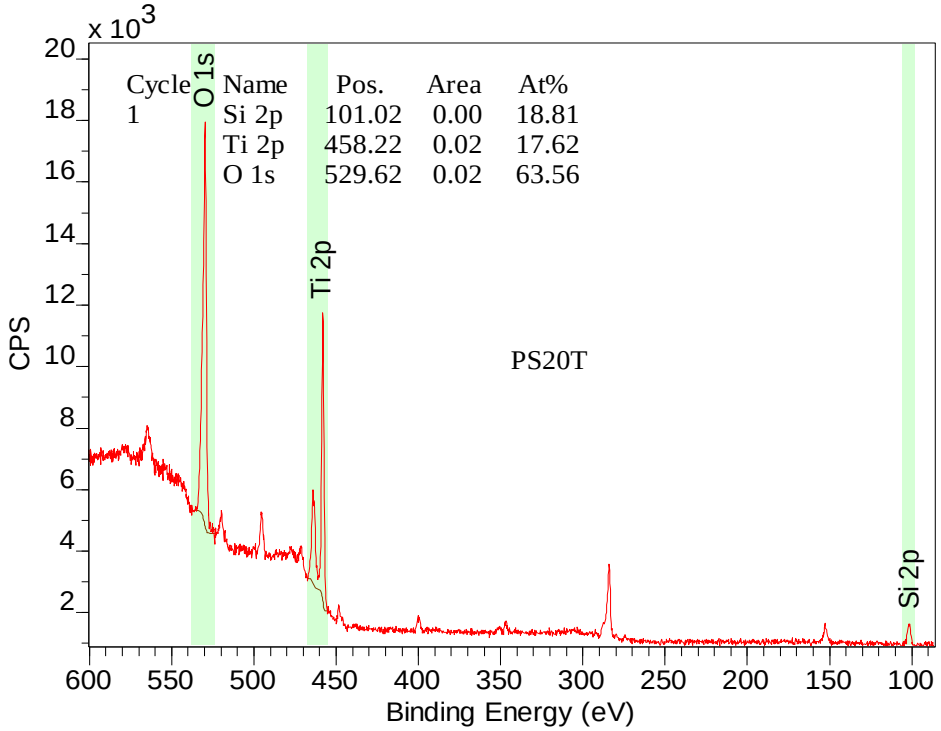

Figure 2.18. The XPS spectrum for the PS20T photocatalyst

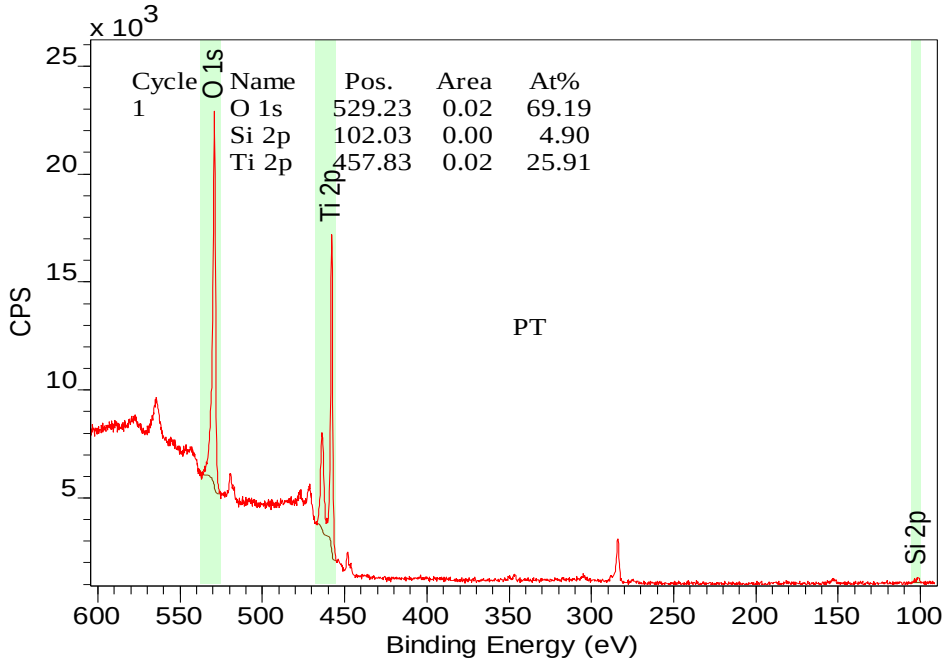

Figure 2.19. The XPS spectrum for the PT photocatalyst

XPS spectrum for one of the catalyst films (PS15T) shown in Figure 2.20 indicates the peaks for Ti, O, C, and Si elements. The peak for C is due to adventitious carbon. The C 1*s* peak at 284 eV is derived from the adventitious carbon used to calibrate the binding energy scale of the XPS data.

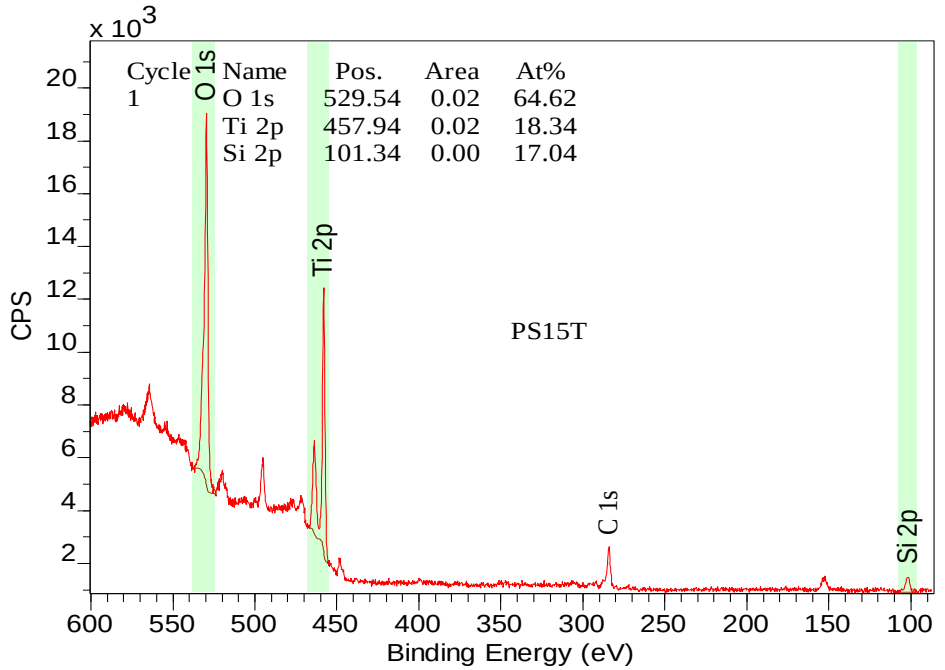

Figure 2.20. The XPS spectrum for the PS15T photocatalyst

Figure 2.21 shows k_{app} values for MIB photodegradation versus the Ti: Si surface ratio, as determined by the XPS. A near-positive linear relationship is observed between the k_{app} and Ti:Si ratio when the latter is >2. Decreasing the SiO_2 content in the initial sol-gel mixture increases the Ti availability on the surface, as shown in XPS, which in turn increases the photocatalytic degradation of taste and odor compounds in water.

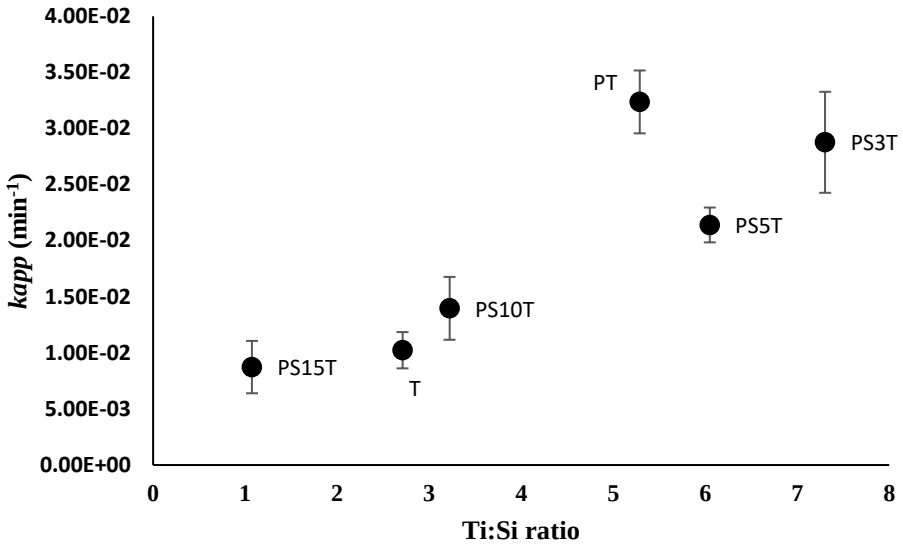

Figure 2.21. The apparent rate constants (k_{app}) for the MIB (initial concentration 500 ng L^{-1}) photodegradation versus the surface atomic Ti:Si ratio as determined by the XPS

Figure 2.22 shows the k_{app} values for MIB photodegradation versus the bulk Ti:Si ratio obtained by the ICP-AES. In contrast to the XPS data that shows the Ti:Si ratio in the catalyst surface (Figure. 2.21), the bulk Ti:Si ratio does not show a linear relationship with k_{app} values. This further proves the catalyst efficiency is controlled by the availability of surface Ti photocatalytic sites.

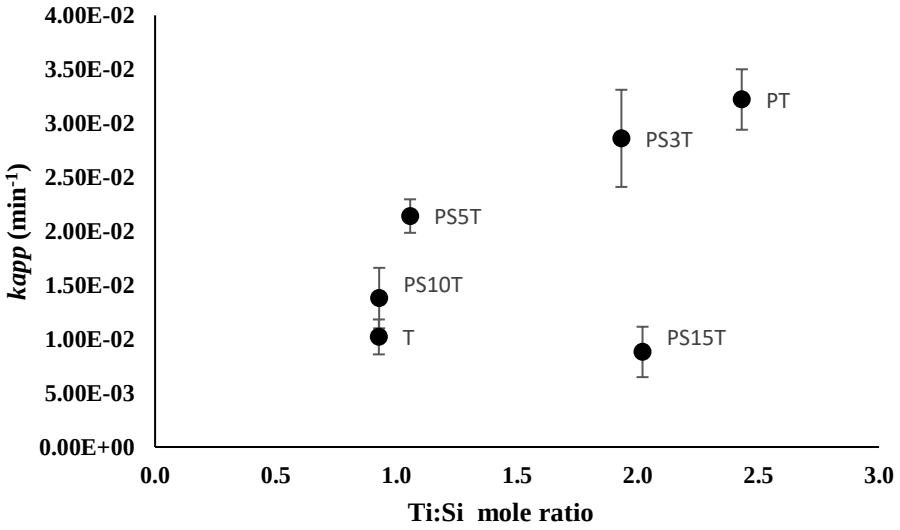

Figure 2.22. The apparent rate constants (k_{app}) for the MIB (initial concentration 500 ng L^{-1}) photodegradation versus the bulk Ti:Si mole ratio of catalyst films as determined by the ICP-AES

In contrast to our observed decrease in the photocatalytic degradation rate with an increase in SiO_2 concentration, several studies of photodegradation of dyes and viruses by suspensions of TiO_2-SiO_2 photocatalysts have shown the opposite trend; i.e., an increase in the photodegradation rate with increasing SiO_2 concentration[30,38,75]. This has been attributed to the enhanced adsorption of the pollutants[30,38,75], increased surface acid sites[30], quantum confinement[68], and minimization of agglomeration of TiO_2 that leads to a higher exposed surface area in the presence of SiO_2[76]. In our study, the presence of Ti-O-Si bonds at higher SiO_2 concentrations resulted in lower photocatalytic activity. The existence of amorphous SiO_2, which covers the surface of the TiO_2 films, as shown by XPS, also leads

to lower photocatalytic activity. This proves that photocatalytic degradation of MIB and GSM is dependent on Ti content on the surface, and adsorption of our target compounds at higher Si contents does not play a role in enhancing the photodegradation.

Figure 2.23 shows the photoluminescence spectra of the PT and the PS20T catalysts. The photoluminescence spectra characterize the separation efficiency of holes and electrons in semiconductor materials, where the intensity of the fluorescence peak is mainly dependent on the rate of recombination of holes and electrons[77,78]. The photoluminescence intensity is lowered in the PT catalyst compared to that in the T catalyst (Figure 2.23), suggesting that electron-hole recombination is effectively suppressed by the presence of both crystalline phases in the PT catalyst. The incorporation of SiO_2 further reduces the photoluminescence for the PS20T catalyst (Figure 2.23), which agrees with the previous photoluminescence studies on SiO_2-incorporated TiO_2[46]. In order to further study the recombination efficiency of each catalyst film, time-resolved photoluminescence is proposed for future research.

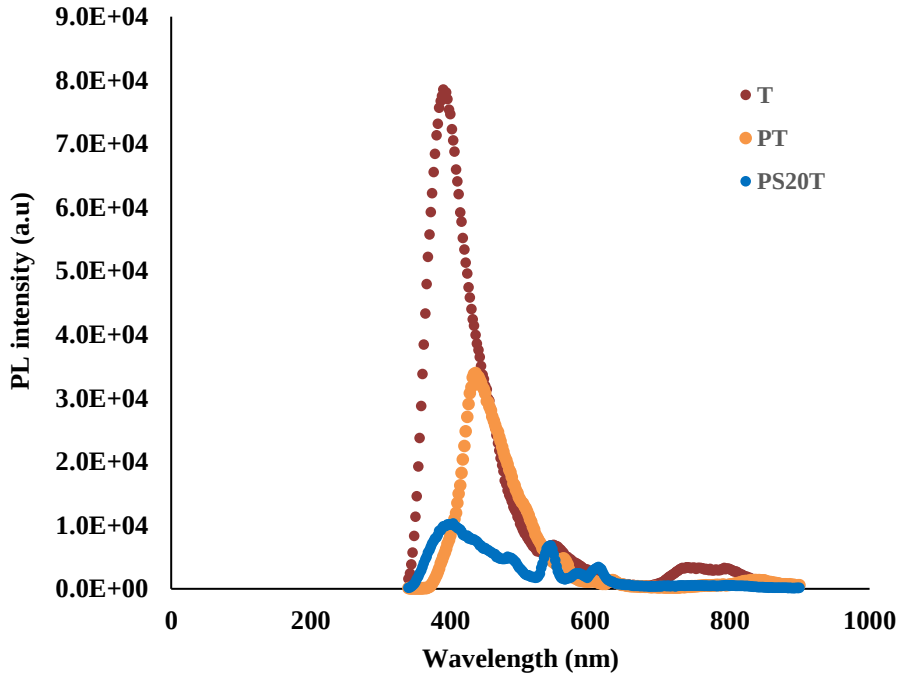

Figure 2.23. Photoluminescence spectra of the T, PT, and PS20T photocatalyst films

Even though suppression of electron-hole recombination by SiO_2 normally enhances the activity of a catalyst, this was not observed in our study. This may be due to the lower availability of surface Ti catalytic sites in the presence of Si, as observed in the XPS results (Figure 2.21).

The SEM micrographs of the catalyst films that contained P25 show that the P25 aggregates are covered by TiO_2 and SiO_2 nanoparticles (Figure 2.24 and Figure 2.25).

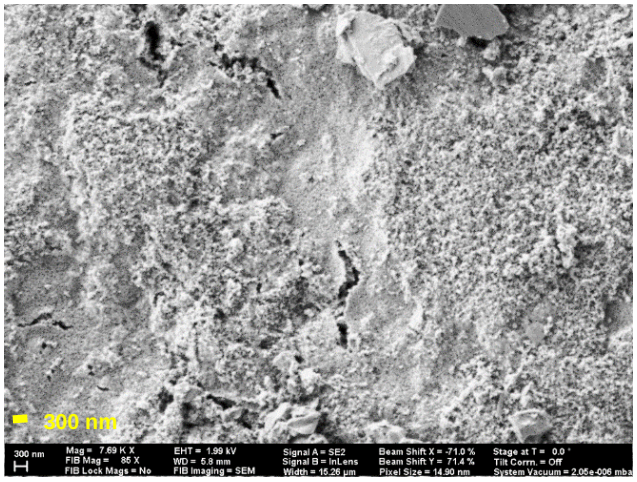

Figure 2.24. The SEM micrograph of the photocatalyst films PS3T high magnification

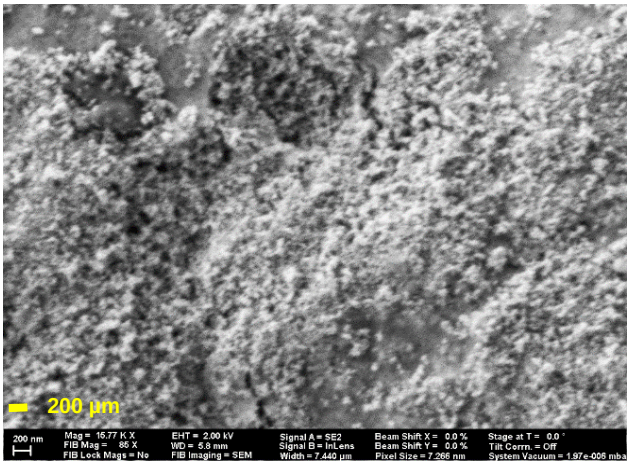

Figure 2.25. The SEM micrograph of the photocatalyst films PS20T high magnification

Figure 2.26 shows the presence of micro-cracks in the PS3T film. These microcracks emerge due to the small residual compressive stresses[79] occurring during drying, crystallization, and densification processes[80]. Differences in the morphologies of PS3T and PS20T catalysts were observed (Figure 2.26 and Figure 2.27).

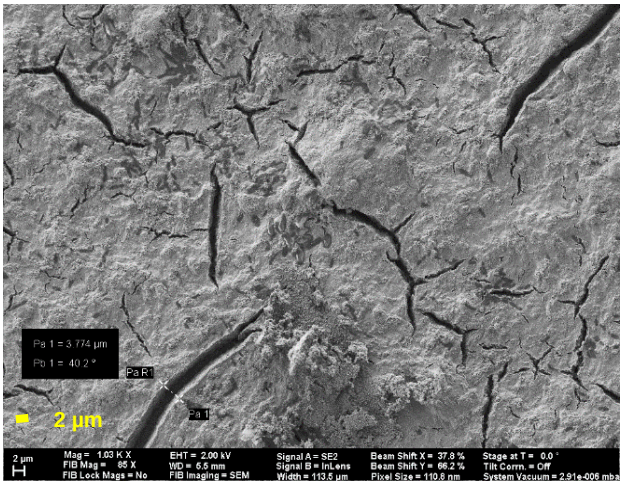

Figure 2.26. The SEM micrograph of the photocatalyst films PS3T low magnification

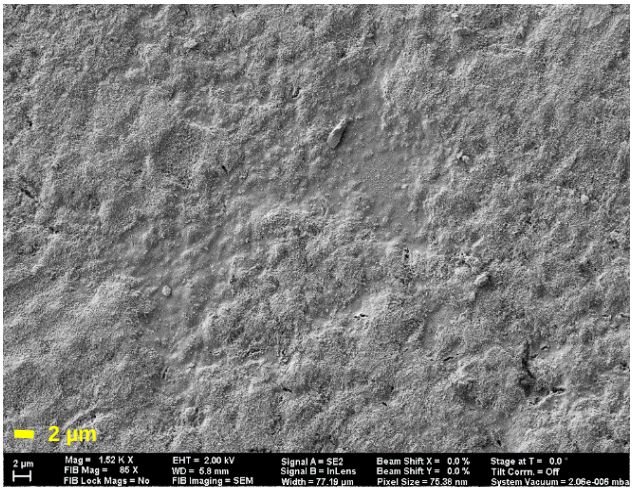

Figure 2.27. The SEM micrograph of the photocatalyst films PS20T low magnification

Increasing the Si content of the catalyst films reduces the formation of microcracks of the powder-modified films and brings about higher robustness. It has been found that the addition of SiO_2 to TiO_2 nanoparticles can minimize the agglomeration of TiO_2 particles and thereby result in a better dispersion in the sol-gel mixture and less microcracks upon drying and calcination[36,38].

The SEM micrographs of the catalyst film T show a smooth surface with some cracks/flakes (Figure 2.28 and Figure 2.29), while the ST film shows some surface roughness but less cracks (Figure 2.30 and Figure 2.31).

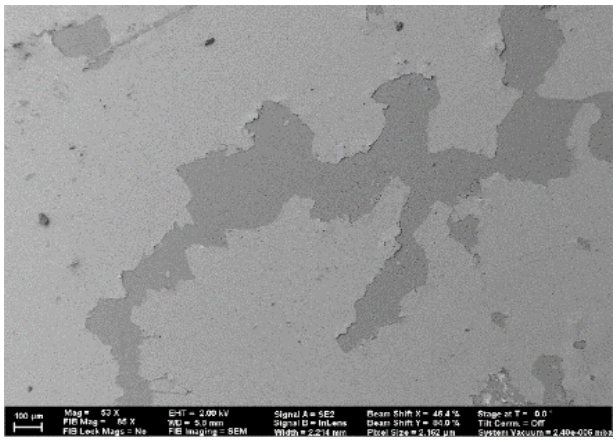

Figure 2.28. SEM micrograph of the photocatalyst films T low magnification

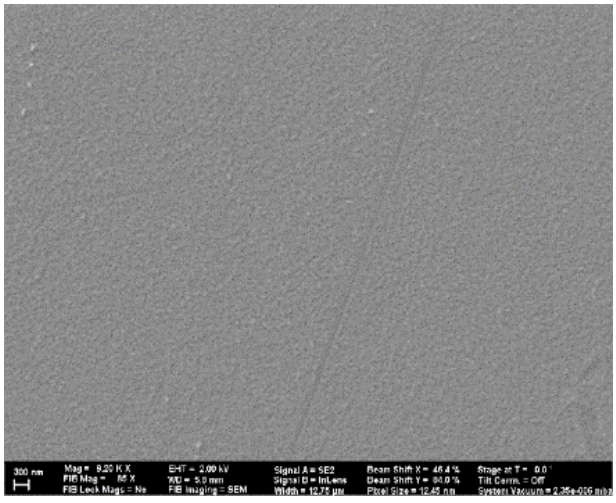

Figure 2.29. SEM micrograph of the photocatalyst films T high magnification

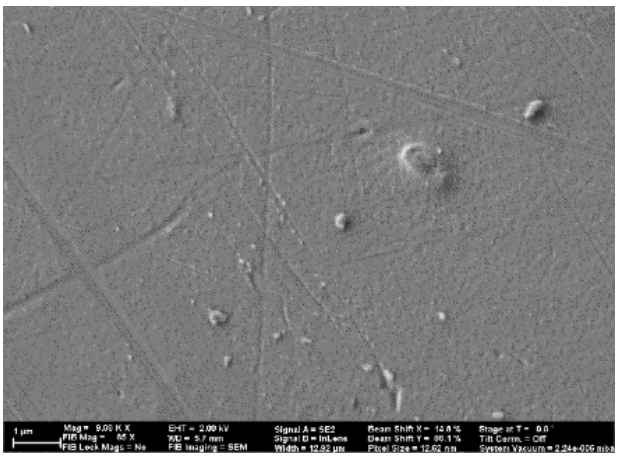

Figure 2.30. SEM micrograph of the photocatalyst films ST low magnification

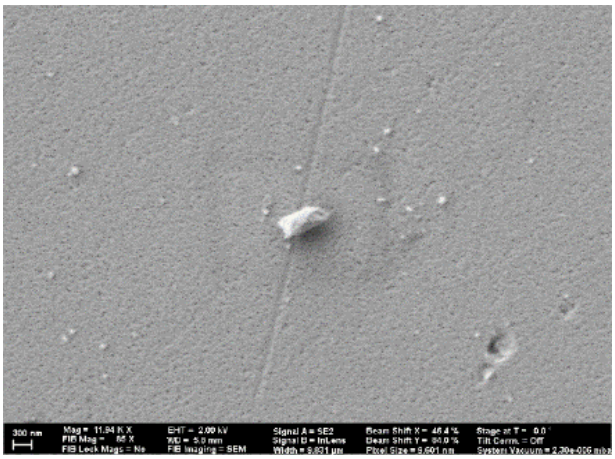

Figure 2.31. SEM micrograph of the photocatalyst films ST high magnification

The stability of the films are found to increase by adding SiO_2 because of the effect it has on delaying the crystallization of TiO_2 to anatase[81]. The SEM micrographs of other catalyst films that contained P25 and different concentrations of SiO_2 show a rough surface with diminishing microcracks with increasing the SiO_2 (Figure 2.32-2.37).

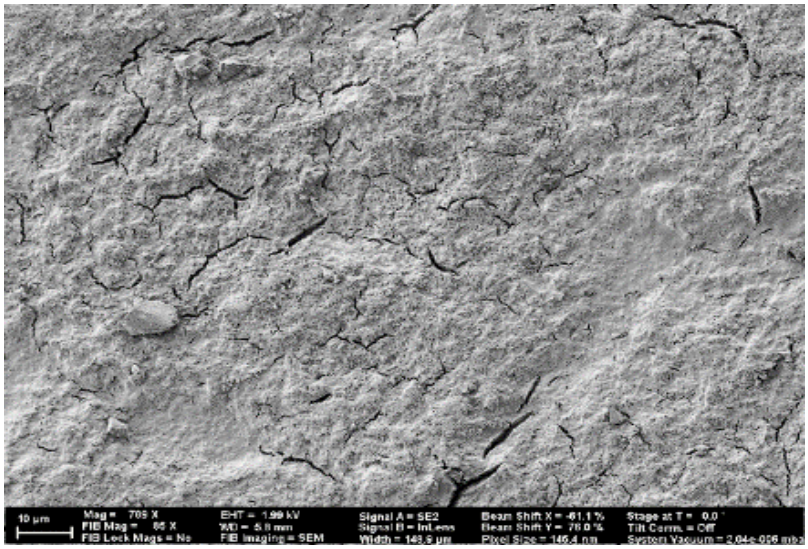

Figure 2.32. SEM micrograph of the photocatalyst films PS5T low magnification

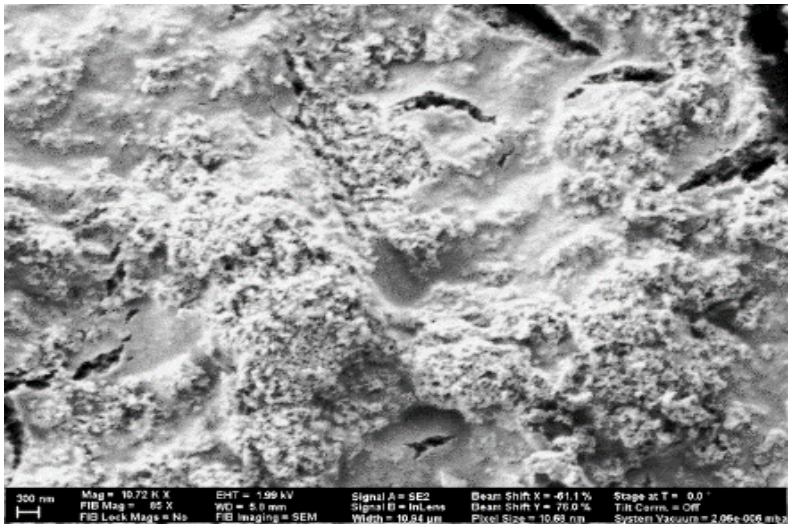

Fugure 2.33. SEM micrograph of the photocatalyst films PS5T high magnification

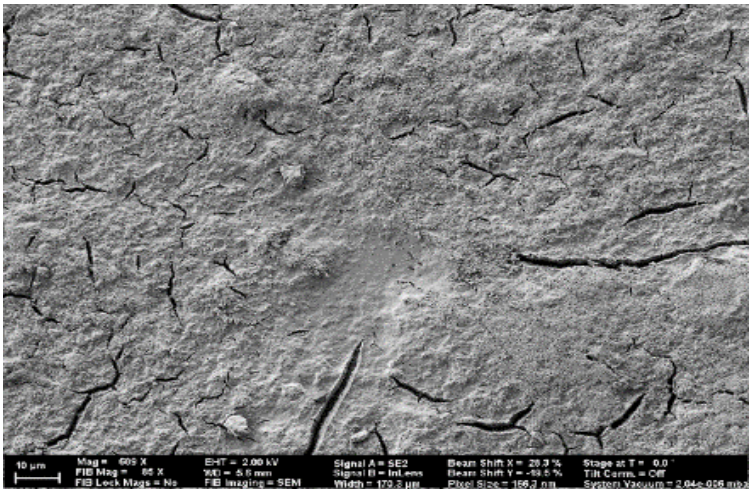

Figure. 2.34. SEM micrograph of the photocatalyst films PS10T low magnification

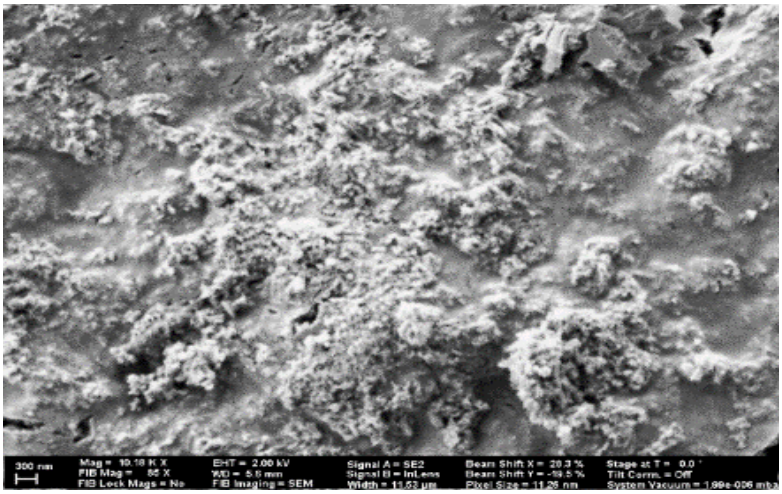

Figure. 2.35. SEM micrograph of the photocatalyst films PS10T high magnification

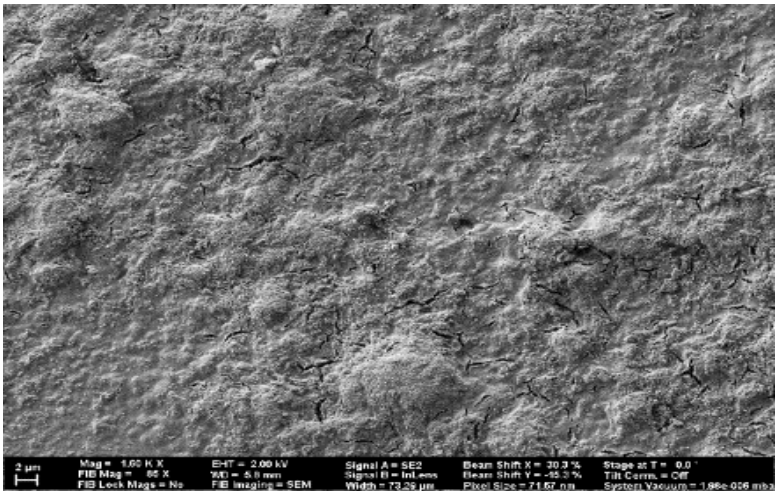

Figure 2.36. SEM micrograph of the photocatalyst films PS15T low magnification

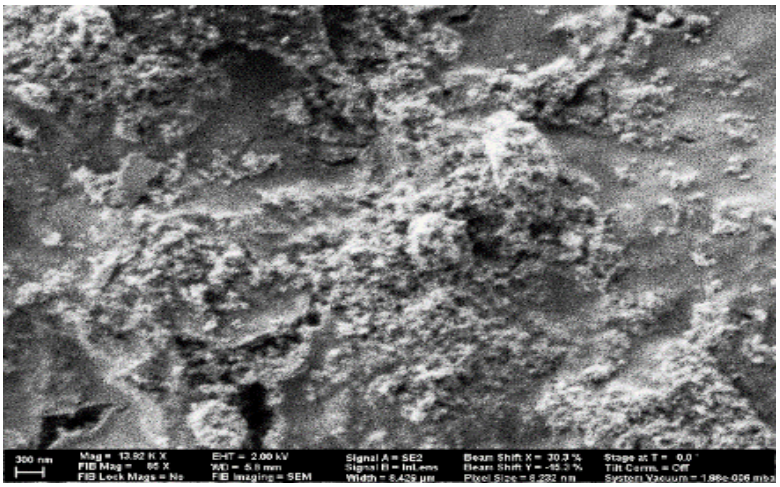

Figure 2.37. SEM micrograph of the photocatalyst films PS15T high magnification

2.5. Conclusions

The results obtained in this study show that P25 powder- modified catalyst films have the ability to photodegrade taste and odor compounds more efficiently than the UV-only treatment. P25 immobilized onto the glass substrate without the TiO_2-SiO_2 sol-gel coating, despite its high photocatalytic efficiency, did not have a strong and stable adherence; the sol-gel mixture assists in binding P25 to the substrate robustly. The powder-modified catalyst film at a-Si:Ti ratio = 3% was able to degrade ~80% of MIB within an hour. Higher SiO_2 concentrations in the catalyst films caused an improved adhesion of P25 to the glass substrate, but a decrease in their photocatalytic activity with respect to the taste and odor compounds was observed. The observed photodegradation rates did not show any relationship to the total Ti concentration in the catalyst films; instead, the rate correlated with the surface (0–10 nm) Ti: Si ratio (as determined by the XPS). The technology developed here involving an immobilized photocatalyst enhances the UV activity without the need for the removal of particulate catalysts using separation/filtration schemes. These catalyst films can be used to augment the existing UV disinfection systems for the removal of taste and odor compounds and other organic pollutants in drinking water and wastewater treatment facilities.

2.6. REFERENCES

(1) US EPA, O. National Primary Drinking Water Regulations https://www.epa.gov/ground-water-and-drinking-water/national-primary-drinking-water-regulations (accessed 2017 -05 -01).

(2) US EPA, O. Long Term 2 Enhanced Surface Water Treatment Rule Documents https://www.epa.gov/dwreginfo/long-term-2-enhanced-surface-water-treatment-rule-documents (accessed 2017 -03 -14).

(3) Lester, Y.; Avisar, D.; Mamane, H. Photodegradation of the Antibiotic Sulphamethoxazole in Water with UV/H_2 O_2 Advanced Oxidation Process. *Environmental Technology* **2010**, *31* (2), 175–183. https://doi.org/10.1080/09593330903414238.

(4) Kalan, R. E.; Yaparatne, S.; Amirbahman, A.; Tripp, C. P. P25 Titanium Dioxide Coated Magnetic Particles: Preparation, Characterization and Photocatalytic Activity. *Applied Catalysis B: Environmental* **2016**, *187*, 249–258. https://doi.org/10.1016/j.apcatb.2016.01.008.

(5) Jeppesen, E.; Kronvang, B.; Meerhoff, M.; Søndergaard, M.; Hansen, K. M.; Andersen, H. E.; Lauridsen, T. L.; Liboriussen, L.; Beklioglu, M.; Özen, A.; Olesen, J. E. Climate Change Effects on Runoff, Catchment Phosphorus Loading and Lake Ecological State, and Potential Adaptations. *Journal of Environment Quality* **2009**, *38* (5), 1930. https://doi.org/10.2134/jeq2008.0113.

(6) Ptacnik, R.; Lepistö, L.; Willén, E.; Brettum, P.; Andersen, T.; Rekolainen, S.; Solheim, A. L.; Carvalho, L. Quantitative Responses of Lake Phytoplankton to Eutrophication in Northern Europe. *Aquat Ecol* **2008**, *42* (2), 227–236. https://doi.org/10.1007/s10452-008-9181-z.

(7) Paerl, H. W.; Hall, N. S.; Calandrino, E. S. Controlling Harmful Cyanobacterial Blooms in a World Experiencing Anthropogenic and Climatic-Induced Change. *Science of The Total Environment* **2011**, *409* (10), 1739–1745. https://doi.org/10.1016/j.scitotenv.2011.02.001.

(8) Front Matter. In *Limnology (Third Edition)*; WETZEL, R. G., Ed.; Academic Press: San Diego, 2001; p iii. https://doi.org/10.1016/B978-0-08-057439-4.50001-0.

(9) Boström, B.; Andersen, J. M.; Fleischer, S.; Jansson, M. Exchange of Phosphorus across the Sediment-Water Interface. *Hydrobiologia* **1988**, *170* (1), 229–244. https://doi.org/10.1007/BF00024907.

(10) Zaitlin, B.; Watson, S. B. Actinomycetes in Relation to Taste and Odour in Drinking Water: Myths, Tenets and Truths. *Water Research* **2006**, *40* (9), 1741–1753. https://doi.org/10.1016/j.watres.2006.02.024.

(11) Rosenfeldt, E. J.; Melcher, B.; Linden, K. G. UV and UV/H2O2 Treatment of Methylisoborneol (MIB) and Geosmin in Water. *Journal of Water Supply: Research and Technology - Aqua* **2005**, *54* (7), 423–434.

(12) Cook, D.; Newcombe, G.; Sztajnbok, P. The Application of Powdered Activated Carbon for MIB and Geosmin Removal: Predicting PAC Doses in Four Raw Waters. *Water Res.* **2001**, *35* (5), 1325–1333.

(13) Jung, S. W.; Baek, K. H.; Yu, M. J. Treatment of Taste and Odor Material by Oxidation and Adsorption. *Water Sci. Technol.* **2004**, *49* (9), 289–295.

(14) Jr, C. T.; Mt, B.; Dw, M. Improvement of Thermal Reactivation of Activated Carbon for the Removal of 2-Methylisoborneol. *Water Res* **2007**, *41* (1), 79–86. https://doi.org/10.1016/j.watres.2006.09.010.

(15) Bu, L.; Zhou, S.; Shi, Z.; Deng, L.; Gao, N. Removal of 2-MIB and Geosmin by Electrogenerated Persulfate: Performance, Mechanism and Pathways. *Chemosphere* **2017**, *168*, 1309–1316. https://doi.org/10.1016/j.chemosphere.2016.11.134.

(16) Klausen, C.; Nicolaisen, M. H.; Strobel, B. W.; Warnecke, F.; Nielsen, J. L.; Jørgensen, N. O. G. Abundance of Actinobacteria and Production of Geosmin and 2-Methylisoborneol in Danish Streams and Fish Ponds. *FEMS Microbiol Ecol* **2005**, *52* (2), 265–278. https://doi.org/10.1016/j.femsec.2004.11.015.

(17) Smith, J. L.; Boyer, G. L.; Zimba, P. V. A Review of Cyanobacterial Odorous and Bioactive Metabolites: Impacts and Management Alternatives in Aquaculture. *Aquaculture* **2008**, *280* (1–4), 5–20. https://doi.org/10.1016/j.aquaculture.2008.05.007.

(18) Lee, J.; Rai, P. K.; Jeon, Y. J.; Kim, K.-H.; Kwon, E. E. The Role of Algae and Cyanobacteria in the Production and Release of Odorants in Water. *Environmental Pollution* **2017**, *227*, 252–262. https://doi.org/10.1016/j.envpol.2017.04.058.

(19) Antonopoulou, M.; Evgenidou, E.; Lambropoulou, D.; Konstantinou, I. A Review on Advanced Oxidation Processes for the Removal of Taste and Odor Compounds from Aqueous Media. *Water Research* **2014**, *53*, 215–234. https://doi.org/10.1016/j.watres.2014.01.028.

(20) Andreozzi, R.; Caprio, V.; Insola, A.; Marotta, R. Advanced Oxidation Processes (AOP) for Water Purification and Recovery. *Catalysis today* **1999**, *53* (1), 51–59.

(21) Chiron, S.; Fernandez-Alba, A.; Rodriguez, A.; Garcia-Calvo, E. Pesticide Chemical Oxidation: State-of-the-Art. *Water Research* **2000**, *34* (2), 366–377.

(22) Chen, Y.; Dionysiou, D. D. TiO2 Photocatalytic Films on Stainless Steel: The Role of Degussa P-25 in Modified Sol–Gel Methods. *Applied Catalysis B: Environmental* **2006**, *62* (3–4), 255–264. https://doi.org/10.1016/j.apcatb.2005.07.017.

(23) Choi, H.; Stathatos, E.; Dionysiou, D. D. Sol–Gel Preparation of Mesoporous Photocatalytic TiO_2 Films and TiO_2/Al_2O_3 Composite Membranes for Environmental Applications. *Applied Catalysis B: Environmental* **2006**, *63* (1–2), 60–67. https://doi.org/10.1016/j.apcatb.2005.09.012.

(24) Choi, H.; Stathatos, E.; Dionysiou, D. D. Synthesis of Nanocrystalline Photocatalytic TiO_2 Thin Films and Particles Using Sol–Gel Method Modified with Nonionic Surfactants. *Thin Solid Films* **2006**, *510* (1–2), 107–114. https://doi.org/10.1016/j.tsf.2005.12.217.

(25) Tran, H.; Evans, G. M.; Yan, Y.; Nguyen, A. V. Photocatalytic Removal of Taste and Odour Compounds for Drinking Water Treatment. *Water Science and Technology: Water Supply* **2009**, *9* (5), 477–483.

(26) Pettit, S. L.; Rodriguez-Gonzalez, L.; Michaels, J. T.; Alcantar, N. A.; Ergas, S. J.; Kuhn, J. N. Parameters Influencing the Photocatalytic Degradation of Geosmin and 2-Methylisoborneol Utilizing Immobilized TiO_2. *Catalysis Letters* **2014**, *144* (8), 1460–1465. https://doi.org/10.1007/s10562-014-1281-x.

(27) Baccaro, A. L. B.; Gutz, I. G. R. Quick Cold Preparation of TiO_2 Nanolayers on Gold from P25 Suspensions – Film Structure, Voltammetric Behavior and Photocatalytic Performance for the Oxidation of EDTA under UVA-LED Irradiation. *Electrochimica Acta* **2016**, *214*, 295–306. https://doi.org/10.1016/j.electacta.2016.08.048.

(28) Kelesidis, G. A.; Goudeli, E.; Pratsinis, S. E. Flame Synthesis of Functional Nanostructured Materials and Devices: Surface Growth and Aggregation. *Proceedings of the Combustion Institute* **2017**, *36* (1), 29–50. https://doi.org/10.1016/j.proci.2016.08.078.

(29) Ohno, T.; Sarukawa, K.; Tokieda, K.; Matsumura, M. Morphology of a TiO_2 Photocatalyst (Degussa, P-25) Consisting of Anatase and Rutile Crystalline Phases. *Journal of Catalysis* **2001**, *203* (1), 82–86. https://doi.org/10.1006/jcat.2001.3316.

(30) Jafry, H. R.; Liga, M. V.; Li, Q.; Barron, A. R. Simple Route to Enhanced Photocatalytic Activity of P25 Titanium Dioxide Nanoparticles by Silica Addition. *Environmental Science & Technology* **2011**, *45* (4), 1563–1568. https://doi.org/10.1021/es102749e.

(31) Hurum, D. C.; Agrios, A. G.; Gray, K. A.; Rajh, T.; Thurnauer, M. C. Explaining the Enhanced Photocatalytic Activity of Degussa P25 Mixed-Phase TiO_2 Using EPR. *The Journal of Physical Chemistry B* **2003**, *107* (19), 4545–4549. https://doi.org/10.1021/jp0273934.

(32) Li, F.; Zhao, Y.; Hao, Y.; Wang, X.; Liu, R.; Zhao, D.; Chen, D. N-Doped P25 TiO_2–Amorphous Al_2O_3 Composites: One-Step Solution Combustion Preparation and Enhanced Visible-Light Photocatalytic Activity. *Journal of Hazardous Materials* **2012**, *239–240*, 118–127. https://doi.org/10.1016/j.jhazmat.2012.08.016.

(33) Scanlon, D. O.; Dunnill, C. W.; Buckeridge, J.; Shevlin, S. A.; Logsdail, A. J.; Woodley, S. M.; Catlow, C. R. A.; Powell, Michael. J.; Palgrave, R. G.; Parkin, I. P.; Watson, G. W.; Keal, T. W.; Sherwood, P.; Walsh, A.; Sokol, A. A. Band Alignment of Rutile and Anatase TiO_2. *Nature Materials* **2013**, *12* (9), 798–801. https://doi.org/10.1038/nmat3697.

(34) Skorb, E. V.; Shchukin, D. G.; Möhwald, H.; Sviridov, D. V. Photocatalytically-Active and Photocontrollable Coatings Based on Titania-Loaded Hybrid Sol–Gel

Films. *Journal of Materials Chemistry* **2009**, *19* (28), 4931. https://doi.org/10.1039/b821827g.

(35) Zainudin, N. F.; Abdullah, A. Z.; Mohamed, A. R. Characteristics of Supported Nano-TiO_2/ZSM-5/Silica Gel (SNTZS): Photocatalytic Degradation of Phenol. *Journal of Hazardous Materials* **2010**, *174* (1–3), 299–306. https://doi.org/10.1016/j.jhazmat.2009.09.051.

(36) Li, A.; Jin, Y.; Muggli, D.; Pierce, D. T.; Aranwela, H.; Marasinghe, G. K.; Knutson, T.; Brockman, G.; Zhao, J. X. Nanoscale Effects of Silica Particle Supports on the Formation and Properties of TiO_2 Nanocatalysts. *Nanoscale* **2013**, *5* (13), 5854. https://doi.org/10.1039/c3nr01287e.

(37) Latthe, S.; Liu, S.; Terashima, C.; Nakata, K.; Fujishima, A. Transparent, Adherent, and Photocatalytic SiO_2-TiO_2 Coatings on Polycarbonate for Self-Cleaning Applications. *Coatings* **2014**, *4* (3), 497–507. https://doi.org/10.3390/coatings4030497.

(38) Jiang, Y.; Jin, Z.; Chen, C.; Duan, W.; Liu, B.; Chen, X.; Yang, F.; Guo, J. Cerium-Doped Mesoporous-Assembled SiO_2 /P25 Nanocomposites with Innovative Visible-Light Sensitivity for the Photocatalytic Degradation of Organic Dyes. *RSC Adv.* **2017**, *7* (21), 12856–12870. https://doi.org/10.1039/C7RA00191F.

(39) Kete, M.; Pavlica, E.; Fresno, F.; Bratina, G.; Štangar, U. L. Highly Active Photocatalytic Coatings Prepared by a Low-Temperature Method. *Environmental Science and Pollution Research* **2014**, *21* (19), 11238–11249. https://doi.org/10.1007/s11356-014-3077-3.

(40) Gaidau, C.; Petica, A.; Ignat, M.; Popescu, L. M.; Piticescu, R. M.; Tudor, I. A.; Piticescu, R. R. Preparation of Silica Doped Titania Nanoparticles with Thermal Stability and Photocatalytic Properties and Their Application for Leather Surface Functionalization. *Arabian Journal of Chemistry* **2016**. https://doi.org/10.1016/j.arabjc.2016.09.002.

(41) Hatchard, C. G.; Parker, C. A. A New Sensitive Chemical Actinometer. II. Potassium Ferrioxalate as a Standard Chemical Actinometer. *Proceedings of the Royal Society of London A: Mathematical, Physical and Engineering Sciences* **1956**, *235* (1203), 518–536. https://doi.org/10.1098/rspa.1956.0102.

(42) Stookey, L. L. Ferrozine---a New Spectrophotometric Reagent for Iron. *Anal. Chem.* **1970**, *42* (7), 779–781. https://doi.org/10.1021/ac60289a016.

(43) Saito, K.; Okamura, K.; Kataoka, H. Determination of Musty Odorants, 2-Methylisoborneol and Geosmin, in Environmental Water by Headspace Solid-Phase Microextraction and Gas Chromatography–Mass Spectrometry. *Journal of Chromatography A* **2008**, *1186* (1–2), 434–437. https://doi.org/10.1016/j.chroma.2007.12.078.

(44) Ishibashi, K.; Fujishima, A.; Watanabe, T.; Hashimoto, K. Quantum Yields of Active Oxidative Species Formed on TiO_2 Photocatalyst. *Journal of Photochemistry and Photobiology A: Chemistry* **2000**, *134* (1), 139–142. https://doi.org/10.1016/S1010-6030(00)00264-1.

(45) Zhang, J.; Nosaka, Y. Mechanism of the OH Radical Generation in Photocatalysis with TiO_2 of Different Crystalline Types. *The Journal of Physical Chemistry C* **2014**, *118* (20), 10824–10832. https://doi.org/10.1021/jp501214m.

(46) Yang, Z.-Y.; Shen, G.-Y.; He, Y.-P.; Liu, X.-X.; Yang, S.-J. Preparation of TiO_2/SiO_2 Composite Oxide and Its Photocatalytic Degradation of Rhodamine B. *Journal of Porous Materials* **2016**, *23* (3), 589–599. https://doi.org/10.1007/s10934-015-0114-7.

(47) Koo, M. S.; Cho, K.; Yoon, J.; Choi, W. Photoelectrochemical Degradation of Organic Compounds Coupled with Molecular Hydrogen Generation Using Electrochromic TiO_2 Nanotube Arrays. *Environmental Science & Technology* **2017**, *51* (11), 6590–6598. https://doi.org/10.1021/acs.est.7b00774.

(48) Paint, A. C. D.-1 on; Related Coatings, Materials; Applications. *Standard Test Methods for Measuring Adhesion by Tape Test*; ASTM International, **2009**.

(49) Fotiou, T.; Triantis, T. M.; Kaloudis, T.; Papaconstantinou, E.; Hiskia, A. Photocatalytic Degradation of Water Taste and Odour Compounds in the Presence of Polyoxometalates and TiO_2: Intermediates and Degradation Pathways. *Journal of Photochemistry and Photobiology A: Chemistry* **2014**, *286*, 1–9. https://doi.org/10.1016/j.jphotochem.2014.04.013.

(50) Summerfelt, S. T. Ozonation and UV Irradiation. *Aquac. Eng* **2003**, *28*, 36.

(51) Ennaoui, A.; Sankapal, B. R.; Skryshevsky, V.; Lux-Steiner, M. Ch. TiO_2 and TiO_2–SiO_2 Thin Films and Powders by One-Step Soft-Solution Method: Synthesis and Characterizations. *Solar Energy Materials and Solar Cells* **2006**, *90* (10), 1533–1541. https://doi.org/10.1016/j.solmat.2005.10.019.

(52) Aziz, R. A.; Sopyan, I. Synthesis of TiO_2-SiO_2 Powder and Thin Film Photocatalysts by Sol-Gel Method. *IJC-A Vol.48A(07) [July 2009]* **2009**.

(53) Erdural, B.; Bolukbasi, U.; Karakas, G. Photocatalytic Antibacterial Activity of TiO_2–SiO_2 Thin Films: The Effect of Composition on Cell Adhesion and Antibacterial Activity. *Journal of Photochemistry and Photobiology A: Chemistry* **2014**, *283*, 29–37. https://doi.org/10.1016/j.jphotochem.2014.03.016.

(54) Lawton, L. The Destruction of 2-Methylisoborneol and Geosmin Using Titanium Dioxide Photocatalysis. *Applied Catalysis B: Environmental* **2003**, *44* (1), 9–13. https://doi.org/10.1016/S0926-3373(03)00005-5.

(55) Dijkstra, M. F. J.; Michorius, A.; Buwalda, H.; Panneman, H. J.; Winkelman, J. G. M.; Beenackers, A. A. C. M. Comparison of the Efficiency of Immobilized and Suspended Systems in Photocatalytic Degradation. *Catalysis Today* **2001**, *66* (2–4), 487–494. https://doi.org/10.1016/S0920-5861(01)00257-7.

(56) Andronic, L.; Duta, A. The Influence of TiO_2 Powder and Film on the Photodegradation of Methyl Orange. *Materials Chemistry and Physics* **2008**, *112* (3), 1078–1082. https://doi.org/10.1016/j.matchemphys.2008.06.059.

(57) Ahmed, S.; Rasul, M. G.; Martens, W. N.; Brown, R.; Hashib, M. A. Heterogeneous Photocatalytic Degradation of Phenols in Wastewater: A Review on Current Status and Developments. *Desalination* **2010**, *261* (1–2), 3–18. https://doi.org/10.1016/j.desal.2010.04.062.

(58) Song, W.; Yan, S.; Cooper, W. J.; Dionysiou, D. D.; O'Shea, K. E. Hydroxyl Radical Oxidation of Cylindrospermopsin (Cyanobacterial Toxin) and Its Role in the Photochemical Transformation. *Environmental Science & Technology* **2012**, *46* (22), 12608–12615. https://doi.org/10.1021/es302458h.

(59) Dong, S. Z.; Chen, C. Z.; Li, D. M.; Sun, Y. S. [A study of hygienic standard for titanium in the source of drinking water]. *Zhonghua Yu Fang Yi Xue Za Zhi* **1993**, *27* (1), 26–28.

(60) Mills, A.; Le Hunte, S. An Overview of Semiconductor Photocatalysis. *Journal of photochemistry and photobiology A: Chemistry* **1997**, *108* (1), 1–35.

(61) Li, H.; Zhang, W.; Pan, W. Enhanced Photocatalytic Activity of Electrospun TiO_2 Nanofibers with Optimal Anatase/Rutile Ratio. *Journal of the American Ceramic Society* **2011**, *94* (10), 3184–3187. https://doi.org/10.1111/j.1551-2916.2011.04748.x.

(62) Balasubramanian, G.; Dionysiou, D.; Suidan, M.; Baudin, I.; Laine, J. Evaluating the Activities of Immobilized TiO_2 Powder Films for the Photocatalytic Degradation of Organic Contaminants in Water. *Applied Catalysis B: Environmental* **2004**, *47* (2), 73–84. https://doi.org/10.1016/j.apcatb.2003.04.002.

(63) Bacsa, R. R.; Kiwi, J. Effect of Rutile Phase on the Photocatalytic Properties of Nanocrystalline Titania during the Degradation of P-Coumaric Acid. *Applied Catalysis B: Environmental* **1998**, *16* (1), 19–29.

(64) Bickley, R. I.; Gonzalez-Carreno, T.; Lees, J. S.; Palmisano, L.; Tilley, R. J. A Structural Investigation of Titanium Dioxide Photocatalysts. *Journal of Solid State Chemistry* **1991**, *92* (1), 178–190.

(65) Kawahara, T.; Konishi, Y.; Tada, H.; Tohge, N.; Nishii, J.; Ito, S. A Patterned TiO_2(Anatase)/TiO_2(Rutile) Bilayer-Type Photocatalyst: Effect of the Anatase/Rutile Junction on the Photocatalytic Activity. *Angewandte Chemie* **2002**, *114* (15), 2935–2937. https://doi.org/10.1002/1521-3757(20020802)114:15<2935::AID-ANGE2935>3.0.CO;2-6.

(66) Miyagi, T.; Kamei, M.; Mitsuhashi, T.; Ishigaki, T.; Yamazaki, A. Charge Separation at the Rutile/Anatase Interface: A Dominant Factor of Photocatalytic Activity. *Chemical Physics Letters* **2004**, *390* (4–6), 399–402. https://doi.org/10.1016/j.cplett.2004.04.042.

(67) Nakajima, H.; Mori, T.; Shen, Q.; Toyoda, T. Photoluminescence Study of Mixtures of Anatase and Rutile TiO_2 Nanoparticles: Influence of Charge Transfer between the Nanoparticles on Their Photoluminescence Excitation Bands. *Chemical Physics Letters* **2005**, *409* (1–3), 81–84. https://doi.org/10.1016/j.cplett.2005.04.093.

(68) Šuligoj, A.; Štangar, U. L.; Ristić, A.; Mazaj, M.; Verhovšek, D.; Tušar, N. N. TiO_2–SiO_2 Films from Organic-Free Colloidal TiO_2 Anatase Nanoparticles as Photocatalyst for Removal of Volatile Organic Compounds from Indoor Air. *Applied Catalysis B: Environmental* **2016**, *184*, 119–131. https://doi.org/10.1016/j.apcatb.2015.11.007.

(69) Yu, J.-G.; Yu, H.-G.; Cheng, B.; Zhao, X.-J.; Yu, J. C.; Ho, W.-K. The Effect of Calcination Temperature on the Surface Microstructure and Photocatalytic Activity of TiO_2 Thin Films Prepared by Liquid Phase Deposition. *The Journal of Physical Chemistry B* **2003**, *107* (50), 13871–13879. https://doi.org/10.1021/jp036158y.

(70) Zhou, L.; Yan, S.; Tian, B.; Zhang, J.; Anpo, M. Preparation of TiO_2–SiO_2 Film with High Photocatalytic Activity on PET Substrate. *Materials Letters* **2006**, *60* (3), 396–399. https://doi.org/10.1016/j.matlet.2005.08.065.

(71) Shifu, C.; Gengyu, C. The Effect of Different Preparation Conditions on the Photocatalytic Activity of $TiO_2 \cdot SiO_2$/Beads. *Surface and Coatings Technology* **2006**, *200* (11), 3637–3643. https://doi.org/10.1016/j.surfcoat.2004.11.025.

(72) López, R.; Gómez, R. Band-Gap Energy Estimation from Diffuse Reflectance Measurements on Sol–Gel and Commercial TiO_2: A Comparative Study. *Journal of Sol-Gel Science and Technology* **2012**, *61* (1), 1–7. https://doi.org/10.1007/s10971-011-2582-9.

(73) Bian, J.; Xue, Y.; Yao, K.; Gu, X.; Yan, C.; Wang, Y. Solid-Phase Extraction Approach for Phospholipids Profiling by Titania-Coated Silica Microspheres Prior to Reversed-Phase Liquid Chromatography–Evaporative Light Scattering Detection and Tandem Mass Spectrometry Analysis. *Talanta* **2014**, *123*, 233–240. https://doi.org/10.1016/j.talanta.2014.02.001.

(74) Lin, Y.-L.; Wang, T.-J.; Jin, Y. Surface Characteristics of Hydrous Silica-Coated TiO_2 Particles. *Powder Technology* **2002**, *123* (2–3), 194–198. https://doi.org/10.1016/S0032-5910(01)00470-3.

(75) Anderson, C.; Bard, A. J.; others. An Improved Photocatalyst of TiO_2/SiO_2 Prepared by a Sol-Gel Synthesis. *Journal of Physical Chemistry* **1995**, *99* (24), 9882–9885.

(76) Tian, G.; Fu, H.; Jing, L.; Xin, B.; Pan, K. Preparation and Characterization of Stable Biphase TiO_2 Photocatalyst with High Crystallinity, Large Surface Area,

and Enhanced Photoactivity. *The Journal of Physical Chemistry C* **2008**, *112* (8), 3083–3089. https://doi.org/10.1021/jp710283p.

(77) Luo, X.; Morrin, A.; Killard, A. J.; Smyth, M. R. Application of Nanoparticles in Electrochemical Sensors and Biosensors. *Electroanalysis* **2006**, *18* (4), 319–326. https://doi.org/10.1002/elan.200503415.

(78) Wu, Z.; Dong, F.; Zhao, W.; Wang, H.; Liu, Y.; Guan, B. The Fabrication and Characterization of Novel Carbon Doped TiO_2 Nanotubes, Nanowires and Nanorods with High Visible Light Photocatalytic Activity. *Nanotechnology* **2009**, *20* (23), 235701. https://doi.org/10.1088/0957-4484/20/23/235701.

(79) Exarhos, G. J.; Hess, N. J. Spectroscopic Measurements of Stress Relaxation during Thermally Induced Crystallization of Amorphous Titania Films. *Thin Solid Films* **1992**, *220* (1–2), 254–260.

(80) Balasubramanian, G.; Dionysiou, D. D.; Suidan, M. T.; Subramanian, V.; Baudin, I.; Laîné, J.-M. Titania Powder Modified Sol-Gel Process for Photocatalytic Applications. *Journal of materials science* **2003**, *38* (4), 823–831.

(81) Li, Y.; Bastakoti, B. P.; Imura, M.; Hwang, S. M.; Sun, Z.; Kim, J. H.; Dou, S. X.; Yamauchi, Y. Synthesis of Mesoporous TiO_2 /SiO_2 Hybrid Films as an Efficient Photocatalyst by Polymeric Micelle Assembly. *Chemistry - A European Journal* **2014**, *20* (20), 6027–6032. https://doi.org/10.1002/chem.201304689.

CHAPTER 3 : VISIBLE LIGHT-ACTIVATED CONTROLLABLE SYNTHESIS OF BISMUTH TITANATE PHOTOCATALYSTS FOR ORGANIC POLLUTANT DEGRADATION

3.1. Abstract

Application of titania (TiO_2) in organic pollutant degradation is limited due to its relatively high charge carrier recombination and wide bandgap. As such, TiO_2 is not an effective photocatalyst in the visible range. A novel ternary heterojunction photocatalyst system composed of $TiO_2/Bi_4Ti_3O_{12}/Bi_2O_3$ was developed to extend the activity of the catalyst into the visible range. The non-ionic surfactant Tween-80 was used to obtain crystalline $Bi_4Ti_3O_{12}$ that enhances photocatalytic activity. Catalysts were characterized by X-ray diffraction (XRD), X-ray photoelectron spectroscopy (XPS), diffuse reflectance spectroscopy (DRS), Brunauer Emmett Teller (BET) surface area analysis, and scanning electron microscopy (SEM). Photocatalytic activity efficiency was assessed by the extent of phenol degradation. The most efficient Ti-Bi double-heterostructure developed in this study showed a 55% and a 26% increase in photocatalytic activity compared to anatase TiO_2 and commercial P25-anatase TiO_2 mixture respectively, under visible light illumination. Varying the Tween-80 and Bi concentrations in the sol-gel synthesis process led to variations in the relative concentrations of TiO_2, $Bi_4Ti_3O_{12}$, and Bi_2O_3 heterostructure, allowing activity optimization of the photocatalyst. The enhanced activity of the photocatalyst system was attributed to the narrow bandgap, and low recombination of the photogenerated holes and electrons brought about by its heterostructure.

3.2. Introduction

Among different wastewater and drinking water treatment techniques, semiconductor photocatalyst-based advanced oxidation methods show the ability to efficiently degrade organic pollutants into nonhazardous substances[1,2]. Advanced oxidation processes involving TiO_2 photocatalysts have been extensively studied after the discovery of titania's photoelectrochemical activity since 1972[3]. Due to its non-toxic nature, low cost, stability, and higher activity in the UV range, TiO_2 is considered an effective material to decompose organic pollutants[3–5]. However, TiO_2 application in water and wastewater treatment is limited and becomes uneconomical due to its low absorption of visible light due to its wide bandgap and poor charge carrier separation ability[6]. To overcome these drawbacks, the incorporation of TiO_2 with other semiconductors has become a desirable approach. Making such composite photocatalysts with narrow bandgap materials enhances visible light absorption. Composite photocatalysts also increase the photo-induced carrier separation, reducing hole-electron recombination and thus making electrons and holes available for photocatalytic reactions[7]. As an alternative to TiO_2 alone, bismuth (Bi)-based titania semiconductor composite materials have recently gained interest for the efficient degradation of organic pollutants. Bi-based oxides have a valence band consisting of hybrid orbitals of O 2p and Bi 6s, while the TiO_2 valence band is composed only of O 2p orbitals. Due to the well dispersed Bi 6s orbitals, increased mobility of electric charges and a bandgap decrease have been observed[8,9].

In the area of Bi-based photocatalysis, bismuth-titanates, such as $Bi_{12}TiO_{20}$[10,11] $Bi_2Ti_2O_7$[12,13], $Bi_{20}TiO_{32}$[14,15], and $Bi_4Ti_3O_{12}$[16–18] have been promising candidates that can perform under visible light with a lower rate of recombination. $Bi_4Ti_3O_{12}$ is a ferroelectric

material with optical memory and piezoelectric properties and electro-optic applications[16]. It has been found that the presence of $Bi_4Ti_3O_{12}$ efficiently suppresses the photogenerated electron-hole recombination, thereby increasing the photocatalytic activity[19]. $Bi_4Ti_3O_{12}$ crystalline structure is constructed by triple layers of TiO_6 octahedra $(Bi_2Ti_3O_{10})^{2-}$ (perovskite slab) and one layer of $(Bi_2O_2)^{2+}$ alternate stacking along the c axis. Studies on bond angles have found that the closer the metal-oxygen-metal bond angle to 180°, the more delocalized the excitation energy [20,21]. In $Bi_4Ti_3O_{12,}$ the Ti-O-Ti bond angle was found to be close to 180° that might lead to the efficient movement of electron-hole pairs. The separation of holes and electrons is also induced due to the intra-electric field between $(Bi_2O_2)^{2+}$ and $[(Bi_2Ti_3O_{10})^{2-}]$ [16]. However, it has been reported that synthesizing pure $Bi_4Ti_3O_{12}$ catalysts with higher crystallinity is challenging[22]. Ferroelectric materials such as $Bi_4Ti_3O_{12}$ have relatively low photocurrent densities that can be a disadvantage for photocatalytic activities[23,24]. As a solution to this, compositing $Bi_4Ti_3O_{12}$ with TiO_2 is a proven method to increase the photocurrent. Composite materials that have heterojunctions between two or more photocatalysts in this way inhibit the recombination of photogenerated electrons and holes effectively[23].

Besides bismuth-titanate composites, Bi_2O_3 is considered as an important semiconductor with a bandgap of around 2.80 eV that can easily be excited with visible light illumination[25]. Furthermore, apart from its narrow bandgap, Bi_2O_3 has several desirable qualities such as thermal stability, nontoxicity, and corrosion resistance for its use in organic pollutant degradation[26]. The main disadvantage of Bi_2O_3, however, is its higher recombination rate of photogenerated charge carriers[27–29].

In recent years, semiconductor composites consisting of three photocatalysts that make ternary heterojunctions/double-heterostructure have been considered for photocatalytic applications due to their enhanced lifetime of charge carriers. Among these ternary systems, $TiO_2/Bi_2O_3/V_2O_5$[30], graphitic $C_3N_4/TiO_2/Bi_2O_3$[31], $TiO_2/SiO_2/Bi_2O_3$[32], $TiO_2/BT/MoS_2$[33], $NiO/Bi_2O_3/Bi_3ClO_4$[29], $BT/Bi_2O_3/Bi_{12}TiO_{20}$[26], $C_3N_4/BT/Bi_4O_5I_2$[34] **,** and $Bi_2O_3/BT/TiO_2$[35] , where BT is $Bi_4Ti_3O_{12}$, have been used.

. Surfactant-assisted nano photocatalyst synthesis has shown an improvement in the physicochemical properties of photocatalysts[36]. During the preparation of photocatalysts, surfactants induce an ordered porous structure and large surface area, thereby improving the photocatalytic efficiency[37–39]. Tween 80 is a non-ionic amphiphilic surfactant with a hydrophilic polar head composed of a sorbitan ring structure and a hydrophobic oleic acid nonpolar tail[40] (Figure 3.1). Self-assembly of Tween 80 in a sol-gel synthesis route plays an important role in achieving homogeneous and ordered nanoparticles[41]. Tween-80 acts as a steric stabilizer, wetting, and capping agent and thereby controls the nucleation and growth of nanoparticles[42,43].

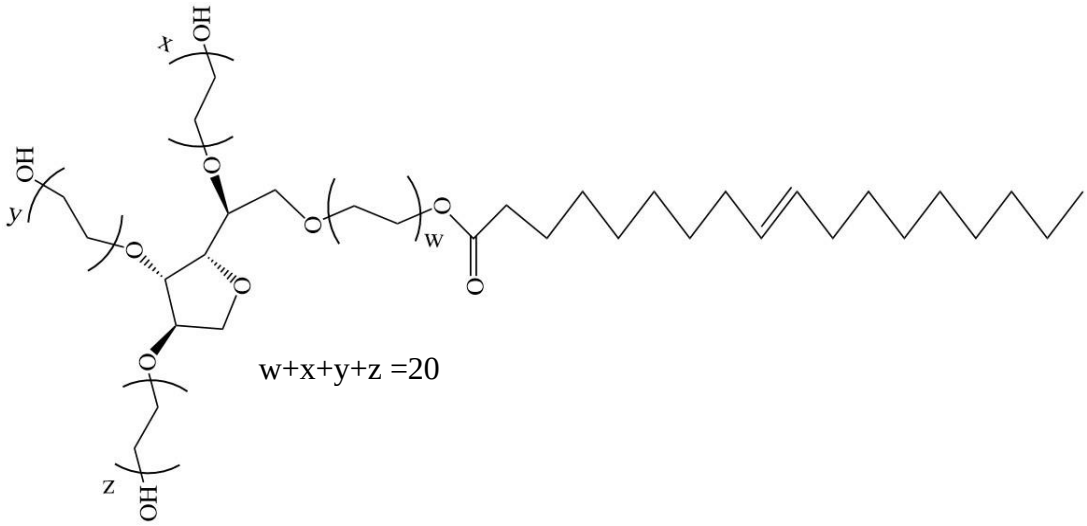

Figure 3.1. Molecular structure of the Tween-80

Karunakaran et al. have synthesized Bi_2O_3-TiO_2 photocatalytic nanocomposite using the sol-gel approach[44]. Tween-80, polyvinyl pyrrolidone-polyethylene glycol(PVP-PEG) were used as templating agents for Bi_2O_3-TiO_2 nanocomposites. This study revealed that in the composites TiO_2 and Bi_2O_3 exist in anatase and β form, respectively[44]. Longxiang et al. have used Span-80 (Sorbitan monooleate) and Tween-80 to synthesize $Bi_{3.25}La_{0.75}Ti_3O_{12}$[45]. Along with the spherical lanthanum bismuth titanate, $Bi_2Ti_2O_7$ and $Bi_4Ti_3O_{12}$ crystalline phases were also observed upon changing the calcination temperature from 450°C to550°C[45]. To the best of our knowledge, no studies have been done on the synthesis of the $Bi_2O_3/Bi_4Ti_3O_{12}/TiO_2$ heterostructure controlled by the concentration of the non-ionic surfactant Tween-80.

Based on the above considerations, in this work, we developed a novel technique to synthesize a double heterostructured photocatalytic system containing a $Bi_2O_3/Bi_4Ti_3O_{12}/TiO_2$ mixture for photocatalytic degradation of organic pollutants under visible light illumination. In our approach, we synthesize efficient photocatalysts by varying the non-ionic surfactant, Tween-80, and Bi concentrations. By incorporating the non-ionic surfactant Tween-80, the photocatalysts' crystalline phases were controlled without changing other parameters, such as calcination temperature and reactant concentrations.

3.3. Experimental

3.3.1. Preparation of Bi-incorporated titanate composites

Titanium tetraisopropoxide (TTIP, 97%; Sigma Aldrich), P25 TiO_2 powder (Evonik, formerly Degussa), polyoxyethylene sorbitan monooleate surfactant (Tween-80, 99.999%; Sigma Aldrich), and bismuth nitrate pentahydrate ($Bi(NO_3)_3.5H_2O$, 98%; Sigma Aldrich) were used in the synthesis Bi-incorporated Ti composites. According to the composition of TTIP, Tween-80, and $Bi(NO_3)_3.5H_2O$, two types of bismuth-titanate photocatalysts were synthesized in this study: (a) Catalysts synthesized at a constant Ti:Bi molar ratio of 1:0.5 and varying the Tween-80:Ti molar ratio (0:1, 0.5:1, 1:1, and 2:1); and (b) Catalysts synthesized at a Tween-80:Ti molar ratio of 2:1 and varying the Ti:Bi molar ratio (1:0, 1:0.25, and 1:1). The chemical composition of the initial sol-gel mixture and the labeling scheme of each catalyst are summarized in Table 3.1.

Table 3.1. Catalyst labeling scheme and corresponding Ti:Bi and Tween-80:Ti molar ratios

Catalyst	**Ti:Bi molar ratio**	**Tween-80:Ti molar ratio**
$B_{0.5}$T-0	1:0.5	No Tween 80
$B_{0.5}$T-0.5	1:0.5	0.5:1
$B_{0.5}$T-1	1:0.5	1:1
$B_{0.5}$T-2	1:0.5	2:1
$B_{0.25}$T-2	1:0.25	2:1
B_1T-2	1:1	2:1
T-2	No Bi	2:1
PT-1	No Bi	1:1
PBT-1	1:0.5	1:1

The catalysts were synthesized by adding an aliquot (e.g., 8.58 g for 1:1 Tween-80:Ti molar ratio) of Tween-80 to 20 mL of 2-propanol (iPrOH, 99.99%; Sigma Aldrich) solution and stirring until a homogenous solution was produced. Then an aliquot of TTIP (e.g., 3.15 mL for 1:1 Tween-80: Ti molar ratio) was added to the mixture to obtain the desired Tween-80:Ti molar ratio, and the solution was stirred for 1 h. To the resulting solution, $Bi(NO_3)_3.5H_2O$(e.g., 5.19 g for 1:1 Ti:Bi molar ratio) was added under stirring to obtain the desired Bi:Ti molar ratio in the sol mixture. Subsequently, 2 mL of HNO_3 (Fisher Scientific, ACS Reagent Grade, 70%) was added to the mixture dropwise. The final mixture was sonicated for 10 min and stirred for 12 h at room temperature. The P25 powder-enriched Bi-incorporated catalyst (PBT-1) was prepared by adding 0.30 g of P25 to the sol mixture with a Tween-80:Ti molar ratio = 1:1. The final sol mixture was dried at 300 °C for 3 h followed by calcination at 450 °C for 6 h at a heating rate of 3 °C min^{-1}. As controls, catalysts without Tween-80 ($B_{0.5}$T-0), without Bi (T-2), and with P25 but without Bi (PT-1) were prepared using the same procedure.

3.3.2. Catalyst characterization

X-ray diffraction (XRD) patterns of catalyst films were obtained on a Panalytical X'pert MRD X-ray diffraction system using Cu-Kα radiation source (λ_k =1.5406 Å) at a scan rate of 0.3° s^{-1}. X-ray photoelectron spectroscopy (XPS) was performed on a dual anode VG Microtech X-ray source and a SPECS HSA2000 analyzer. XPS data were analyzed using CasaXPS software. UV-Visible diffuse reflectance spectra (DRS) were collected on solid samples at room temperature. The light source was a Mikropack DH-2000 deuterium and halogen light source coupled with an Ocean Optics USB4000 detector. The scattered light was collected with a fiber optic cable. Spectra were referenced to MgO

powder. Data were processed using Spectra Suite 1.4.2 09. Nitrogen adsorption/desorption isotherms were measured using Micromeritics ASAP 2020. The catalyst powder samples (about 0.10 g) were first evacuated at 120 °C for 10 h. An adsorption/desorption isotherm curve was collected at 77 K and at relative pressures of N_2 from P/P0 < 0.01 to 0.996, where P0 is the saturation pressure. The Brunauer Emmett Teller (BET(N_2)) surface areas were calculated using the adsorption branch of the N_2 sorption isotherm. The elemental composition of the photocatalysts was obtained by digesting 0.01 g of the sample in a solution containing 45 mL of concentrated H_2SO_4 (ACS reagent, 95-98%) and 15 mL of H_2O_2 (Certified ACS,30% w/v) and analyzing using an Inductively Coupled Plasma-Atomic Emission Spectrometer (ICP-AES; TJA Model iCAP 6000). Scanning electron microscopy (SEM) was performed on a Zeiss N vision 40 system.

3.3.3. Photocatalytic degradation of phenol

Photodegradation experiments were conducted in a 250 mL quartz beaker in the presence of a 200 mL solution of 10^{-4} M phenol (99%+ Sigma Aldrich) in deionized water (DI, 18 MΩ cm). The experiments started by adding 0.04 g of catalyst powder to the phenol solution and allowing it to equilibrate in the dark for 1 h. The suspension was then placed in the UV chamber (Rayonet, Southern New England Ultraviolet Company, Branford, CT, USA), and illuminated with 16 lamps (Rayonet RPR-4190A), each emitting monochromatic light at 420 nm for 180 min. During the irradiation, 0.5 mL aliquots of solution were withdrawn at six different time intervals (0, 30, 60, 120, and 180 min) to analyze the phenol concentration. Phenol concentration was determined by measuring the absorbance peak area at 269 nm using a UV-Vis spectrometer (Varian Cary-100 Bio).

3.4. Results and discussion

3.4.1. Photocatalyst characterization

3.4.1.1. Ti and Bi concentrations in catalysts

The total Ti and Bi concentrations and molar ratios in each catalyst determined by ICP-AES, and the corresponding Ti: Bi molar ratios are shown in Table 3.2. The catalysts synthesized starting with a Ti: Bi ratio of 2:1 have measured Ti: Bi ratios ranging from 2.1:1 to 2.7:1. When Ti: Bi ratio is changed to 1:1 in the B_2T-2 catalyst, the Ti: Bi ratio is 1.2:1. In the catalyst $B_{0.25}$T-2 that has a lower Bi concentration, the Ti:Bi ratio increases to 3.9:1. These results indicate that the synthesis process incorporates a similar percentage of Bi compared to Ti in the final product.

Table 3.2. Ti:Bi molar ratio of the catalysts after calcination obtained from ICP-AES

Catalyst	**Ti (mg/L)**	**Bi (mg/L)**	**Ti:Bi ratio (molar ratio)**
PBT-1	1.25	2.38	2.3
$B_{0.5}$T-0	2.22	4.06	2.4
$B_{0.5}$T-0.5	1.69	3.41	2.1
$B_{0.5}$T-1	1.95	3.17	2.7
$B_{0.25}$T-2	1.39.	1.53	3.9
$B_{0.5}$T-2	1.64	3.09	2.3
B_1T-2	0.77	2.78	1.2

3.4.1.2. XRD analysis

X-Ray Diffraction patterns obtained for different catalysts are shown in Figure 3.2 P25-enriched TiO_2 powder (PT-1) shows XRD peaks characteristic of both anatase and rutile crystalline phases (International Centre for Diffraction Data; Powder diffraction files ICCD, PDF 01-080-6402)[46]. Diffraction peaks at 2θ = 25.04°, 37.50°, 47.74°, and 54.93° are attributed to anatase crystal planes and those at 2θ = 27.21°, 35.83°, and 53.75° to rutile[46]. The catalyst synthesized without any surfactant ($B_{0.5}$T-0) exhibited a weak peak at 2θ = 27.90° that can be assigned to the major peak for Bi_2O_3, which shows the comparable value for alpha and gamma Bi_2O_3[47–51]. Peaks responsible for bismuth titanate or anatase could not be detected due to the low intensity of those peaks. Tween-80 incorporation in the synthesis of $B_{0.5}$T-0.5, $B_{0.5}$T-1, and $B_{0.5}$T-2 catalysts leads to XRD peaks representing a higher amount of anatase and bismuth-titanate mixed oxide phases ($Bi_4Ti_3O_{12}$) relative to Bi_2O_3 than in the $B_{0.5}$T-0 catalyst. Peaks assigned to $Bi_4Ti_3O_{12}$ appear at 21.40°, 23.37°, 30.06°, 32.87°, 39.76°, 47.20°, and 57.05° are identified and confirmed according to the Crystallography Open Database (COD-2020.12.16)[52,53] and are present in all BT catalysts synthesized with Tween-80. The presence of P25 in the PBT catalyst (PBT-1) also results in peaks for anatase and rutile, in addition to those for $Bi_4Ti_3O_{12}$.

Figure 3.2. also shows the XRD patterns of the catalysts synthesized by varying the Bi concentration but keeping the Ti and Tween-80 concentrations constant ($B_{0.25}$T-2, $B_{0.5}$T-2, B_1T-2; Table 3.1).

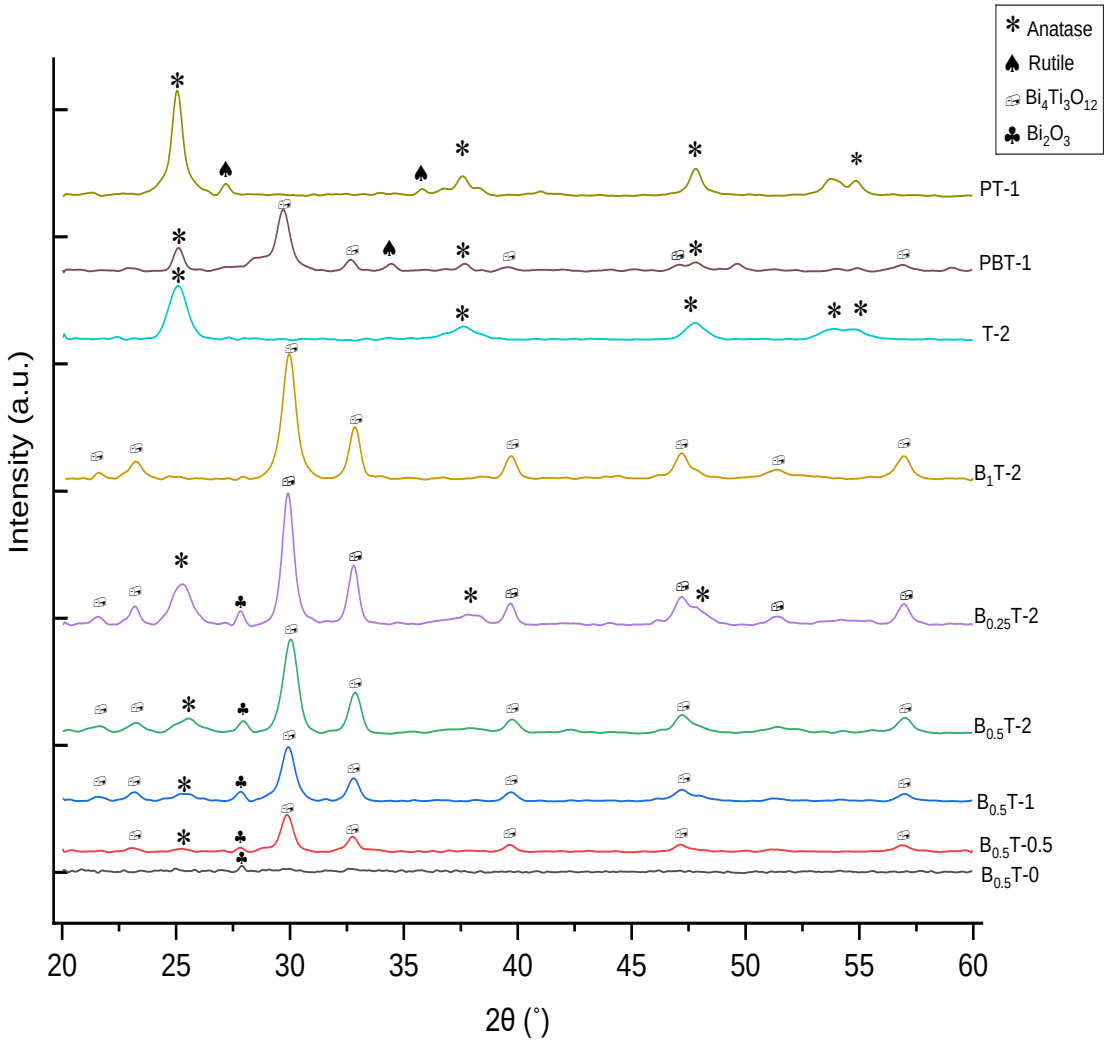

Figure 3.2. X-Ray Diffractograms of the catalysts

These catalysts show characteristic peaks for anatase, $Bi_4Ti_3O_{12}$, and Bi_2O_3. However, an increase in the Bi concentration results in a decrease in the intensities of Bi_2O_3 and anatase peaks relative to the $Bi_4Ti_3O_{12}$ peaks in the order $B_{0.25}$T-2 > $B_{0.5}$T-2 > B_1T-2. Figure 3.3 shows the areas of the most intense peaks for anatase (101) and $Bi_4Ti_3O_{12}$ (171) crystalline phases for the $B_{0.25}$T-2 and $B_{0.5}$T-2 catalysts.

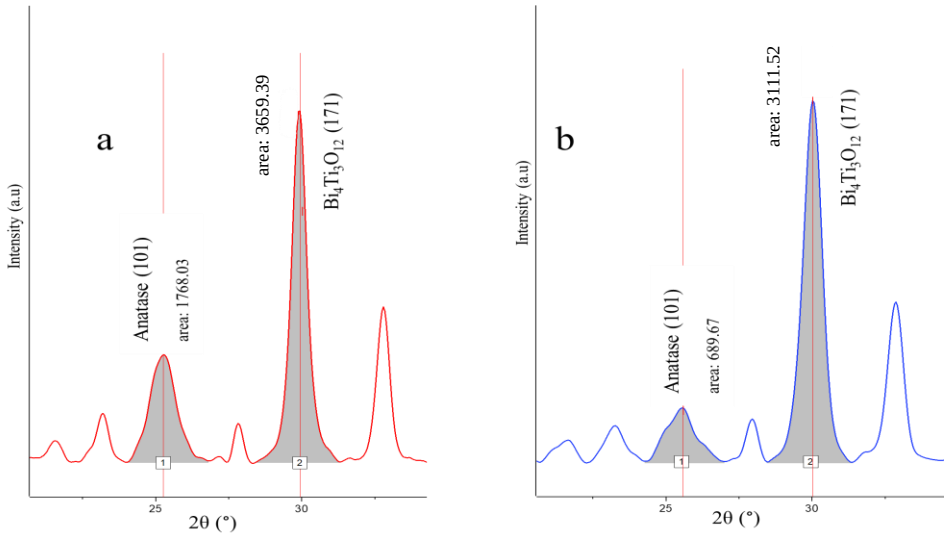

Figure 3.3. Anatase (101) and $Bi_4Ti_3O_{12}$ (171) peak area obtained from XRD for (a) $B_{0.25}$T-2 and (b) $B_{0.5}$T-2 catalysts

The anatase: $Bi_4Ti_3O_{12}$ peak area ratios for $B_{0.25}$T-2 and $B_{0.5}$T-2 are 1:2 and 1:4.5, respectively, indicating that an increase in the Bi concentration and a decrease in the anatase concentration, which suggests that more Ti is incorporated into the $Bi_4Ti_3O_{12}$ network. At a higher Bi concentration of the B_1T-2 catalyst, only $Bi_4Ti_3O_{12}$ peaks are observed. Peaks due to anatase and Bi_2O_3 are not detected. The crystallite size measurement for $Bi_4Ti_3O_{12}$ for the B_xT-2 (x=0.25, 0.5, 1) catalysts was carried out using the Scherrer equation, $D = k\lambda / (\beta \cos\theta)$, where D is the crystallite size, k is a constant (0.94 for spherical particles), λ is the wavelength of the X-ray radiation (1.54 Å), β is the line width at half maximum (FWHM), and 2θ is the angle of diffraction[54]. The average crystallite sizes obtained from XRD were 14.1(±0.48), 11.0(±1.14), and 12.3(±1.03) nm for the $B_{0.25}$T-2, $B_{0.5}$T-2, and B_1T-2 catalysts, respectively.

According to the crystalline phase relative peak areas obtained from the XRD patterns (Anatase (101), Bi_2O_3, and $Bi_4Ti_3O_{12}$ (171)), the composition of the catalyst with respect to the percentage of three different crystalline phases can be shown in a ternary phase diagram as follows (Figure 3.4).

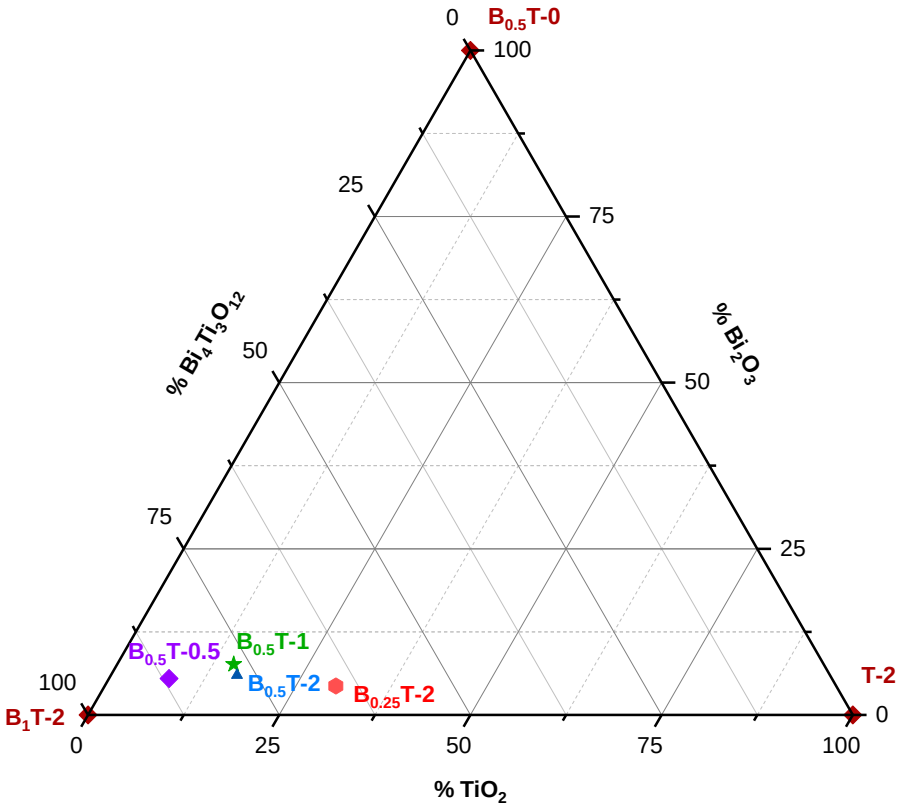

Figure 3.4. Ternary phase diagram for the percentages of Bi_2O_3, TiO_2, and $Bi_4Ti_3O_{12}$ in the photocatalysts determined by XRD

3.4.1.3. X-ray photoelectron spectroscopy

The surface chemical composition and elemental oxidation states of the catalysts were investigated by XPS. Figures 3.5-3.10 show the XPS spectra of bismuth titanate catalysts, PT, and PBT catalysts.

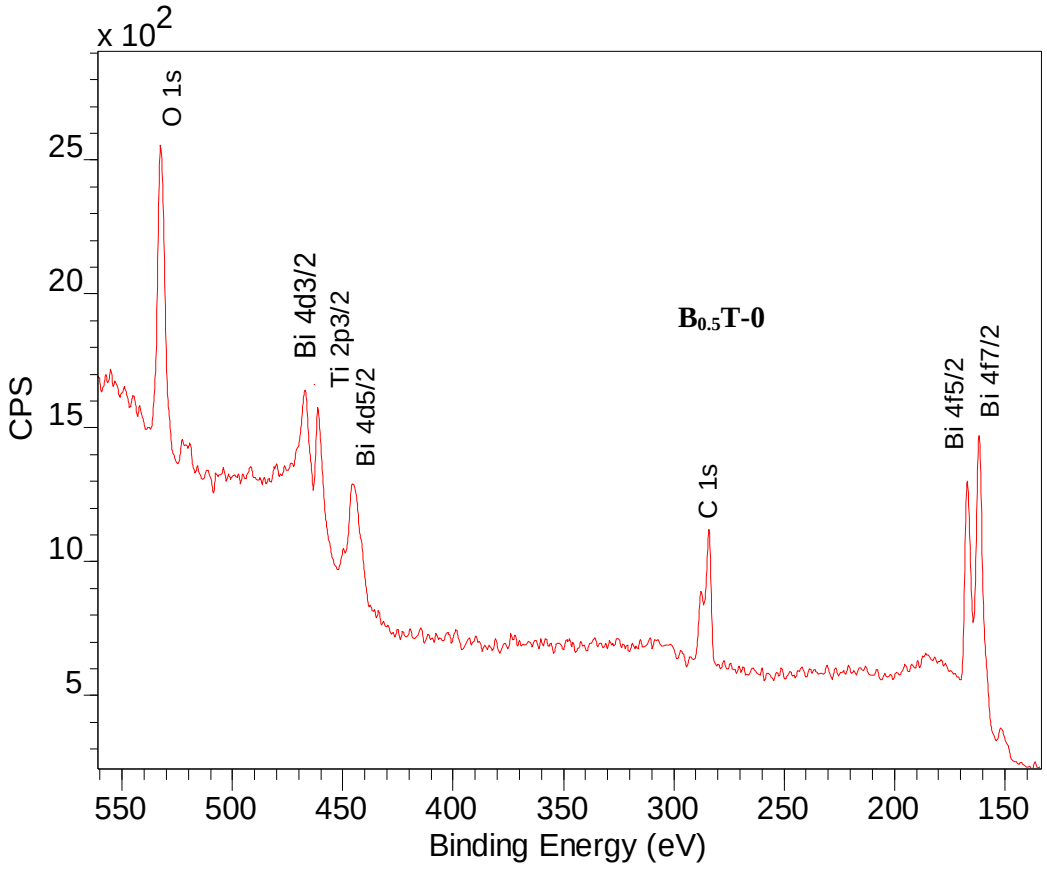

Figure 3.5. XPS spectra of catalyst $B_{0.5}T$-0

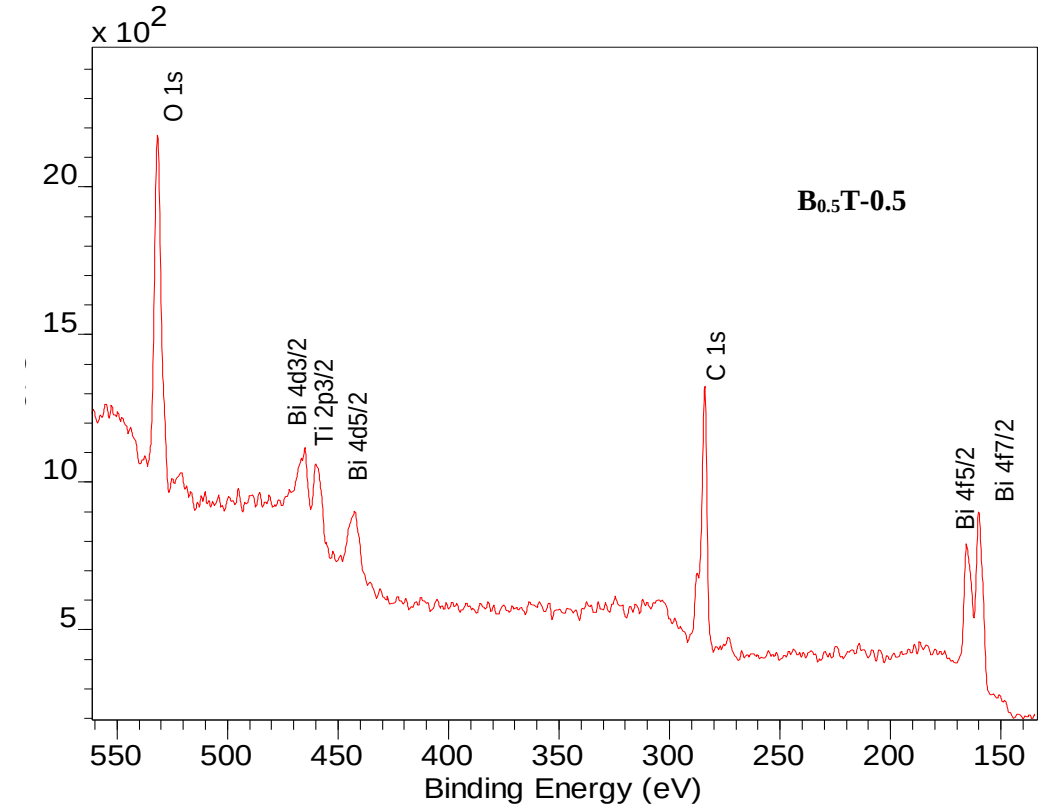

Figure 3.6. XPS spectra of catalyst $B_{0.5}T$-0.5

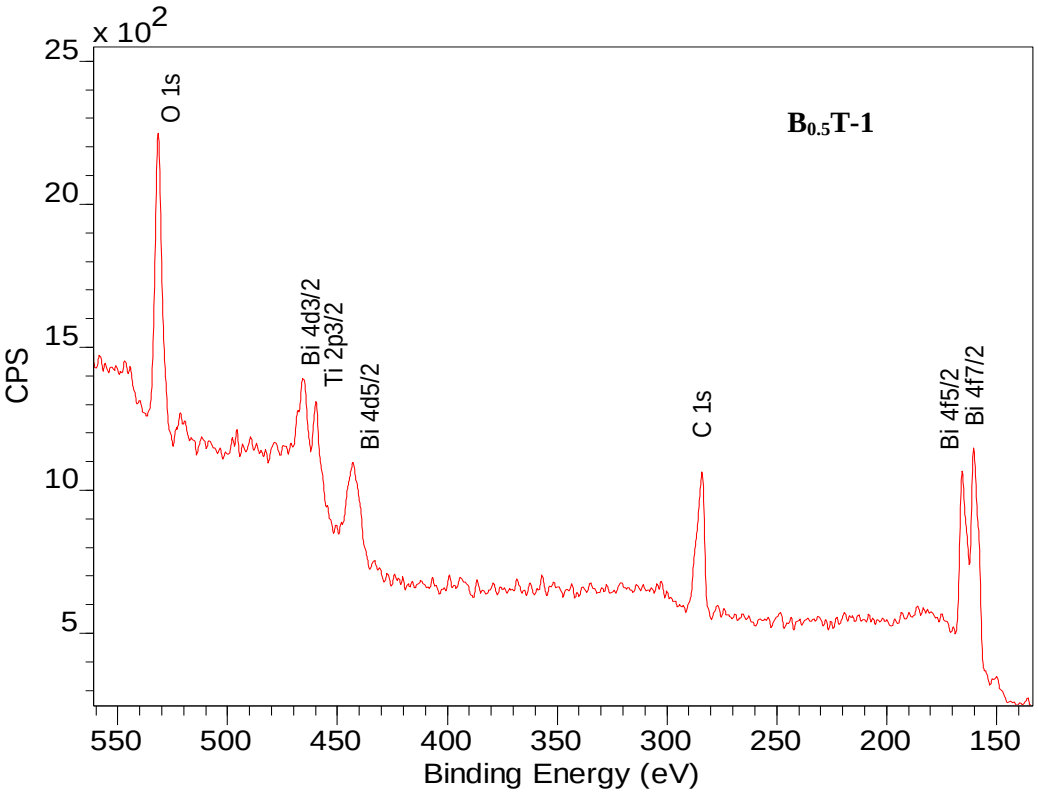

Figure 3.7. XPS spectra of catalyst $B_{0.5}T$-1

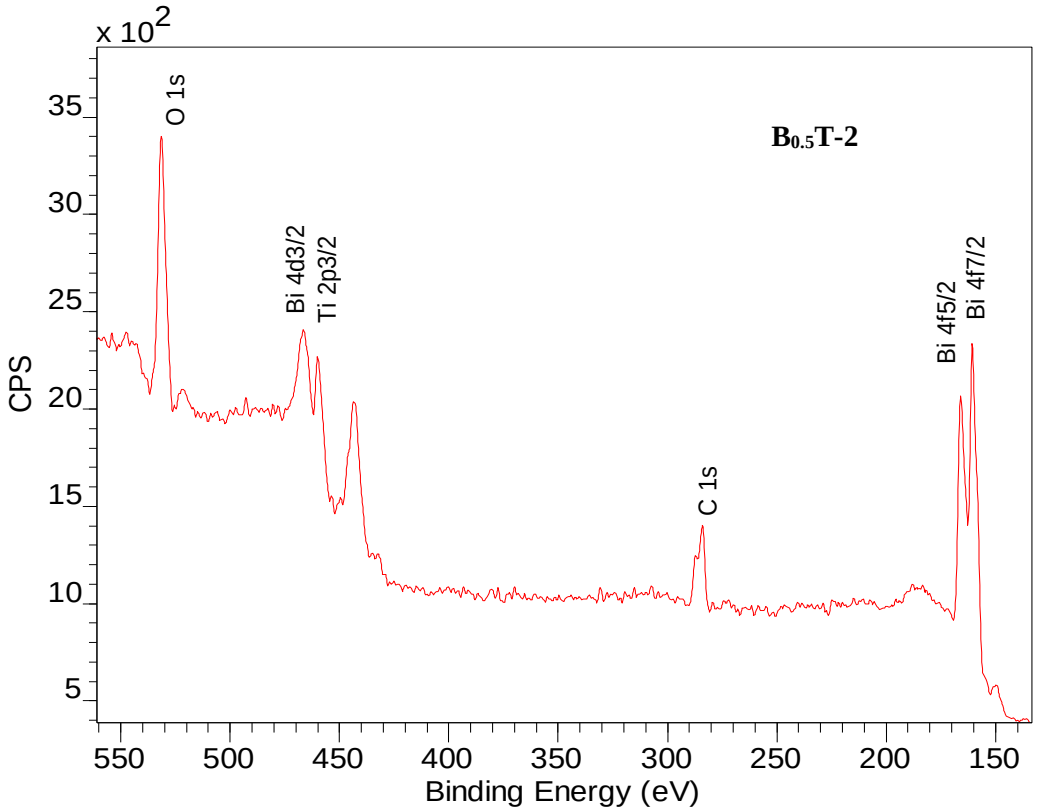

Figure 3.8. XPS spectra of catalyst $B_{0.5}T$-2

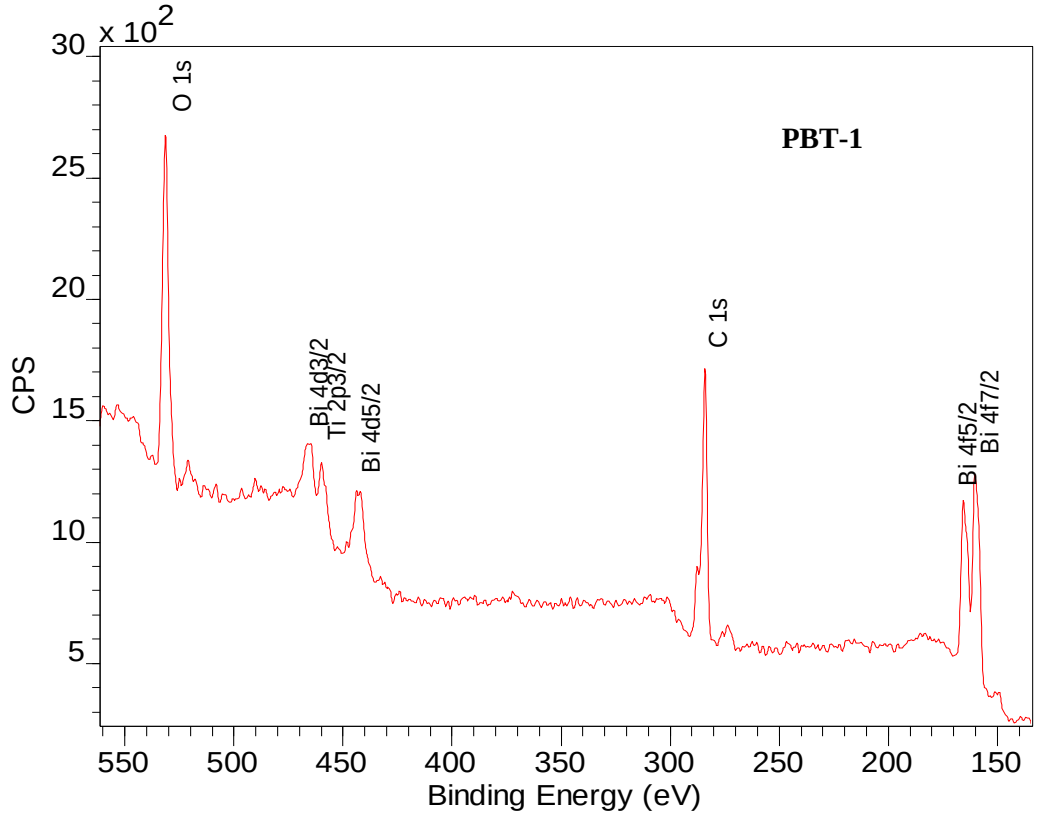

Figure 3.9. XPS spectra of catalyst PBT-1

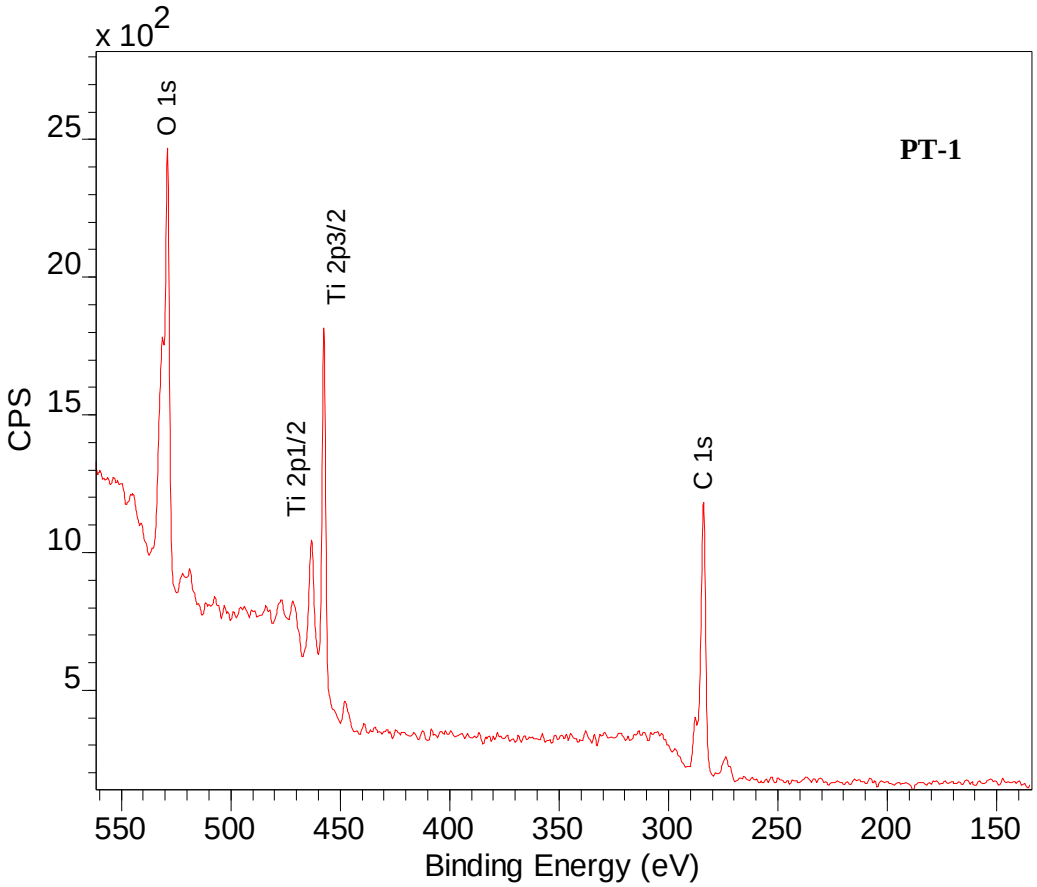

Figure 3.10. XPS spectra of catalyst PT-1

The C 1*s* peak at 284 eV is derived from the adventitious carbon used to calibrate the binding energy scale of the XPS data. The spectra show peaks corresponding to the photoemission of Bi 4*f*, Bi 4*d*, Ti 2*p*, and O 1*s* core levels. Two sharp peaks at the lower binding energy region can be assigned to Bi $4f_{5/2}$ and Bi $4f_{7/2}$ levels[55]. In all these catalysts, the binding energies of Bi $4f_{5/2}$ and Bi $4f_{7/2}$ show a positive shift than previously reported values for bare Bi_2O_3 (166.4 eV -161.0 eV)[55] and $Bi_4Ti_3O_{12}$ (164.5 eV-159.2 eV)[18]. This positive shift is likely due to partial oxidation of Bi^{3+} centers to $Bi^{(3+\delta+)}$[56], which indicates a strong interaction between Bi and TiO_2 due to the formation of Bi-O-Ti bonds[57]. For the $B_{0.5}T$-0 catalyst, the Bi $4f_{5/2}$ and $4f_{7/2}$ doublet occurred at 166.9 and 161.8 eV, respectively. These values are comparable to the previously reported range of 167.2-161.8

eV, suggesting the existence of Bi_2O_3-TiO_2 interaction in the $B_{0.5}$T-0 catalyst [55]. Compared to $B_{0.5}$T-0, catalysts synthesized using Tween-80 ($B_{0.5}$T-0.5, $B_{0.5}$T-1, and $B_{0.5}$T-2, and PBT-1) showed less shift (compared to 166.9 and 161.8 eV) of the Bi 4*f* doublet. For instance, the binding energies for Bi $4f_{5/2}$ and $4f_{7/2}$ doublet for B_1T-2 is centered at 160.6 eV and 165.9 eV, respectively. Less shift in the Bi $4f_{5/2}$ and $4f_{7/2}$ doublet for $B_{0.5}$T-2 compared to $B_{0.5}$T-0 can be considered as an indication of the existence of (+3-δ) valence state of Bi in $Bi_4Ti_3O_{12}$ that is produced due to the oxygen deficiency and an increase in oxygen vacancies near the Bi cations in $[Bi_2O_2]^{2+}$ or $[Bi_2Ti_3O_{10}]^{2-}$ layers[58].

The XPS spectra of Ti 2*p* for the Bi-containing catalysts can be resolved into two peaks that can be assigned to Ti $2p_{1/2}$, Ti $2p_{3/2}$, and these overlap with the Bi $4d_{3/2}$ peak leading to one broad band centered at 467.0 - 465.0 eV. Binding energy values of $2p_{3/2}$ for each catalyst are given in Table 3.3. An example of peak fitting for one catalyst ($B_{0.5}$T-2) is shown in Figure 3.11. The binding energies of $2p_{3/2}$ peaks of Bi-containing catalysts showed a higher value and broader peaks than that of catalysts without Bi (PT-1 and T-2), as shown in Table 3.3. This shift towards a higher binding energy can be ascribed to the decreasing electron density around the Ti^{4+} due to Bi^{3+} ions[59]. This further confirms the Ti-O-Bi interaction of all of the Bi-containing catalysts. Peak broadening can also be attributed to the formation of the Ti-O-Bi network, and surface defects[60]. Figure 3.10 shows peaks assigned to Ti $2p_{1/2}$ and Ti $2p_{3/2}$ photoemissions of PT-1 catalyst at 463.2 and 457.6 eV, respectively, with a typical energy gap of 5.7 eV that is characteristic of Ti^{4+} [51]. Moreover, Bi-containing catalysts show a single asymmetric peak for the O 1s region at above 530.0 eV, indicating that there is more than one chemical state which confirms Bi-O and Ti-O bonds [58,61].

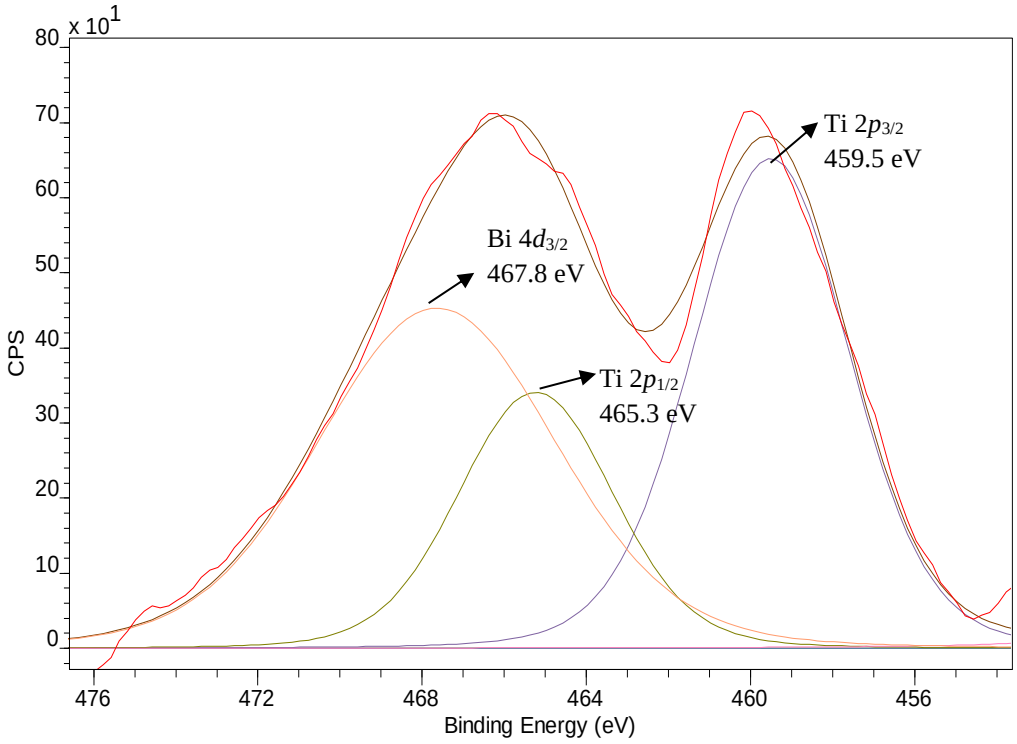

Figure 3.11. Gaussian peak fitting of XPS spectra of Ti 2p and Bi 4d3/2 region ($B_{0.5}$T-2 catalyst)

Table 3.3. Ti 2p3/2 binding energy values

Catalyst	**Ti 2p3/2 (eV)**
PT-1	457.6
$B_{0.5}$T-0	461.4
$B_{0.5}$T-0.5	460.1
$B_{0.5}$T-1	459.8
$B_{0.5}$T-2	460.1
PBT-1	459.8

3.4.1.4. UV-Vis diffuse reflectance measurements

The UV-Vis diffuse reflectance measurements were performed to determine the bandgap energy (E_g) of the catalysts. Figure 3.12 and 3.13 show the modified Kubelka-Munk function, $(F(R)\ h\nu)^2$, versus the bandgap energy (eV) for the different catalysts, where h is the Planck constant and ν is the frequency. An exponent of 2 in the Kubelka-Munk function was used considering the direct transition band gap[62,63]. F(R) was determined by transforming the reflectance (R) spectra of the samples. The bandgap values were obtained by extrapolating the linear part of the curve to $(F(R)\ h\nu)^2 = 0$. The catalyst $B_{0.5}T$-0 (Figure 3.12) shows a direct bandgap = 2.87 eV, which is comparable to previously reported Bi_2O_3 band gap values[64]. Previous studies on pure anatase and $Bi_4Ti_3O_{12}$ show higher bandgap values than Bi_2O_3[65,66]. With the formation of more $Bi_4Ti_3O_{12,}$ bandgaps of $B_{0.5}T$-0.5, $B_{0.5}T$-1, and $B_{0.5}T$-2 catalysts (Figure 3.12) increased to 3.02, 3.11, and 3.18 eV, respectively. This increase in the bandgap can be attributed to the formation of more $Bi_4Ti_3O_{12}$ that was observed in several other studies as well[67]. Also, $B_{0.5}T$-0.5, $B_{0.5}T$-1, and $B_{0.5}T$-2 catalysts show slightly lower bandgap values than pure $Bi_4Ti_3O_{12}$ reported in other studies (3.20 eV)[68–70]. This decrease in bandgap is likely due to the interaction between narrow bandgap $Bi_4Ti_3O_{12}$ with TiO_2 heterojuncntion[61].

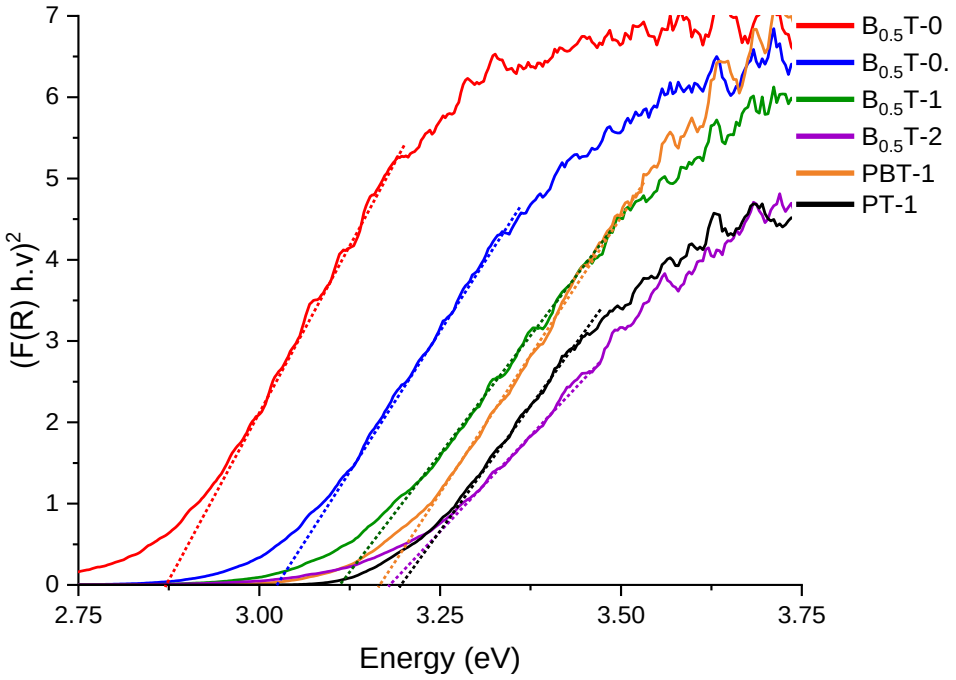

Figure 3.12. Modified Kubelka-Munk vs. energy plots; catalysts synthesized using Ti:Bi (molar) =1:0.5 and varying Tween-80:Ti (molar) (0, 0.5, 1 and 2)

UV-Vis DRS for the catalysts synthesized with varying amounts of bismuth and the same amount of Tween-80 are shown in Figure 3.13. The T-2 catalyst shows a bandgap energy of 3.27 eV (Figure 3.13), which is a closer value to the reported band gap of anatase (3.26 eV)[71]. The bandgap energy of 3.25 eV for B_1T-2 (Figure 3.13) is within the range (3.20 eV- 3.29 eV) of the reported values for $Bi_4Ti_3O_{12}$[68–70]. In our study, the higher value of the Bi_1Ti-2 bandgap (compared to other Bi-incorporated catalysts) can be attributed to decrease in the amount of anatase and Bi_2O_3, relative to $Bi_4Ti_3O_{12}$ (Figure 3.2 and 3.3). Also smaller crystallite size 12.3 (±1.03) lead to increase the bandgap value of Bi_1Ti-2 catalyst compared to the other Bi-containing catalysts shown in Figure 3.13. This change can be attributed to the quantum confinement effect[72]. When the particle size decreases at the nanoscale, the number of overlapping energy levels decreases, and band energy

becomes discrete. This causes a rise in the bandgap between the valence band and conduction band[73]. A lower bandgap energy of 3.15 eV was observed for the $Bi_{0.25}$Ti-2 (Figure 3.13) catalyst than those of the $Bi_{0.5}$Ti-2 and Bi_1Ti-2 catalysts. This lower value can be attributed to two major factors identified from the XRD analysis. 1. Larger crystallite size of the $Bi_4Ti_3O_{12}$ species in $Bi_{0.25}$Ti-2 (14.1(±0.48) nm) than $Bi_{0.5}$Ti-2 (11.0(±1.14) nm), and Bi_1Ti-2 (12.3(±1.03) nm) 2. The coexistence of three crystalline phases (TiO_2, Bi_2O_3, and $Bi_4Ti_3O_{12}$) in this catalyst leading to a double heterostructure arrangement.

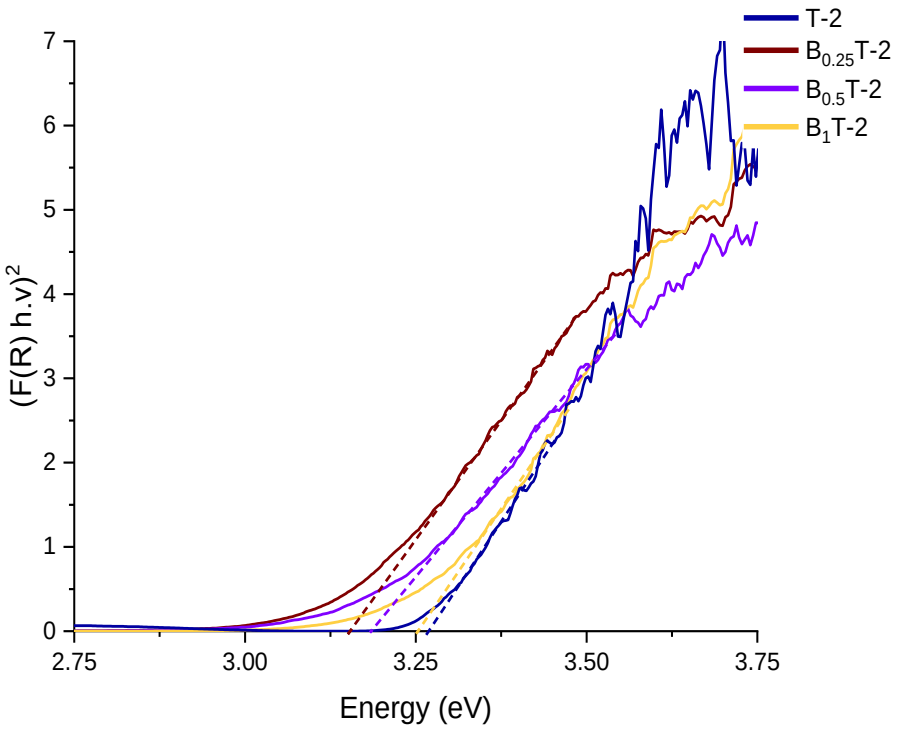

Figure 3.13. Modified Kubelka-Munk vs. energy plots; catalysts synthesized varying Ti:Bi (molar) and using same amount of Tween 80 (Tween 80:Ti=2)

3.4.1.5. BET surface area

Specific surface areas, pore sizes, and pore volumes of the photocatalysts calculated by the BET and BJH methods are summarized in Table 3.4. Figure 3.14-3.22 shows the N_2 adsorption-desorption isotherms of each catalyst. All samples exhibit type (IV) isotherms with a hysteresis loop according to the IUPAC classification, indicating that they have a mesoporous structure[74]. Pore size distribution was evaluated by considering the desorption branch of the isotherms. In the desorption branch of the isotherm for the $B_{0.5}$T-0 catalyst (Figure 3.14), pore size is uniform (~5 nm diameter) compared to those in the $B_{0.5}$T-0.5, $B_{0.5}$T-1, and $B_{0.5}$T-2 catalysts. This uniform pore size distribution in $B_{0.5}$T-0 is likely due to the presence of only Bi_2O_3 in this catalyst.

Table 3.4. Structural characteristics of the catalysts

Catalyst	**BET surface area (m^2/g)**	**Pore volume (Single point adsorption total) (cm^3/g)**	**BJH_{ads} pore diameter (nm)**	**BJH_{desorp} pore diameter (nm)**
PT-1	87.60	0.167	8.10	7.45
PBT-1	42.04	0.227	23.21	18.86
$B_{0.5}$T-0	83.26	0.118	6.11	5.33
$B_{0.5}$T-0.5	66.59	0.128	8.38	7.62
$B_{0.5}$T-1	61.85	0.162	11.34	9.90
$B_{0.25}$T-2	50.94	0.116	9.39	8.04
$B_{0.5}$T-2	56.80	0.144	10.86	9.94
B_1T-2	26.48	0.159	24.94	18.77
T-2	89.91	0.111	5.49	5.07

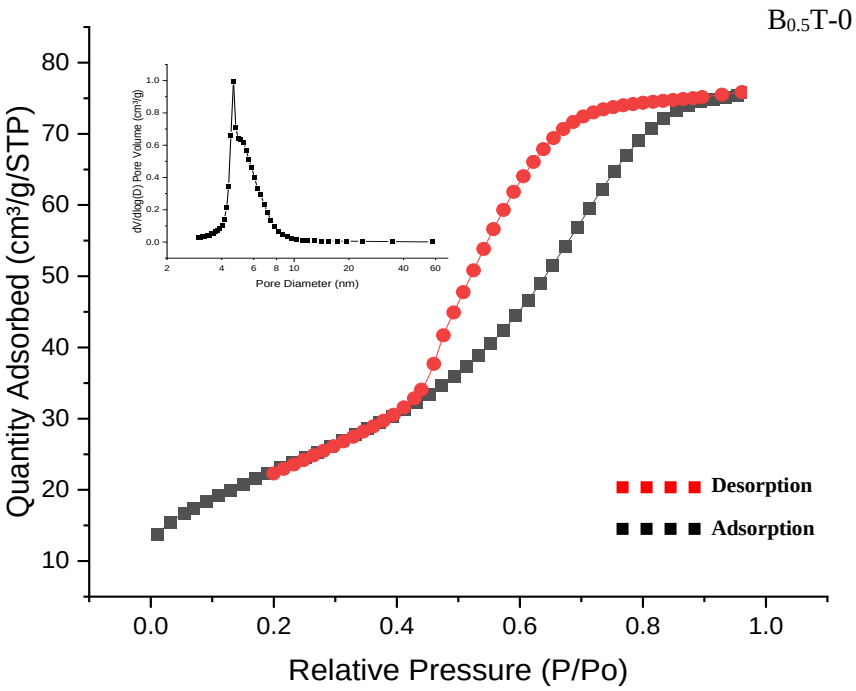

Figure 3.14. N_2 adsorption-desorption isotherms and corresponding pore size of $B_{0.5}T$-0

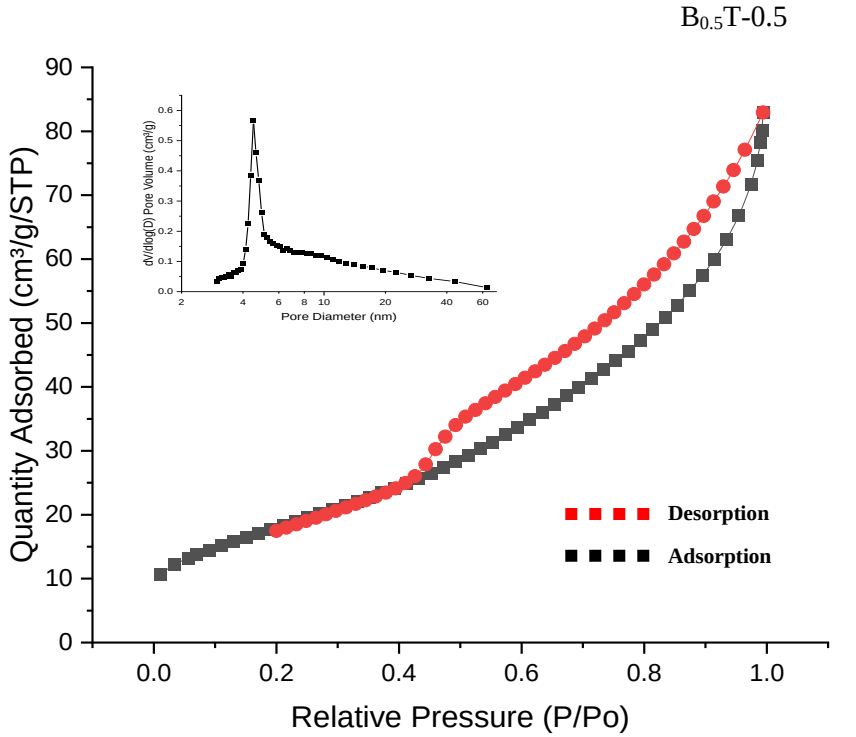

Figure 3.15. N_2 adsorption-desorption isotherms and corresponding pore size $B_{0.5}T$-0.5

The emergence of porous structures with pore size diameter in the ~5-10 nm range is observed in the $B_{0.5}T$-0.5 catalyst (Figure 3.15). This pattern extends and becomes more noticeable for the $B_{0.5}T$-1 and $B_{0.5}T$-2 catalysts that show an increase in pore size diameter > 5 nm due to the presence of the TiO_2 and $Bi_4Ti_3O_{12}$ species (Figure 3.16 and Figure 3.17).

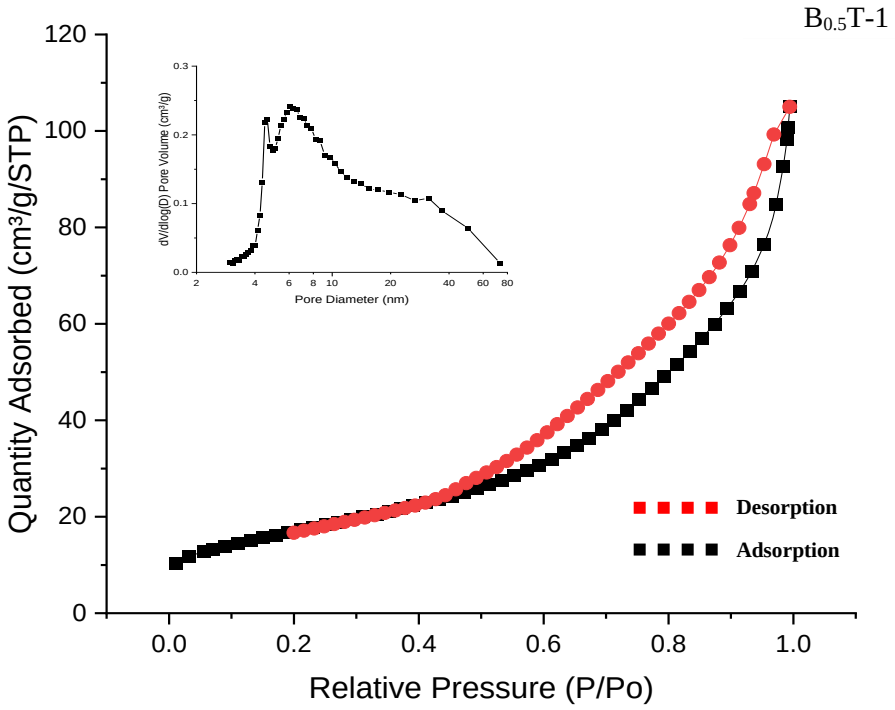

Figure 3.16. N_2 adsorption-desorption isotherms and corresponding pore size $B_{0.5}T$-1

Pore distribution becomes less monodisperse for the catalysts synthesized with varying amounts of Bi but the same amount of Tween-80 ($B_{0.5}T$-2, $B_{0.25}T$-2, B_1T-2; Figure 3.17, 3.18 and 3.19). This can be attributed to the presence of different species in the catalysts (i.e.,Bi_2O_3, anatase, and $Bi_4Ti_3O_{12}$). According to XRD analysis, ratios of major peaks for anatase to $Bi_4Ti_3O_{12}$ increased in the order of 1:2,1:4.5 and 1:44 for $B_{0.25}T$-2, and $B_{0.5}T$-2

catalysts, respectively. With the increase of $Bi_4Ti_3O_{12}$, a decrease in Bi_2O_3, anatase species was also observed.

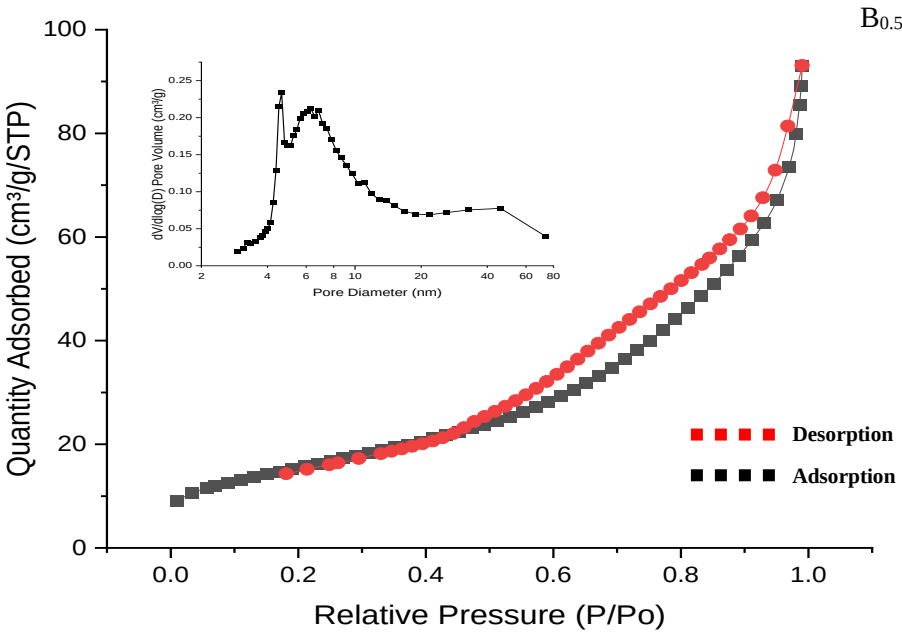

Figure 3.17. N_2 adsorption-desorption isotherms and corresponding pore size distribution of the catalysts $B_{0.5}T$-2

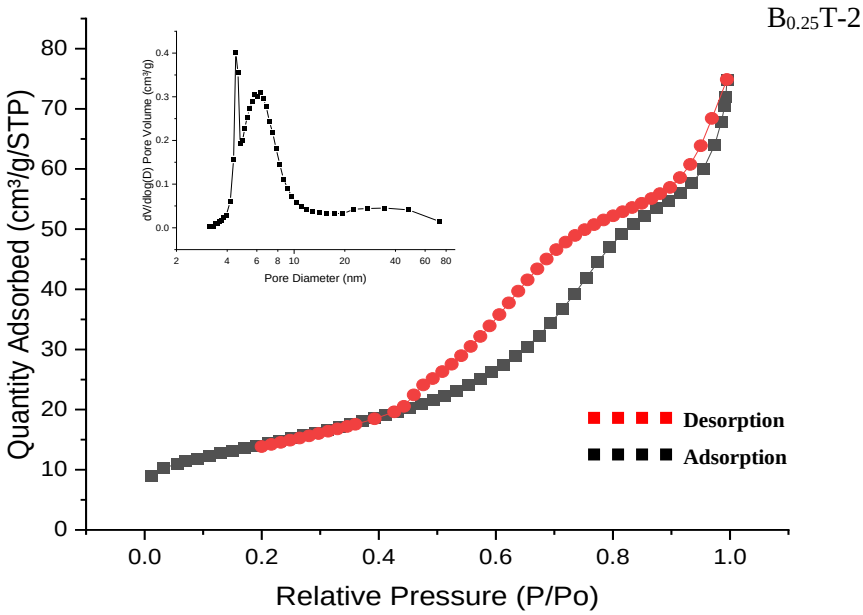

Figure 3.18. N_2 adsorption-desorption isotherms and corresponding pore size distribution of the catalysts $B_{0.25}T$-2

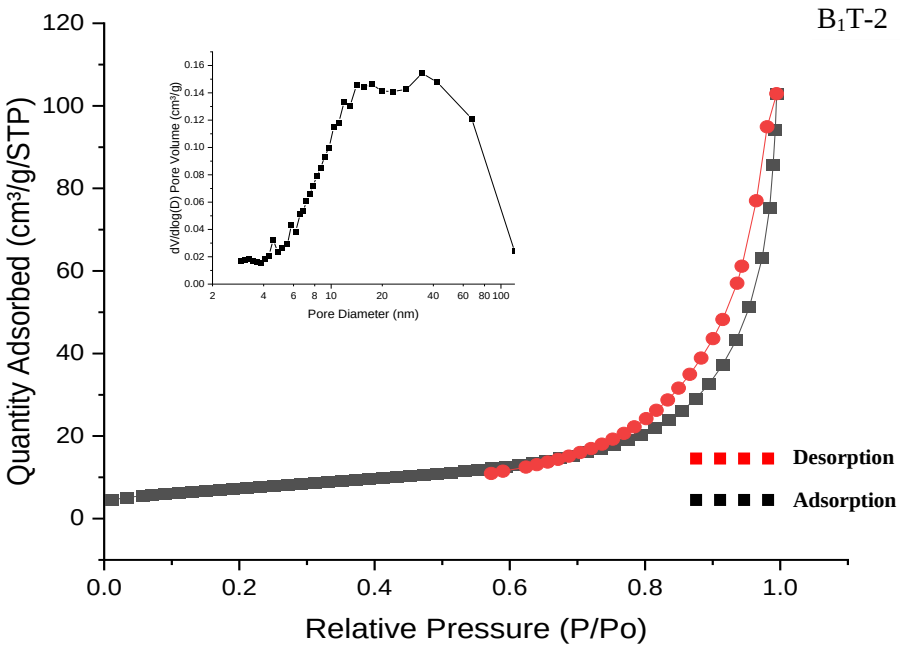

Figure 3.19. N_2 adsorption-desorption isotherms and corresponding pore size distribution of the catalysts B_1T-2

The PT-1 catalyst shows two types of pores due to TiO_2 (~5 nm) and P25 (~15 nm), while the T-2 catalyst only shows pore distribution of ~5 nm (Figure 3.20 and 3.21). The PBT-1 catalyst shows a wide distribution of pore sizes from 5 to 60 nm, which can be attributed to the presence of the $Bi_4Ti_3O_{12}$ and P25 (Figure 3.22).

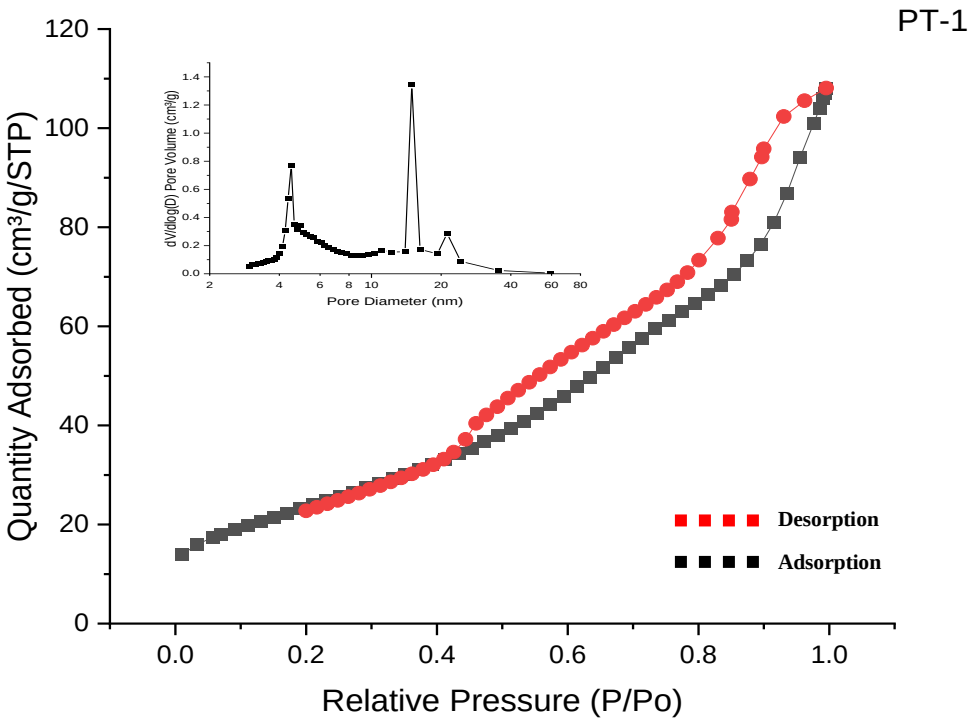

Figure 3.20. N_2 adsorption-desorption isotherms and corresponding pore size distribution of PT-1

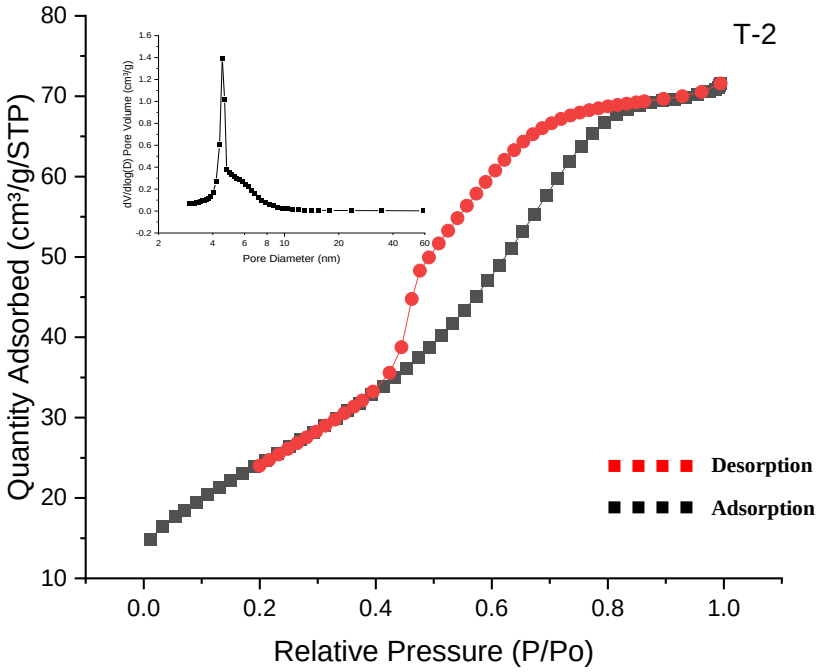

Figure 3.21. N_2 adsorption-desorption isotherms and corresponding pore size distribution of T-2

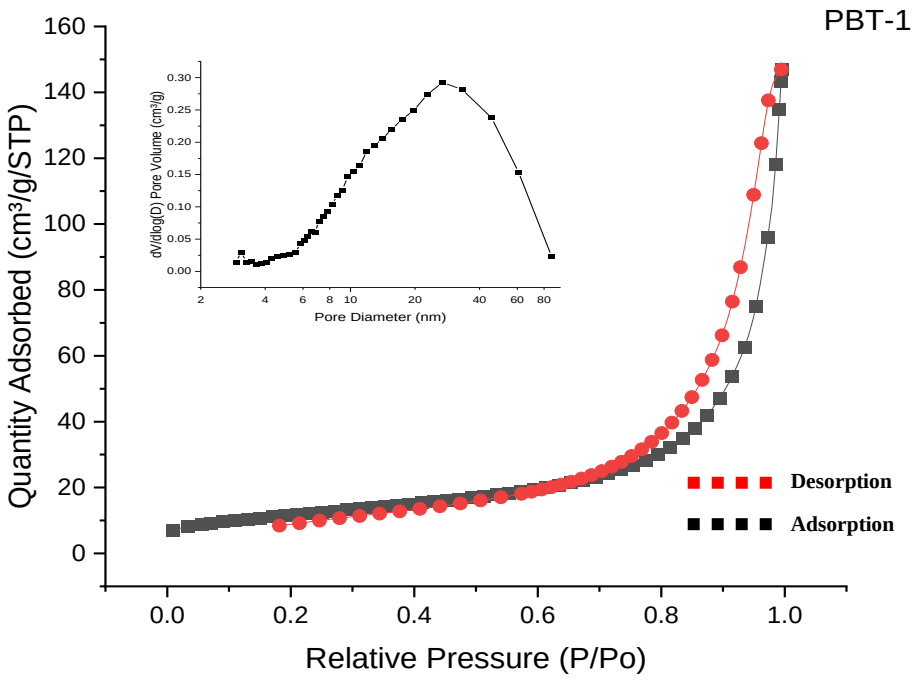

Figure 3.22. N_2 adsorption-desorption isotherms and corresponding pore size distribution of the catalysts PBT-1

A decrease in the surface area was observed with an increase in the Tween-80 concentration (i.e., $B_{0.5}T$-0 > $B_{0.5}T$-0.5 > $B_{0.5}T$-1 > $B_{0.5}T$-2). Pore diameters and volumes, however, increased with an increase in Tween-80 concentration. Therefore, the formation of more $Bi_4Ti_3O_{12}$ with increasing Tween-80 concentration in the sol-gel results in a smaller BET surface area but a larger pore size. The reported surface area of mesoporous $Bi_4Ti_3O_{12}$ species at 53.6 m^2g^{-1} is within the range of surface areas measured in this study.[75]

3.4.1.6. Scanning electron microscopy

The SEM micrographs (Figure 3.23) show that particle size decreases with an increasing surfactant concentration in the catalysts. More uniform distribution and less particle aggregation are observed by increasing the Tween-80:Ti molar ratio from 0 to 2 in the initial mixture. These observations can be attributed to the role played by the Tween-80 in making a stable sol that facilitates interparticle repulsion and prevents aggregation[76].

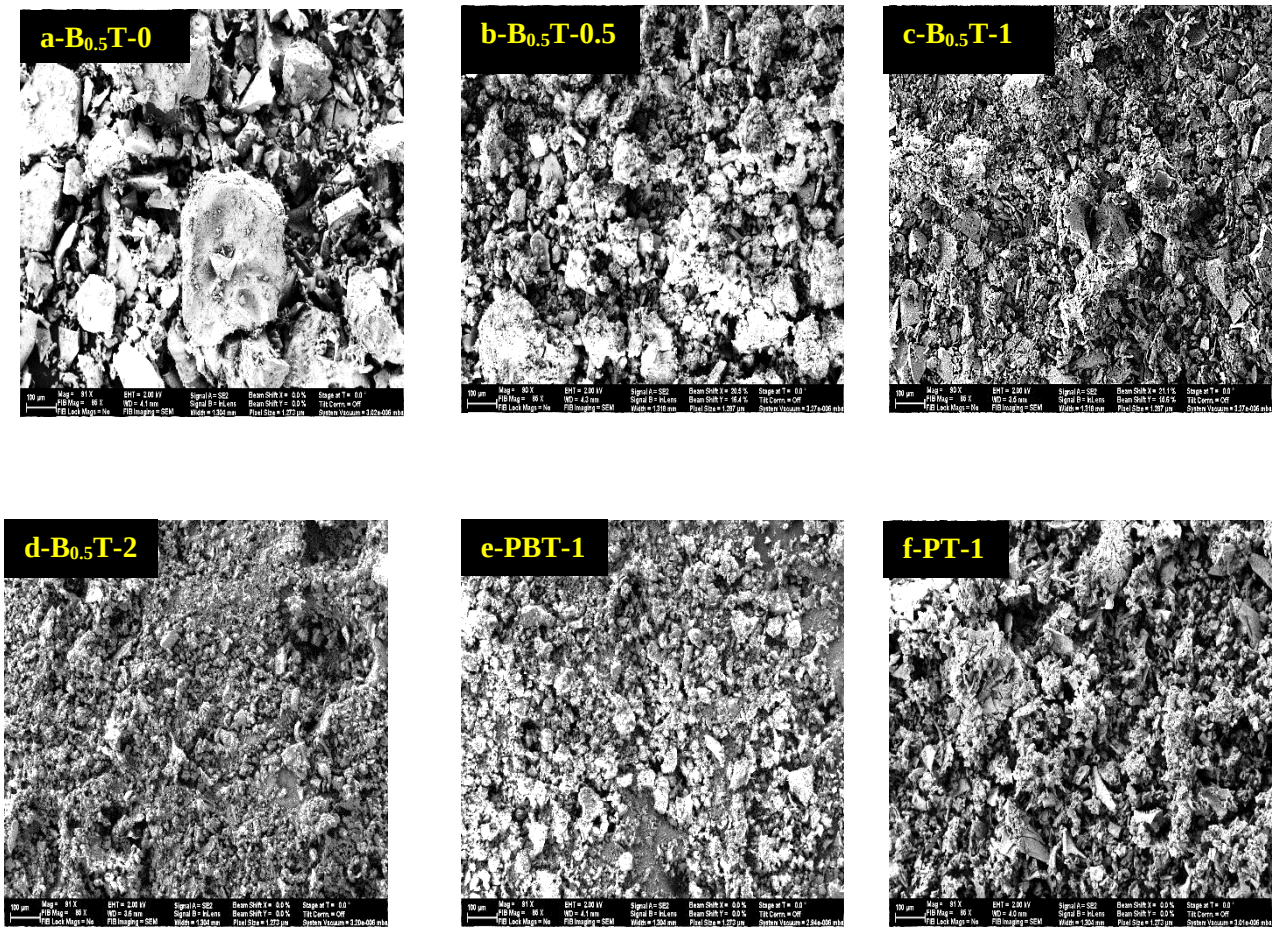

Figure 3.23. The SEM micrographs of the photocatalyst of the catalysts (a: $B_{0.5}$T-0, b: $B_{0.5}$T-0.5, c: $B_{0.5}$T-1, d: $B_{0.5}$T-2, e: PBT-1, f: PT-1)

3.4.2. Effect of the surfactant on the catalyst formation

Based on the above characterization results, it can be seen that the phase transformation, and fraction of each crystalline phase (Bi_2O_3, $Bi_4Ti_3O_{12}$, and TiO_2) are affected by the surfactant concentration. The catalysts $B_{0.5}T$-0, $B_{0.5}T$-0.5, $B_{0.5}T$-1, and $B_{0.5}T$-2 that contain the same Ti:Bi molar ratio of 1:0.5 had different amounts of Bi_2O_3, $Bi_4Ti_3O_{12}$, and TiO_2 (Figure 3.2). This can be attributed to the presence of different concentrations of the surfactant in these catalysts. The addition of surfactants during the nanoparticle growth process has been shown to control the crystallinity of nanoparticles[77,78]. Specifically, the $B_{0.5}T$-0 catalyst showed only Bi_2O_3 and no detectable amounts of anatase TiO_2 or $Bi_4Ti_3O_{12}$ that is due to the absence of the surfactant during the synthesis process (Figure 3.2). The adsorption of the uniformly ordered structure of the surfactant on the metal oxide can greatly decrease the particle growth rate, causing decreased aggregation and increased crystallinity[65]. Therefore, in this work appearance of crystalline phases of $Bi_4Ti_3O_{12}$ and TiO_2 was observed when increasing the surfactant concentration.

The sol-gel method used for the preparation of TiO_2 in this study involves highly reactive TTIP, which is rapidly hydrolyzed and condensed to form a Ti-O-Ti network. It was observed that the presence of surfactants could significantly reduce the hydrolyzation and condensation reactions due to the capping effect of surfactants around the titania precursor[79–81]. The small micelle size and rigidity resulted from the addition of surfactant can limit the aggregation of the nanoparticles during the sol-gel process[82]. A previous report on $BiVO_4$ formation has found that reaction between Bi^{3+} (in the $Bi(NO_3)_3$ precursor) and VO_3^- is partly inhibited by the surfactant polyethylene glycol[83]. A similar phenomenon

can affect the Bi precursor in the process of condensation into Bi_2O_3 nanoparticles. Bi^{3+} in the Bi precursor solution can adsorb to the surfactant's hydrophilic parts, leading to a decrease in the condensation reaction rate, and inhibiting the formation of the Bi-O-Bi network. Considering the surfactant effect as mentioned above, it can be hypothesized that the addition of Tween-80 inhibits the initial rapid formation of Ti-O-Ti and Bi-O-Bi networks. This leads to the formation of $Bi_4Ti_3O_{12}$ phase that, following an increase in Tween-80 concentration, results in its higher fraction in the catalyst.

3.4.3. Photocatalytic degradation of phenol

Figure 3.24 shows the photodegradation of phenol at 420 nm with time in the presence of different catalysts synthesized with a Ti:Bi molar ratio of 1:0.5 and different Tween-80 concentrations. The apparent pseudo first-order rate constants (k_{app}) for phenol photodegradation are reported in Table 3.5. At 420 nm irradiation, without any catalyst, no phenol was degraded, indicating that radiation alone at this wavelength is not effective in degrading phenol. Phenol concentration decreased by ~18% and ~24% in the presence of PT-1 and $B_{0.5}$T-0 catalysts (both synthesized without Tween-80), respectively, within 3 hr.

The catalysts that were synthesized using Tween-80, however, enhanced the photocatalytic activity. The catalysts with the lowest ($B_{0.5}$T-0.5) and the highest ($B_{0.5}$T-2) Tween-80 concentrations increased the photocatalytic activity by ~10% and ~16%, respectively, compared to $B_{0.5}$T-0. This lower activity of the $B_{0.5}$T-0 can be ascribed to its low degree of crystallinity and the presence of Bi_2O_3 (Figure 3.2) and its lower bandgap energy (2.87 eV) that lead to the photogenerated electron-hole recombination. Higher phenol degradation rates were observed for the $B_{0.5}$T-1 and PBT-1 catalysts at 45% and

44%, respectively. The higher photocatalytic activity of $B_{0.5}T$-1 can be attributed to its higher crystallinity and the presence of the $Bi_4Ti_3O_{12}$ species (Figure 3.2) that has a lower bandgap energy compared to anatase and can efficiently suppress the photogenerated electron-hole recombination[84]. The presence of P25 in the PBT-1 catalyst did not show any improvement in phenol degradation kinetics compared to the $B_{0.5}T$-1 catalyst (Figure 3.24).

Table 3.5. Apparent rate constants for phenol photodegradation

Catalyst	k_{app} **/min**$^{-1}$
PT-1	$1.08\times10^{-3}\pm(3.2\times10^{-4})$
PBT-1	$3.22\times10^{-3}\pm(5.2\times10^{-4})$
$B_{0.5}T$-0	$1.58\times10^{-3}\pm(1.8\times10^{-4})$
$B_{0.5}T$-0.5	$2.34\times10^{-3}\pm(1.1\times10^{-4})$
$B_{0.5}T$-1	$3.26\times10^{-3}\pm(9.7\times10^{-4})$
$B_{0.25}T$-2	$3.60\times10^{-3}\pm(2.3\times10^{-4})$
$B_{0.5}T$-2	$2.80\times10^{-3}\pm(1.5\times10^{-4})$
B_1T-2	$2.10\times10^{-3}\pm(6.9\times10^{-4})$

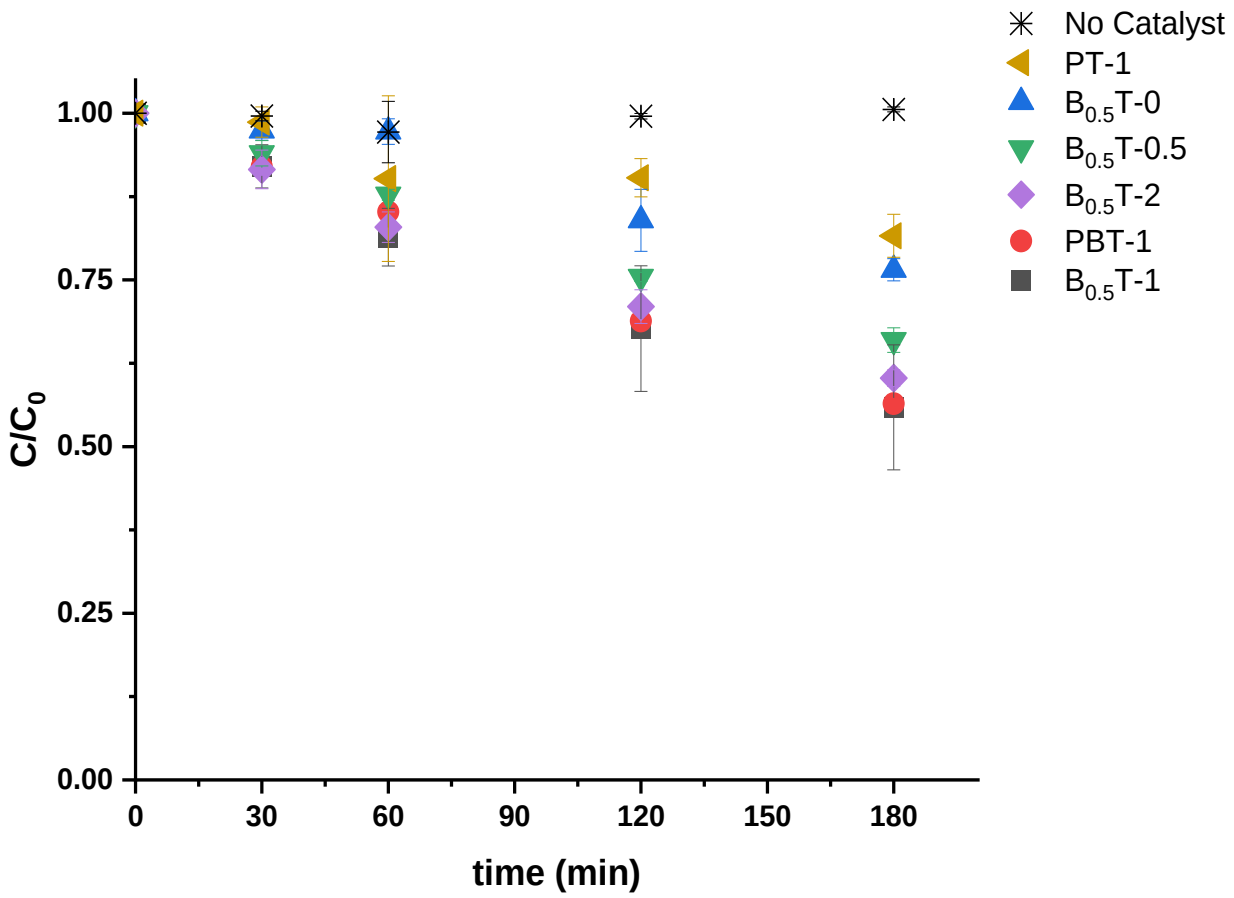

Figure 3.24. Time concentration plots for the photodegradation of phenol 1×10^{-4} M photocatalysts (0.04 g) synthesized using same amount bismuth (Ti:Bi =1:0.5) and changing amounts of Tween 80

The effect of Bi concentration in the photocatalysts on phenol photodegradation is shown in Figure 3.25. In the absence of Bi, the catalyst T-2 did not show any phenol degradation. The lower activity is due to the insufficient photon energy at 420 nm (2.952 eV) compared to the bandgap energy of anatase at 3.26 eV. The photodegradation rate increased with the addition of Bi to the catalysts. However, catalysts with the lowest Bi concentration ($B_{0.25}$T-2) showed a higher phenol degradation activity compared to the other catalysts with higher Bi concentrations ($B_{0.5}$T-2 and B_1T-2). This may be attributed to the decreasing bandgap energy (Figure 3.13) due to the presence of multiphase components,

which allows efficient absorption of radiation at 420 nm wavelength to generate electron-hole pairs. It has been found that photocatalytic activity of $Bi_4Ti_3O_{12}$ only is poor due to its less adsorption ability of organic compounds[85]. Even though lowering the bandgap enhances the possibility of recombination of electron-hole pairs, the coexistence of multiple phases, such as anatase, Bi_2O_3, and $Bi_4Ti_3O_{12}$, minimizes the recombination rate[26]. Several studies have shown that $Bi_4Ti_3O_{12}/TiO_2$ heterojunction catalysts have a higher activity than $Bi_4Ti_3O_{12}$ or TiO_2 alone due to their lower electron-hole recombination[23,86,87]. Accordingly, the % degradation of phenol by the $B_{0.25}$T-2 catalyst shows a ~6% higher value than the $B_{0.5}$T-2 catalyst and ~ 14% higher value than B_1T-2.

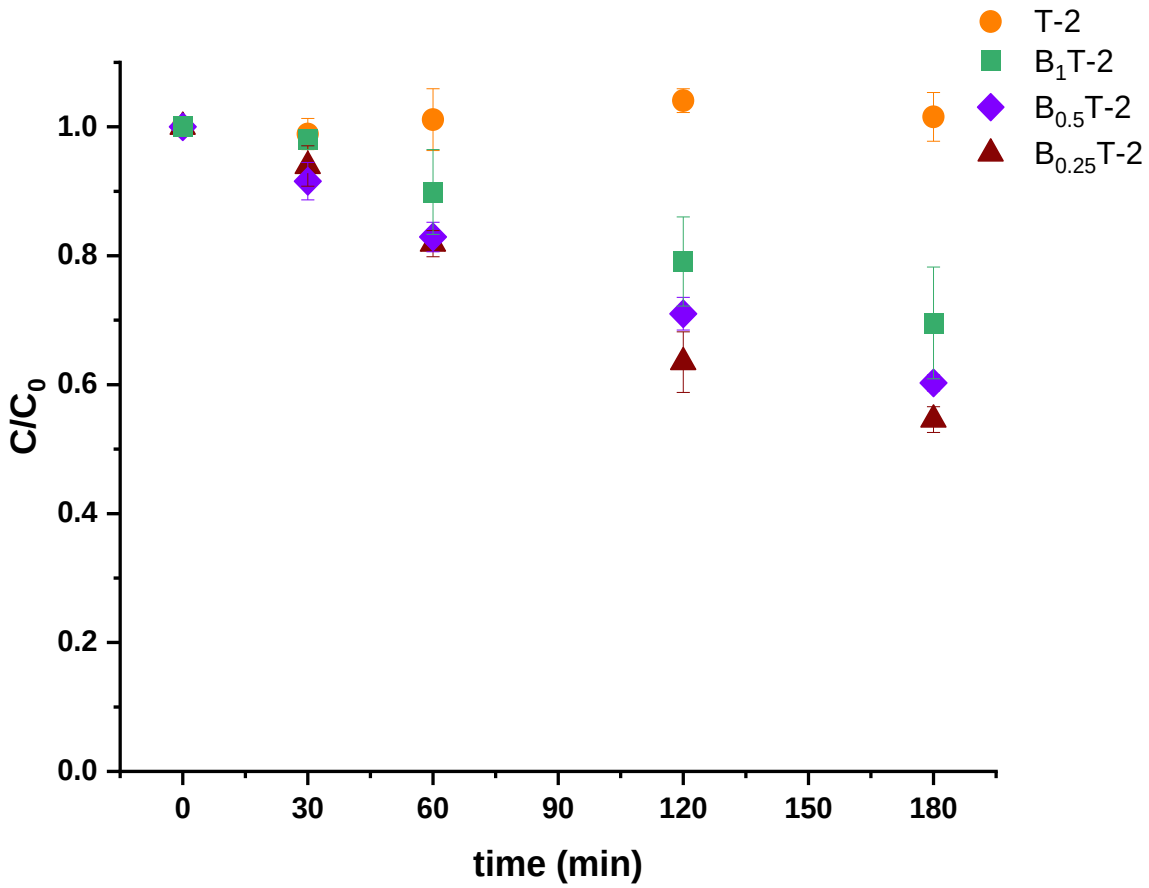

Figure 3.25. Time concentration plots for the photodegradation of phenol 1×10^{-4} M photocatalysts (0.04 g) synthesized varying bismuth concentration (Ti: Bi =1:0, 1:0.25,1:0.5,1:1) and constant Tween-80

3.4.4. Photocatalytic degradation mechanism

Catalysts with a double heterojunction are reported to be more efficient in inhibiting the electron-hole recombination than those with a single heterojunction[35]. The improved activity of multiphase composite materials can be explained by the band structure of their components. A possible catalytic mechanism for ternary heterojunction composite is proposed in Figure 3.26, which is similar to the study done by Zhao et al[35]. CB and VB positions can be calculated using the empirical equation[88,89],

$$E_{CB} = X - E_e - 0.5\, E_g$$

where E_{CB} is the CB edge potential, X is the geometric mean of Mullikan electronegativity of the constituent atoms (Bi_2O_3 = 6.23 eV, $Bi_4Ti_3O_{12}$ = 4.12 eV, TiO_2 = 5 .81eV) [25], E_e is the energy of free electrons on the hydrogen scale (about 4.5 eV), and E_g is the bandgap energy. The E_g values for bare Bi_2O_3, $Bi_4Ti_3O_{12}$, and TiO_2 were calculated according to the UV-Visible diffuse reflectance measurements as 2.87, 3.25, and 3.26 eV, respectively. The E_{CB} values at the points of zero charge were estimated as, Bi_2O_3 = 0.33 eV, $Bi_4Ti_3O_{12}$ = -1.98 eV, and TiO_2 = -0.32 eV. According to these values, the calculated VB potentials (E_{VB}) of Bi_2O_3, $Bi_4Ti_3O_{12}$, and TiO_2 are 3.20, 1.27, and 2.94 eV, respectively.

Electrons in the VB of Bi_2O_3 can be excited by visible light up to 442.8 nm due to its low bandgap energy (2.80 eV)[90]. Consequently, the photo-induced holes of Bi_2O_3 can be transferred into the VB of $Bi_4Ti_3O_{12}$, disturbing its charge balance, as explained in a similar study done by Zhao et al[35]. The $Bi_4Ti_3O_{12}$ CB electrons can then migrate to the CB of TiO_2 that possesses a lower energy level (Figure 3.26), where photocatalytic reactions are initiated. The CB position of TiO_2 (-0.32 eV) is more negative than the potential for O_2 reduction to superoxide ($EO_2/\bullet O_2^-$ = -0.046 eV)[26]. Therefore, electrons transferred to CB

of TiO_2 can react with O_2 on its surface to produce $^{\bullet}O_2^-$, and through a series of reactions, hydroxyl radicals ($^{\bullet}OH$)[4]. The VB positions of TiO_2 (3.20 eV) are higher than those of $E^{\bullet}OH/OH^-$ (2.38 eV) and $E^{\bullet}OH/H_2O$ (2.72 eV), resulting in the generation of hydroxyl radicals at the VB of Bi_2O_3. According to the proposed scheme, holes are not generated at the VB of TiO_2, but the holes generated at the VB of Bi_2O_3 are transferred to the VB of $Bi_4Ti_3O_{12}$.

On the whole, photocatalytic activity is enhanced mainly due to the efficient separation of charge carriers within the heterostructures. A lower Bi concentration in the $B_{0.25}$T-2 catalyst shows that more multiphase species coexist in the same catalyst as observed in the XRD analysis (Figure 3.2). Therefore, the highest phenol degradation activity observed for the $B_{0.25}$T-2 catalyst can be attributed to the aforementioned lower bandgap and less recombination brought about by the presence of multiphase species.

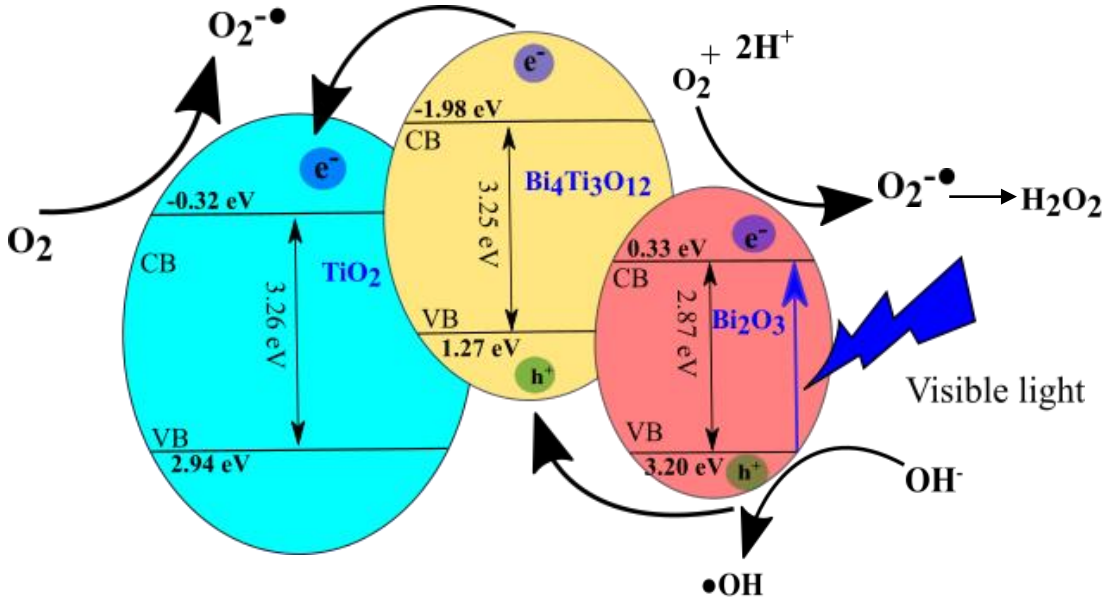

Figure 3.26. Schematic diagram for photocatalytic mechanism in TiO_2/ $Bi_4Ti_3O_{12}$/ Bi_2O_3 heterostructure

3.5. Conclusions

In this study, we have shown that the resulting oxide phases of the catalyst mixture and their crystallinity can be controlled by incorporating Tween-80, a non-ionic surfactant, into the bismuth-titanate sol-gel synthesis scheme. The catalysts synthesized in this study showed major crystalline phases as Bi_2O_3, TiO_2 (anatase), and $Bi_4Ti_3O_{12}$. The bismuth-titanate ($Bi_4Ti_3O_{12}$) fraction in the catalysts was increased by increasing the Tween-80 concentration (Tween-80:Ti molar ratio = 0 < 0.5:1 < 1:1 < 2:1), while keeping the Bi and Ti concentrations constant in the sol-gel mixture (Ti:Bi molar ratio =1:0.5). Also, at an optimum level of surfactant (Tween-80:Ti molar ratio = 2:1), increasing the Bi concentration (Ti:Bi molar ratio = 1:0.25 < 1:0.5 < 1:1) resulted in an increase in the $Bi_4Ti_3O_{12}$ concentration in the catalyst. The combination of Bi_2O_3, TiO_2 (anatase), and $Bi_4Ti_3O_{12}$ resulted in a visible light-active photocatalyst that can effectively degrade phenol under 420 nm light illumination. It was identified that it is vital to have all three crystalline phases (Bi_2O_3, TiO_2 (anatase), and $Bi_4Ti_3O_{12}$) in the catalyst mixture to degrade phenol successfully. The lack of any of these semiconductor species resulted in a less than optimal photocatalytic activity under visible light. It can be concluded that photocatalytic activity of the ternary structured catalysts is enhanced due to the efficient separation of charge carriers within the heterostructures. The catalyst synthesized with a lower Bi content (Ti:Bi ratio = 1:0.25) and higher Tween-80 concentration (Tween-80:Ti ratio = 2:1) showed the coexistence of Bi_2O_3, TiO_2 (anatase), and $Bi_4Ti_3O_{12}$ that resulted in a lower bandgap energy and an optimal photocatalytic activity under visible light.

3.6. REFERENCES

(1) Zhao, X.; Yang, H.; Li, S.; Cui, Z.; Zhang, C. Synthesis and Theoretical Study of Large-Sized $Bi_4Ti_3O_{12}$ Square Nanosheets with High Photocatalytic Activity. *Materials Research Bulletin* **2018**, *107*, 180–188. https://doi.org/10.1016/j.materresbull.2018.07.018.

(2) Ye, Y.; Yang, H.; Li, R.; Wang, X. Enhanced Photocatalytic Performance and Mechanism of Ag-Decorated $LaFeO_3$ Nanoparticles. *J Sol-Gel Sci Technol* **2017**, *82* (2), 509–518. https://doi.org/10.1007/s10971-017-4332-0.

(3) Fujishima, A.; Honda, K. Electrochemical Photolysis of Water at a Semiconductor Electrode. *nature* **1972**, *238* (5358), 37–38.

(4) Hoffmann, M. R.; Martin, S. T.; Choi, W.; Bahnemann, D. W. Environmental Applications of Semiconductor Photocatalysis. *Chemical reviews* **1995**, *95* (1), 69–96.

(5) Fujishima, A.; Rao, T. N.; Tryk, D. A. Titanium Dioxide Photocatalysis. *Journal of Photochemistry and Photobiology C: Photochemistry Reviews* **2000**, *1* (1), 1–21.

(6) Lee, S.-Y.; Park, S.-J. TiO_2 Photocatalyst for Water Treatment Applications. *Journal of Industrial and Engineering Chemistry* **2013**, *19* (6), 1761–1769. https://doi.org/10.1016/j.jiec.2013.07.012.

(7) Dahl, M.; Liu, Y.; Yin, Y. Composite Titanium Dioxide Nanomaterials. *Chem. Rev.* **2014**, *114* (19), 9853–9889. https://doi.org/10.1021/cr400634p.

(8) An, H.; Du, Y.; Wang, T.; Wang, C.; Hao, W.; Zhang, J. Photocatalytic Properties of BiOX (X = Cl, Br, and I). *Rare Metals* **2008**, *27* (3), 243–250. https://doi.org/10.1016/S1001-0521(08)60123-0.

(9) Meng, X.; Zhang, Z. Facile Synthesis of $BiOBr/Bi_2WO_6$ Heterojunction Semiconductors with High Visible-Light-Driven Photocatalytic Activity. *Journal of Photochemistry and Photobiology A: Chemistry* **2015**, *310*, 33–44. https://doi.org/10.1016/j.jphotochem.2015.04.024.

(10) Hou, J.; Cao, R.; Jiao, S.; Zhu, H.; Kumar, R. V. PANI/$Bi_{12}TiO_{20}$ Complex Architectures: Controllable Synthesis and Enhanced Visible-Light Photocatalytic Activities. *Applied Catalysis B: Environmental* **2011**, *104* (3), 399–406. https://doi.org/10.1016/j.apcatb.2011.02.032.

(11) Zhu, X.; Zhang, J.; Chen, F. Hydrothermal Synthesis of Nanostructures $Bi_{12}TiO_{20}$ and Their Photocatalytic Activity on Acid Orange 7 under Visible Light. *Chemosphere* **2010**, *78* (11), 1350–1355. https://doi.org/10.1016/j.chemosphere.2010.01.002.

(12) Hou, J.; Jiao, S.; Zhu, H.; Kumar, R. V. Bismuth Titanate Pyrochlore Microspheres: Directed Synthesis and Their Visible Light Photocatalytic Activity. *Journal of Solid State Chemistry* **2011**, *184* (1), 154–158. https://doi.org/10.1016/j.jssc.2010.11.017.

(13) Yao, W. F.; Wang, H.; Xu, X. H.; Zhou, J. T.; Yang, X. N.; Zhang, Y.; Shang, S. X. Photocatalytic Property of Bismuth Titanate $Bi_2Ti_2O_7$. *Applied Catalysis A: General* **2004**, *259* (1), 29–33. https://doi.org/10.1016/j.apcata.2003.09.004.

(14) Zhou, T.; Hu, J. Mass Production and Photocatalytic Activity of Highly Crystalline Metastable Single-Phase $Bi_{20}TiO_{32}$ Nanosheets. *Environ. Sci. Technol.* **2010**, *44* (22), 8698–8703. https://doi.org/10.1021/es1019959.

(15) Cheng, H.; Huang, B.; Dai, Y.; Qin, X.; Zhang, X.; Wang, Z.; Jiang, M. Visible-Light Photocatalytic Activity of the Metastable $Bi_{20}TiO_{32}$ Synthesized by a High-Temperature Quenching Method. *Journal of Solid State Chemistry* **2009**, *182* (8), 2274–2278. https://doi.org/10.1016/j.jssc.2009.06.006.

(16) Yao, W. F.; Xu, X. H.; Wang, H.; Zhou, J. T.; Yang, X. N.; Zhang, Y.; Shang, S. X.; Huang, B. B. Photocatalytic Property of Perovskite Bismuth Titanate. *Applied Catalysis B: Environmental* **2004**, *52* (2), 109–116. https://doi.org/10.1016/j.apcatb.2004.04.002.

(17) LIN, X.; GUAN, Q.-F.; LIU, T.-T.; ZHANG, Y.; ZOU, C.-J. Controllable Synthesis and Photocatalytic Activity of $Bi_4Ti_3O_{12}$ Particles with Different Morphologies. *Acta Physico-Chimica Sinica* **2013**, *29* (2), 411–417.

(18) Wang, L.; Ma, W.; Fang, Y.; Zhang, Y.; Jia, M.; Li, R.; Huang, Y. $Bi_4Ti_3O_{12}$ Synthesized by High Temperature Solid Phase Method and It's Visible Catalytic

Activity. *Procedia Environmental Sciences* **2013**, *18*, 547–558. https://doi.org/10.1016/j.proenv.2013.04.074.

(19) XU, X. H.; WANG, M.; HOU, Y.; YAO, W. F.; WANG, D.; WANG, H. Preparation and Characterization of Bi-Doped TiO_2 Photocatalyst. *J. mater. sci. lett* **2002**, *21* (21), 1655–1656.

(20) Srivastava, A. M.; Ackerman, J. F.; Beers, W. W. On the Luminescence of $Ba_5M_4O_{15}$(M=Ta5+, Nb5+). *Journal of Solid State Chemistry* **1997**, *134* (1), 187–191. https://doi.org/10.1006/jssc.1997.7574.

(21) Blasse, G. The Influence of Crystal Structure on the Luminescence of Tantalates and Niobates. *Journal of Solid State Chemistry* **1988**, *72* (1), 72–79. https://doi.org/10.1016/0022-4596(88)90010-2.

(22) Cao, T.; Li, Y.; Wang, C.; Zhang, Z.; Zhang, M.; Shao, C.; Liu, Y. $Bi_4Ti_3O_{12}$ Nanosheets/TiO_2 Submicron Fibers Heterostructures: In Situ Fabrication and High Visible Light Photocatalytic Activity. *J. Mater. Chem.* **2011**, *21* (19), 6922. https://doi.org/10.1039/c1jm10343a.

(23) Tian, H.; Chen, K.; Ye, X.; Yang, S.; Gu, Q. Hydrothermal Growth of $Bi_2Ti_2O_7$/TiO_2 and $Bi_4Ti_3O_{12}$/TiO_2 Heterostructures on Highly Ordered TiO_2-Nanotube Arrays for Dye-Sensitized Solar Cells. *Ceramics International* **2019**, *45* (16), 20750–20757. https://doi.org/10.1016/j.ceramint.2019.07.059.

(24) Yuan, Y.; Xiao, Z.; Yang, B.; Huang, J. Arising Applications of Ferroelectric Materials in Photovoltaic Devices. *J. Mater. Chem. A* **2014**, *2* (17), 6027–6041. https://doi.org/10.1039/c3ta14188h.

(25) Xu, Y.; Schoonen, M. A. A. The Absolute Energy Positions of Conduction and Valence Bands of Selected Semiconducting Minerals. *American Mineralogist* **2000**, *85* (3–4), 543–556. https://doi.org/10.2138/am-2000-0416.

(26) Wang, L.; Li, H.; Zhang, S.; Long, Y.; Li, L.; Zheng, Z.; Wu, S.; Zhou, L.; Hei, Y.; Luo, L.; Jiang, F. One-Step Synthesis of $Bi_4Ti_3O_{12}$/Bi_2O_3/$Bi_{12}TiO_{20}$ Spherical Ternary Heterojunctions with Enhanced Photocatalytic Properties via Sol-Gel Method. *Solid State Sciences* **2020**, *100*, 106098. https://doi.org/10.1016/j.solidstatesciences.2019.106098.

(27) Huang, Y.; Mi, L.; Liu, X.; Bi, S.; Seo, H. J. Band Structure, Photochemical Properties and Luminescence Characteristics of (Ni,F)-Doped α-Bi_2O_3 Nanorods via Facile Hydrothermal Synthesis. *J. Phys. D: Appl. Phys.* **2018**, *52* (2), 025101. https://doi.org/10.1088/1361-6463/aae633.

(28) Ikram, M.; Liu, L.; Lv, H.; Liu, Y.; Ur Rehman, A.; Kan, K.; Zhang, W.; He, L.; Wang, Y.; Wang, R.; Shi, K. Intercalation of Bi_2O_3/Bi_2S_3 Nanoparticles into Highly Expanded MoS_2 Nanosheets for Greatly Enhanced Gas Sensing Performance at Room Temperature. *Journal of Hazardous Materials* **2019**, *363*, 335–345. https://doi.org/10.1016/j.jhazmat.2018.09.077.

(29) Najafian, H.; Manteghi, F.; Beshkar, F.; Salavati-Niasari, M. Enhanced Photocatalytic Activity of a Novel NiO/Bi_2O_3/Bi_3ClO_4 Nanocomposite for the Degradation of Azo Dye Pollutants under Visible Light Irradiation. *Separation and Purification Technology* **2019**, *209*, 6–17. https://doi.org/10.1016/j.seppur.2018.07.010.

(30) Lv, P.; Zheng, M.; Wang, X.; Huang, F. Subsolidus Phase Relationships and Photocatalytic Properties in the Ternary System TiO_2–Bi_2O_3–V_2O_5. *Journal of Alloys and Compounds* **2014**, *583*, 285–290. https://doi.org/10.1016/j.jallcom.2013.07.156.

(31) Peng, W.; Yang, C.; Yu, J. Bi_2 O_3 and g-C_3 N_4 Quantum Dot Modified Anatase TiO_2 Heterojunction System for Degradation of Dyes under Sunlight Irradiation. *RSC Adv.* **2020**, *10* (2), 1181–1190. https://doi.org/10.1039/C9RA07424D.

(32) Ren, C.; Qiu, W.; Zhang, H.; He, Z.; Chen, Y. Degradation of Benzene on TiO_2/SiO_2/Bi_2O_3 Photocatalysts under UV and Visible Light. *Journal of Molecular Catalysis A: Chemical* **2015**, *398*, 215–222. https://doi.org/10.1016/j.molcata.2014.12.007.

(33) Chang, M.-J.; Cui, W.-N.; Liu, J.; Wang, K.; Du, H.-L.; Qiu, L.; Fan, S.-M.; Luo, Z.-M. Construction of Novel TiO_2/$Bi_4Ti_3O_{12}$/MoS_2 Core/Shell Nanofibers for Enhanced Visible Light Photocatalysis. *Journal of Materials Science & Technology* **2020**, *36*, 97–105. https://doi.org/10.1016/j.jmst.2019.06.020.

(34) Kumar, A.; Sharma, G.; Kumari, A.; Guo, C.; Naushad, Mu.; Vo, D.-V. N.; Iqbal, J.; Stadler, F. J. Construction of Dual Z-Scheme g-C_3N_4/$Bi_4Ti_3O_{12}$/$Bi_4O_5I_2$ Heterojunction for Visible and Solar Powered Coupled Photocatalytic Antibiotic Degradation and Hydrogen Production: Boosting via I−/I3− and Bi3+/Bi5+ Redox

Mediators. *Applied Catalysis B: Environmental* **2021**, *284*, 119808. https://doi.org/10.1016/j.apcatb.2020.119808.

(35) Zhao, Z.; Tian, J.; Wang, D.; Kang, X.; Sang, Y.; Liu, H.; Wang, J.; Chen, S.; Boughton, R. I.; Jiang, H. UV-Visible-Light-Activated Photocatalysts Based on Bi_2O_3/$Bi_4Ti_3O_{12}$/TiO_2 Double-Heterostructured TiO_2 Nanobelts. *J. Mater. Chem.* **2012**, *22* (44), 23395. https://doi.org/10.1039/c2jm34580c.

(36) Liang, Q.; Liu, X.; Zeng, G.; Liu, Z.; Tang, L.; Shao, B.; Zeng, Z.; Zhang, W.; Liu, Y.; Cheng, M.; Tang, W.; Gong, S. Surfactant-Assisted Synthesis of Photocatalysts: Mechanism, Synthesis, Recent Advances and Environmental Application. *Chemical Engineering Journal* **2019**, *372*, 429–451. https://doi.org/10.1016/j.cej.2019.04.168.

(37) Gordon, T. R.; Cargnello, M.; Paik, T.; Mangolini, F.; Weber, R. T.; Fornasiero, P.; Murray, C. B. Nonaqueous Synthesis of TiO_2 Nanocrystals Using TiF_4 to Engineer Morphology, Oxygen Vacancy Concentration, and Photocatalytic Activity. *J. Am. Chem. Soc.* **2012**, *134* (15), 6751–6761. https://doi.org/10.1021/ja300823a.

(38) Xu, X.; Gao, Z.; Cui, Z.; Liang, Y.; Li, Z.; Zhu, S.; Yang, X.; Ma, J. Synthesis of Cu_2O Octadecahedron/TiO_2 Quantum Dot Heterojunctions with High Visible Light Photocatalytic Activity and High Stability. *ACS Appl. Mater. Interfaces* **2016**, *8* (1), 91–101. https://doi.org/10.1021/acsami.5b06536.

(39) Zinovjev, K.; Tuñón, I. Reaction Coordinates and Transition States in Enzymatic Catalysis. *WIREs Computational Molecular Science* **2018**, *8* (1), e1329. https://doi.org/10.1002/wcms.1329.

(40) Joseph, D.; Lee, H.; Huh, Y. S.; Han, Y.-K. Cylindrical Core-Shell Tween 80 Micelle Templated Green Synthesis of Gold-Silver Hollow Cubic Nanostructures as Efficient Nanocatalysts. *Materials & Design* **2018**, *160*, 169–178. https://doi.org/10.1016/j.matdes.2018.09.003.

(41) Hamza, M. A.; Abou-Gamra, Z. M.; Ahmed, M. A.; Medien, H. A. A. The Critical Role of Tween 80 as a 'Green' Template on the Physical Properties and Photocatalytic Performance of TiO_2 Nanoparticles for Rhodamine B Photodegradation. *J Mater Sci: Mater Electron* **2020**, *31* (6), 4650–4661. https://doi.org/10.1007/s10854-020-03017-2.

(42) Rahut, S.; Basu, S. S.; Basu, J. K. Surfactant Assisted Self-Assembly of Ag^{+} Containing Nanocrystals and Their Facet Dependent Photocatalytic Activity. *CrystEngComm* **2019**, *21* (1), 23–29. https://doi.org/10.1039/C8CE01563E.

(43) Ntakirutimana, S.; Tan, W. Electrochemical Capacitive Behaviors of Carbon/Titania Composite Prepared by Tween 80-Assisted Sol-Gel Process for Capacitive Deionization. *Desalination* **2021**, *512*, 115131. https://doi.org/10.1016/j.desal.2021.115131.

(44) Karunakaran, C.; Magesan, P.; Gomathisankar, P. Photocatalytic Activity of Sol-Gel Derived Bi_2O_3-TiO_2 Nanocomposite. *MSF* **2012**, *712*, 73–83. https://doi.org/10.4028/www.scientific.net/MSF.712.73.

(45) Han, L.; Zheng, L.; Hu, Z.; Yin, S.; Zeng, Y. Preparation of Spherical Bi_3.25La0.75Ti_3O_{12} Nanocrystals by a Sol-Gel Inverse Mini-Emulsion Approach. *Electron. Mater. Lett.* **2014**, *10* (1), 1–4. https://doi.org/10.1007/s13391-013-3064-8.

(46) Yaparatne, S.; Tripp, C. P.; Amirbahman, A. Photodegradation of Taste and Odor Compounds in Water in the Presence of Immobilized TiO_2 -SiO_2 Photocatalysts. *Journal of Hazardous Materials* **2018**, *346*, 208–217. https://doi.org/10.1016/j.jhazmat.2017.12.029.

(47) Correia, F. C.; Calheiros, M.; Marques, J.; Ribeiro, J. M.; Tavares, C. J. Synthesis of Bi_2O_3/TiO_2 Nanostructured Films for Photocatalytic Applications. *Ceramics International* **2018**, *44* (18), 22638–22644. https://doi.org/10.1016/j.ceramint.2018.09.040.

(48) Solís-Casados, D. A.; Escobar-Alarcón, L.; Arrieta-Castañeda, A.; Haro-Poniatowski, E. Bismuth–Titanium Oxide Nanopowders Prepared by Sol–Gel Method for Photocatalytic Applications. *Materials Chemistry and Physics* **2016**, *172*, 11–19. https://doi.org/10.1016/j.matchemphys.2015.12.002.

(49) Cheng, H.; Huang, B.; Lu, J.; Wang, Z.; Xu, B.; Qin, X.; Zhang, X.; Dai, Y. Synergistic Effect of Crystal and Electronic Structures on the Visible-Light-Driven Photocatalytic Performances of Bi_2O_3 Polymorphs. *Phys. Chem. Chem. Phys.* **2010**, *12* (47), 15468. https://doi.org/10.1039/c0cp01189d.

(50) Liu, G.; Li, S.; Lu, Y.; Zhang, J.; Feng, Z.; Li, C. Controllable Synthesis of α-$Bi2O_3$ and γ-Bi_2O_3 with High Photocatalytic Activity by α-Bi_2O_3→γ-Bi_2O_3→α-Bi_2O3 Transformation in a Facile Precipitation Method. *Journal of Alloys and Compounds* **2016**, *689*, 787–799. https://doi.org/10.1016/j.jallcom.2016.08.047.

(51) Iyyapushpam, S.; Nishanthi, S. T.; Pathinettam Padiyan, D. Enhanced Photocatalytic Degradation of Methyl Orange by Gamma Bi2O3 and Its Kinetics. *Journal of Alloys and Compounds* **2014**, *601*, 85–87. https://doi.org/10.1016/j.jallcom.2014.02.142.

(52) Solís-Casados, D. A.; Escobar-Alarcón, L.; Alvarado-Pérez, V.; Haro-Poniatowski, E. Photocatalytic Activity under Simulated Sunlight of Bi-Modified TiO_2 Thin Films Obtained by Sol Gel. *International Journal of Photoenergy* **2018**, *2018*, 1–9. https://doi.org/10.1155/2018/8715987.

(53) García-Muñoz, P.; Pliego, G.; Zazo, J. A.; Bahamonde, A.; Casas, J. A. Ilmenite ($FeTiO_3$) as Low Cost Catalyst for Advanced Oxidation Processes. *Journal of Environmental Chemical Engineering* **2016**, *4* (1), 542–548. https://doi.org/10.1016/j.jece.2015.11.037.

(54) Gautam, C. R.; Madheshiya, A.; Dwivedi, R. K. Synthesis, Crystallization, and Dielectric Behaviour of Lead Bismuth Titanate Borosilicate Glasses with Addition of 1% La_2O_3. *Indian Journal of Materials Science* **2015**, *2015*, 1–10. https://doi.org/10.1155/2015/498254.

(55) Sood, S.; Mehta, S. K.; Sinha, A. S. K.; Kansal, S. K. Bi $_2O_3$/TiO_2 Heterostructures: Synthesis, Characterization and Their Application in Solar Light Mediated Photocatalyzed Degradation of an Antibiotic, Ofloxacin. *Chemical Engineering Journal* **2016**, *290*, 45–52. https://doi.org/10.1016/j.cej.2016.01.017.

(56) Gul, I.; Sayed, M.; Shah, N. S.; Ali Khan, J.; Polychronopoulou, K.; Iqbal, J.; Rehman, F. Solar Light Responsive Bismuth Doped Titania with Ti3+ for Efficient Photocatalytic Degradation of Flumequine: Synergistic Role of Peroxymonosulfate. *Chemical Engineering Journal* **2020**, *384*, 123255. https://doi.org/10.1016/j.cej.2019.123255.

(57) Sajjad, S.; Leghari, S. A. K.; Chen, F.; Zhang, J. Bismuth-Doped Ordered Mesoporous TiO2: Visible-Light Catalyst for Simultaneous Degradation of Phenol and Chromium. *Chem. Eur. J.* **2010**, *16* (46), 13795–13804. https://doi.org/10.1002/chem.201001099.

(58) Zhang, Y.; Gao, J.; Chen, Z.; Lu, Z. Enhanced Photocatalytic Performance of Bi4Ti3O12 Nanosheets Synthesized by a Self-Catalyzed Fast Reaction Process. *Ceramics International* **2018**, *44* (18), 23014–23023. https://doi.org/10.1016/j.ceramint.2018.09.103.

(59) Preparation and Characterization of Bi_3+-TiO_2 and Its Photocatalytic Activity. *Chem. Eng. Technol.* **2007**, No. 5, 6.

(60) Yang, J. Energy Storage Ability and Anti-Corrosion Properties of Bi-Doped TiO_2 Nanotube Arrays. *Electrochimica Acta* **2015**, 6.

(61) Liu, J.; Sun, M.; Chang, M.-J.; Cui, W.-N.; Zhang, C.-M.; Ni, F.-R.; Zhang, J.; Fan, S.-M.; Du, H.-L. Novel TiO_2/$Bi_4Ti_3O_{12}$ Nanorod Arrays Decorated with Co-Pi for Boosted Solar Photoelectrochemical Water Splitting. *Journal of Physics and Chemistry of Solids* **2021**, *157*, 110179. https://doi.org/10.1016/j.jpcs.2021.110179.

(62) López, R.; Gómez, R. Band-Gap Energy Estimation from Diffuse Reflectance Measurements on Sol–Gel and Commercial TiO_2: A Comparative Study. *J Sol-Gel Sci Technol* **2012**, *61* (1), 1–7. https://doi.org/10.1007/s10971-011-2582-9.

(63) Makuła, P.; Pacia, M.; Macyk, W. How To Correctly Determine the Band Gap Energy of Modified Semiconductor Photocatalysts Based on UV–Vis Spectra. *J. Phys. Chem. Lett.* **2018**, *9* (23), 6814–6817. https://doi.org/10.1021/acs.jpclett.8b02892.

(64) Sharma, R.; Khanuja, M.; Sharma, S. N.; Sinha, O. P. Reduced Band Gap & Charge Recombination Rate in Se Doped α-Bi_2O_3 Leads to Enhanced Photoelectrochemical and Photocatalytic Performance: Theoretical & Experimental Insight. *International Journal of Hydrogen Energy* **2017**, *42* (32), 20638–20648. https://doi.org/10.1016/j.ijhydene.2017.07.011.

(65) Madhusudan Reddy, K.; Manorama, S. V.; Ramachandra Reddy, A. Bandgap Studies on Anatase Titanium Dioxide Nanoparticles. *Materials Chemistry and Physics* **2003**, *78* (1), 239–245. https://doi.org/10.1016/S0254-0584(02)00343-7.

(66) Hao, P.; Zhao, Z.; Tian, J.; Sang, Y.; Yu, G.; Liu, H.; Chen, S.; Zhou, W. Bismuth Titanate Nanobelts through a Low-Temperature Nanoscale Solid-State Reaction. *Acta Materialia* **2014**, *62*, 258–266. https://doi.org/10.1016/j.actamat.2013.10.006.

(67) Liu, Y.; Xin, F.; Wang, F.; Luo, S.; Yin, X. Synthesis, Characterization, and Activities of Visible Light-Driven Bi_2O_3–TiO_2 Composite Photocatalysts. *Journal of Alloys and Compounds* **2010**, *498* (2), 179–184. https://doi.org/10.1016/j.jallcom.2010.03.151.

(68) Wei, W.; Dai, Y.; Huang, B. First-Principles Characterization of Bi-Based Photocatalysts: $Bi_{12}TiO_{20}$, $Bi_2Ti_2O_7$, and $Bi_4Ti_3O_{12}$. *J. Phys. Chem. C* **2009**, *113* (14), 5658–5663. https://doi.org/10.1021/jp810344e.

(69) Dias, J. A.; Oliveira, J. A.; Renda, C. G.; Morelli, M. R. Production of Nanometric $Bi_4Ti_3O_{12}$ Powders: From Synthesis to Optical and Dielectric Properties. *Mat. Res.* **2018**, *21* (5). https://doi.org/10.1590/1980-5373-mr-2018-0118.

(70) Tu, S.; Huang, H.; Zhang, T.; Zhang, Y. Controllable Synthesis of Multi-Responsive Ferroelectric Layered Perovskite-like $Bi_4Ti_3O_{12}$: Photocatalysis and Piezoelectric-Catalysis and Mechanism Insight. *Applied Catalysis B: Environmental* **2017**, *219*, 550–562. https://doi.org/10.1016/j.apcatb.2017.08.001.

(71) Carp, O. Photoinduced Reactivity of Titanium Dioxide. *Progress in Solid State Chemistry* **2004**, *32* (1–2), 33–177. https://doi.org/10.1016/j.progsolidstchem.2004.08.001.

(72) Gopal, R.; Kathirgamanathan, P.; Ravi, G.; Elangovan, T.; Kumar, B.; Manivannan, N.; Kasinathan, K.; Arjunkumar, B. Quantum Confinement Effect of 2D Nanomaterials; 2020. https://doi.org/10.5772/intechopen.90140.

(73) Singh, M.; Goyal, M.; Devlal, K. Size and Shape Effects on the Band Gap of Semiconductor Compound Nanomaterials. *Journal of Taibah University for Science* **2018**, *12* (4), 470–475. https://doi.org/10.1080/16583655.2018.1473946.

(74) Thommes, M.; Kaneko, K.; Neimark, A. V.; Olivier, J. P.; Rodriguez-Reinoso, F.; Rouquerol, J.; Sing, K. S. W. Physisorption of Gases, with Special Reference to the Evaluation of Surface Area and Pore Size Distribution (IUPAC Technical Report). *Pure and Applied Chemistry* **2015**, *87* (9–10), 1051–1069. https://doi.org/10.1515/pac-2014-1117.

(75) Xue, L.; Qing-Feng, G.; Ting-Ting, L.; Yao, Z.; Chun-Jie, Z.; 1 ; 1 College of Chemistry, Key Laboratory of Preparation and Application Environmentally Friendly Materials of the Ministry of Education, Jilin Normal University, Siping 136000, Jilin Province, P. R. China;; 2 School of Materials Science and Engineering, Jiangsu University, Zhenjiang 212013, Jiangsu Province, P. R. China. Controllable Synthesis and Photocatalytic Activity of $Bi_4Ti_3O_{12}$ Particles with Different Morphologies. *Acta Physico-Chimica Sinica* **2013**, *29* (02), 411–417. https://doi.org/10.3866/PKU.WHXB201211211.

(76) Du, X.; Xu, Y.; Ma, H.; Wang, J.; Li, X. Synthesis and Characterization of Bismuth Titanate by an Aqueous Sol-Gel Method. *J American Ceramic Society* **2007**, *90* (5), 1382–1385. https://doi.org/10.1111/j.1551-2916.2007.01548.x.

(77) Vidyasagar, C. C.; Arthoba Naik, Y. Surfactant (PEG 400) Effects on Crystallinity of ZnO Nanoparticles. *Arabian Journal of Chemistry* **2016**, *9* (4), 507–510. https://doi.org/10.1016/j.arabjc.2012.08.002.

(78) Liu, Y.; Wang, C.; Wei, Y.; Zhu, L.; Li, D.; Jiang, J. S.; Markovic, N. M.; Stamenkovic, V. R.; Sun, S. Surfactant-Induced Postsynthetic Modulation of Pd Nanoparticle Crystallinity. *Nano Lett.* **2011**, *11* (4), 1614–1617. https://doi.org/10.1021/nl104548g.

(79) Choi, H.; Stathatos, E.; Dionysiou, D. D. Synthesis of Nanocrystalline Photocatalytic TiO2 Thin Films and Particles Using Sol–Gel Method Modified with Nonionic Surfactants. *Thin Solid Films* **2006**, *510* (1–2), 107–114. https://doi.org/10.1016/j.tsf.2005.12.217.

(80) Dag, Ö.; Soten, I.; Çelik, Ö.; Polarz, S.; Coombs, N.; Ozin, G. A. Solventless Acid-Free Synthesis of Mesostructured Titania: Nanovessels for Metal Complexes and Metal Nanoclusters. *Advanced Functional Materials* **2003**, *13* (1), 30–36. https://doi.org/10.1002/adfm.200390001.

(81) Stathatos, E.; Lianos, P.; Tsakiroglou, C. Highly Efficient Nanocrystalline Titania Films Made from Organic/Inorganic Nanocomposite Gels. *Microporous and Mesoporous Materials* **2004**, *75* (3), 255–260. https://doi.org/10.1016/j.micromeso.2004.07.006.

(82) Yuenyongsuwan, J.; Nithiyakorn, N.; Sabkird, P.; O'Rear, E. A.; Pongprayoon, T. Surfactant Effect on Phase-Controlled Synthesis and Photocatalyst Property of

TiO2 Nanoparticles. *Materials Chemistry and Physics* **2018**, *214*, 330–336. https://doi.org/10.1016/j.matchemphys.2018.04.111.

(83) Shang, M.; Wang, W.; Zhou, L.; Sun, S.; Yin, W. Nanosized $BiVO_4$ with High Visible-Light-Induced Photocatalytic Activity: Ultrasonic-Assisted Synthesis and Protective Effect of Surfactant. *Journal of Hazardous Materials* **2009**, *172* (1), 338–344. https://doi.org/10.1016/j.jhazmat.2009.07.017.

(84) Qian, K.; Jiang, Z.; Shi, H.; Wei, W.; Zhu, C.; Xie, J. Constructing Mesoporous Bi4Ti3O12 with Enhanced Visible Light Photocatalytic Activity. *Materials Letters* **2016**, *183*, 303–306. https://doi.org/10.1016/j.matlet.2016.07.121.

(85) Zhang, J.; Huang, L.; Liu, P.; Wang, Y.; Jiang, X.; Zhang, E.; Wang, H.; Kong, Z.; Xi, J.; Ji, Z. Heterostructure of Epitaxial (001) $Bi_4Ti_3O_{12}$ Growth on (001) TiO_2 for Enhancing Photocatalytic Activity. *Journal of Alloys and Compounds* **2016**, *654*, 71–78. https://doi.org/10.1016/j.jallcom.2015.09.067.

(86) Chen, K.; Hu, R.; Feng, X.; Xie, K.; Li, Y.; Gu, H. $Bi_4Ti_3O_{12}/TiO_2$ Heterostructure: Synthesis, Characterization and Enhanced Photocatalytic Activity. *Ceramics International* **2013**, *39* (8), 9109–9114. https://doi.org/10.1016/j.ceramint.2013.05.007.

(87) Li, Y.; Dang, L.; Han, L.; Li, P.; Wang, J.; Li, Z. Iodine-Sensitized $Bi_4Ti_3O_{12}/TiO_2$ Photocatalyst with Enhanced Photocatalytic Activity on Degradation of Phenol. *Journal of Molecular Catalysis A: Chemical* **2013**, *379*, 146–151. https://doi.org/10.1016/j.molcata.2013.08.001.

(88) Butler, M. A.; Ginley, D. S. Prediction of Flatband Potentials at Semiconductor-Electrolyte Interfaces from Atomic Electronegativities. *J. Electrochem. Soc.* **1978**, *125* (2), 228–232. https://doi.org/10.1149/1.2131419.

(89) Nethercot, A. H. Prediction of Fermi Energies and Photoelectric Thresholds Based on Electronegativity Concepts. *Phys. Rev. Lett.* **1974**, *33* (18), 1088–1091. https://doi.org/10.1103/PhysRevLett.33.1088.

(90) Wang, L.; Hou, T.; Xin, Y.; Zhu, W.; Yu, S.; Xie, Z.; Liang, S.; Wang, L. Large-Scale Synthesis of Porous Bi_2O_3 with Oxygen Vacancies for Efficient Photodegradation of Methylene Blue. *Chinese Journal of Chemical Physics* **2020**, *33* (4), 500–506. https://doi.org/10.1063/1674-0068/cjcp2001009.

CHAPTER 4 : FUTURE DIRECTIONS

4.1. Preparation of visible light active TiO_2-SiO_2 coatings

In Chapter 2, a robust P25 powder modified TiO_2-SiO_2 photocatalytic film was developed to degrade taste and odor compounds under UV illumination. However, it would be beneficial to avoid energy-consuming UV illumination to degrade organic pollutants and design the catalyst to perform under visible light/sunlight. In order to extend the titania silica film activity to visible range, non-metals such as nitrogen can be doped into the catalysts, or as discussed in Chapter 3, visible light-activated semiconductor bismuth-titanate heterostructures can be tailored to TiO_2-SiO_2 films.

Further characterization of the catalyst films should be conducted for the crystal size using X-ray diffraction analysis to explain the blue shifts in the band edge of Si-incorporated catalysts. Catalyst film characterization by time-resolved photoluminescence is proposed to determine the photogenerated electron-hole recombination efficiency.

4.2. Activity of bismuth incorporated photocatalyst composites

In Chapter 3, a bismuth-titanium photocatalyst was developed, and effective photocatalytic activity with respect to phenol degradation under 420 nm light was achieved. A study of the activity of the catalyst under sunlight or solar simulator is proposed. Photocatalytic activity efficiency can depend on the type of compound that is being degraded. Therefore, it is worthwhile to evaluate the degradation of common emerging drinking water contaminants such as pharmaceutical compounds, and PFAS (poly-fluoroalkyl substances), and algal exudates.

Lowering the illumination time of the catalyst with the organic contaminant and increasing the efficiency of the photocatalytic activity is proposed. This can be achieved by increasing the catalyst loading and designing macroporous catalysts with enhanced surface area.

The heterostructured catalyst composite material should be further studied for its charge carrier separation using photoluminescence spectroscopy and transient photocurrent measurements. In order to verify the photodegradation mechanism towards organic pollutants, photocatalytic experiments with scavengers (ammonium oxalate, para-benzoquinone-, and isopropyl alcohol) are proposed. Ammonium oxalate, para-benzoquinone-, and isopropyl alcohol are scavengers for h^+, $\bullet O^{2-}$ and $\bullet OH$, respectively[1,2]. Furthermore, the reusability of the catalyst should be evaluated and make sure that the heterostructure of the catalyst is stable over multiple uses. The addition of protective layers such as TiO_2 sol-gel coating and nitrogen-doped TiO_2 is proposed to improve the stability of the catalyst particles.

4.3. Implementation of catalyst films for photodegradation of pollutants in pilot scale

Even though numerous lab-scale photocatalytic materials (films and powders) have been synthesized, there is a limited number of studies on using these photocatalysts in actual drinking water or wastewater treatment plants. Based on the results obtained in Chapter 2, a pilot-scale immobilized photocatalyst substrate is proposed to operate along with the UV lamps used in the drinking water treatment facility. The immobilized catalyst substrate should be placed along the flow path such that it would enhance mixing and mass

transfer of the pollutants to the catalyst surface without creating excessive headloss. Coating the outer surface of the UV lamps with catalyst and evaluating the photocatalytic activity is also proposed. The implications of dissolved organic matter and other contaminants in the feed water on photocatalytic efficiency can be assessed as well.

4.4. REFERENCES

(1) Guo, W.; Yang, Y.; Guo, Y.; Jia, Y.; Liu, H.; Guo, Y. Self-Assembled Hierarchical $Bi_{12}TiO_{20}$–Graphene Nanoarchitectures with Excellent Simulated Sunlight Photocatalytic Activity. *Phys. Chem. Chem. Phys.* **2014**, *16* (6), 2705–2714. https://doi.org/10.1039/C3CP53070A.

(2) Xiang, Y.; Ju, P.; Wang, Y.; Sun, Y.; Zhang, D.; Yu, J. Chemical Etching Preparation of the Bi_2WO_6/BiOI p–n Heterojunction with Enhanced Photocatalytic Antifouling Activity under Visible Light Irradiation. *Chemical Engineering Journal* **2016**, *288*, 264–275. https://doi.org/10.1016/j.cej.2015.11.103.

BIOGRAPHY OF THE AUTHOR

Sudheera Yaparatne was born in Kandy, Sri Lanka on May 3,1986. He was raised in Kandy and received his high school education at Dharmaraja College, Kandy. Sudheera entered the University of Kelaniya, Sri Lanka, in 2007 and graduated from the University of Kelaniya with a Bachelor's degree in Chemistry in 2011.

In August 2013, Sudheera moved to Maine, USA, and started his Ph.D. degree at the University of Maine. He worked as a chemistry graduate teaching assistant and research assistant in Prof. Aria Amirbahman's research group. Sudheera is a candidate for the Doctor of Philosophy degree in Chemistry from the University of Maine in August 2021.